nature portfolio

https://doi.org/10.1038/s41586-026-11000-w

## Supplementary information

# Heterogeneous photonic integration of single-crystalline nanomembranes

In the format provided by the authors and unedited

# Heterogeneous photonic integration of single-crystalline nanomembranes – Supplementary Information

Yuan Meng[1†], Wenbo Mao[2†], Zhihao Xu[3†], Di Jia[2†], Mengxin Lin[4,5], Jisung Seo[6,7], Bora Kim[7,8], Xinyuan Zhang[9], Eugene Park[9], Seokje Lee[10,11], Jekyung Kim[10,11], Sangmoon Han[1,19], Ji-Yun Moon[12], Weijie Xu[2], Qian Zhang[2], Xiaoqing He[3], Mingfeng Chen[13], Sang Hyun Nam[14], Jianqi Hu[4,5], Justin S. Kim[3], Sejin Lee[3], Sanggeun Bae[3], Soo Ho Choi[7,8], Tae Hyung Kim[1,14], Yunseok Choi[1], Seung-Il Kim[1], Kyubeen Kim[1], Minho Jin[1], Chen Jiang[1], Yiheng Zhang[2], Young-Hoon Kim[14], Jae-Hyun Lee[15], Hobeom Kim[16], Sheng Ran[13], Xi Wang[13], Cheng-Wei Qiu[17], Frances M. Ross[9], Jeehwan Kim[9,10,11], Minjoo Larry Lee[6,7,8], Hyunseok Kim[6,7,8,18], Tobias J. Kippenberg[4,5], Lan Yang[2,3]*, and Sang-Hoon Bae[1,3,13]*

[1]Department of Mechanical Engineering and Materials Science, Washington University in St. Louis, St. Louis, MO, USA.
[2]Department of Electrical and Systems Engineering, Washington University in St Louis, St. Louis, MO USA.
[3]Institute of Materials Science and Engineering, Washington University in St Louis, St. Louis, MO, USA.
[4]Institute of Physics, Swiss Federal Institute of Technology Lausanne (EPFL), Lausanne, Switzerland.
[5]Institute of Electrical and Micro Engineering (IEM), Swiss Federal Institute of Technology (EPFL), Lausanne, Switzerland.
[6]Department of Materials Science and Engineering, University of Illinois Urbana-Champaign, Urbana, IL, USA.
[7]Holonyak Micro and Nanotechnology Laboratory, University of Illinois Urbana-Champaign, Urbana, IL, USA.
[8]Department of Electrical and Computer Engineering, University of Illinois Urbana-Champaign, Urbana, IL, USA.
[9]Department of Materials Science and Engineering, Massachusetts Institute of Technology, Cambridge, MA, USA.
[10]Department of Mechanical Engineering, Massachusetts Institute of Technology, Cambridge, MA, USA.
[11]Research Laboratory of Electronics, Massachusetts Institute of Technology, Cambridge, MA, USA.
[12]Division of Electronics and Electrical Engineering, Dongguk University, Seoul, Republic of Korea
[13]Department of Physics, Washington University in St Louis, St Louis, MO, USA.
[14]Department of Energy Engineering, Hanyang University, Seoul, Republic of Korea.
[15]Department of Electrical and Computer Engineering, Sungkyunkwan University, Suwon, Republic of Korea.
[16]Department of Materials Science & Engineering, Gwangju Institute of Science and Technology, Gwangju, Republic of Korea.
[17]Department of Electrical and Computer Engineering, National University of Singapore, Singapore, Singapore.
[18]Materials Research Laboratory, University of Illinois Urbana-Champaign, Urbana, IL, USA.
[19]Present address: Department of Semiconductor Engineering, Gwangju Institute of Science and Technology, Gwangju 61005, Republic of Korea.
† Equal contribution.
Correspondence: sbae22@wustl.edu; yang@seas.wustl.edu;

This Supplementary Information contains extended discussions in Supplementary Notes S1~S27 (including Supplementary Figures S1~S40, Tables S1~S3, and references), as listed in the Table of Contents below.

## Table of Contents for Supplementary Notes

## S1. Freestanding nanomembranes lift-off and transfer details

Different functional single-crystalline nanomembranes are prepared by either 2D materials-assisted layer transfer (2DLT)[1-5] or epitaxial lift-off (ELO)[6-8] with film growth details discussed in Methods.

For 2DLT (Fig. S1), 2D-covered single-crystalline substrates are prepared as growth templates[3,4,9], typically monolayer graphene or boron nitride (BN) depending on the polarity of substrate materials[10]. Afterwards, remote epitaxy is performed at varying optimized conditions for GaN[11], GaAs[9,12,13], and YIG[2,14] ($Y_3Fe_5O_{12}$), to name a few[1,15]. The semi-transparent 2D layers facilitate remote adatom interaction with the substrate for single-crystalline epilayers[3], and the subsequent release of the nanomembranes precisely along the 2D layer interface. These 2D interlayers can be realized by either transfer[9,16] or direct growth atop the substrate[11], the proper implementation of which is crucial for realizing successful and scalable 2DLT with guidelines discussed elsewhere[3,17].

For BTO ($BaTiO_3$) and CFO ($CoFe_2O_4$) nanomembranes, ELO and wet transfer processes are applied (see Methods). Different polymer handlers, including polypropylene carbonate (PPC), polymethylmethacrylate (PMMA), polydimethylsiloxane (PDMS), and ethylene-vinyl acetate (EVA) with varying Young's modulus, can be applied for optimal layer transfer yield[8]. For BTO (Fig. S2a), the $Sr_3Al_2O_6$ (SAO)[18-20] sacrificial layer can be etched in deionized (DI) water, followed by scooping of the freestanding PPC/BTO nanomembranes floating on wafer surface to the target photonic chip. For CFO (Fig. S2b), the MgO interlayer can be etched in ammonium sulfate ($(NH_4)_2SO_4$) aqueous solution with slow speed, or heated weak acetic acid solution with faster layer lift-off speed[21,22] without damaging single-crystalline CFO epilayer.

For ELO GaAs nanomembranes for integrated photodetectors, the epitaxial structure is shown as Fig. S3a, where the unintentionally doped (UID) $Al_{0.9}Ga_{0.1}As$ layer can be etched in diluted hydrochloric acid (HCl) or buffered oxide etchant (BOE) for subsequent layer transfer via PDMS handler[23,24] (Fig. S3b). For 2DLT GaN nanomembranes[4,11], due to high-stress-level adhesive layers (Ti/Ni) required for epilayer exfoliation[3] (Methods), its layer transfer process is slightly different (Fig. S4) with additional steps. Details are discussed later in Supplementary Note S16.

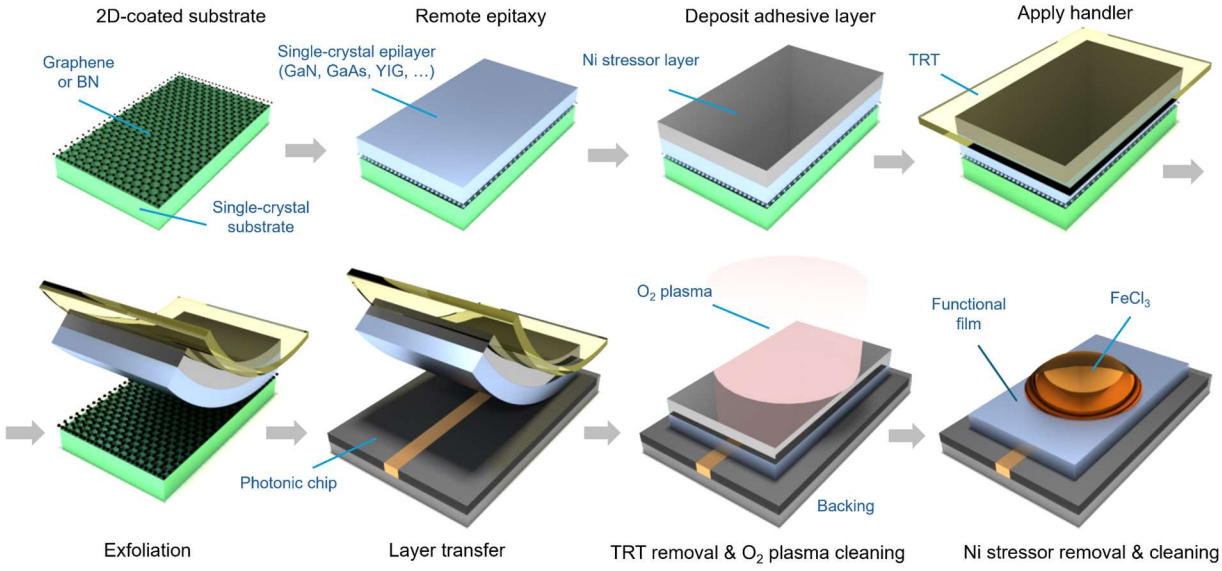


Figure S1. Remote epitaxy through 2D materials and 2DLT process for producing various functional single-crystalline nanomembranes. TRT: thermal release tape.

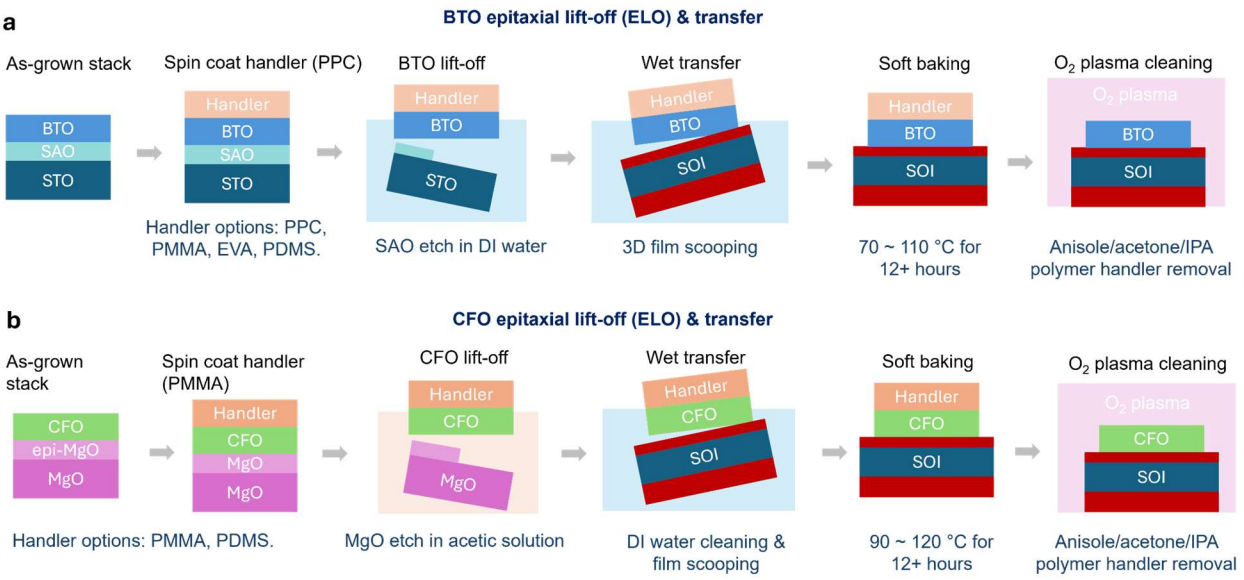


Figure S2. ELO and film transfer processes for BTO (a) and CFO (b) nanomembranes to arbitrary photonic substrates. DI: deionized. IPA: isopropyl alcohol.

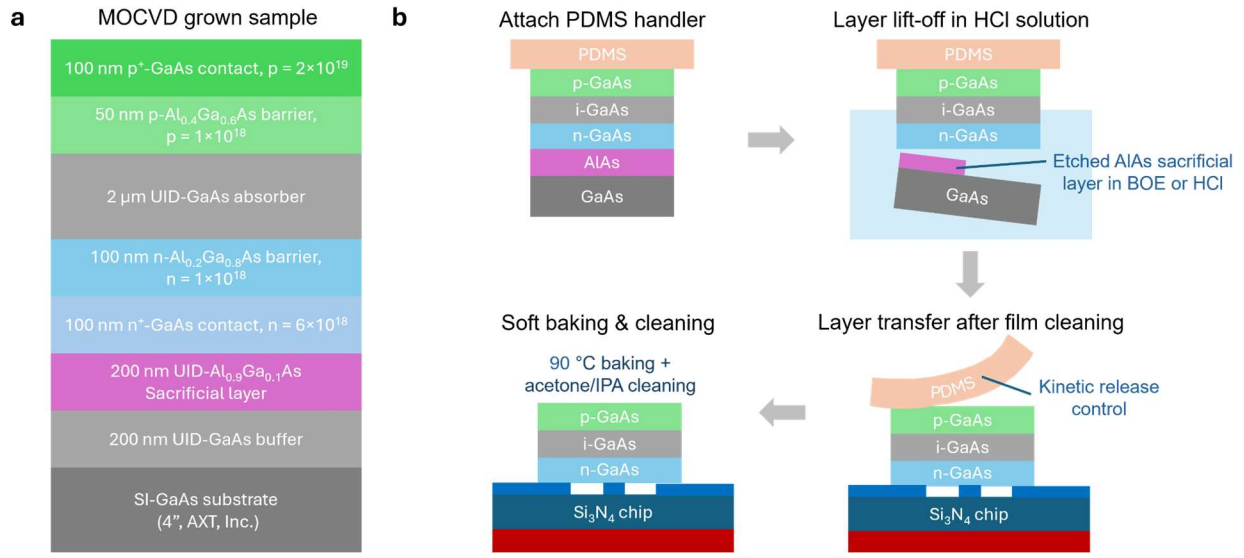


Figure S3. Epitaxial structure (a) and layer transfer process (b) for freestanding GaAs films. SI: semi-insulating. UID: unintentionally doped. BOE: buffered oxide etchant. PDMS: polydimethylsiloxane.

The vdW integration of diverse functional nanomembranes are experimentally verified (Figs. S5, S6) with clean and uniform film surface morphology, atomically sharp interfaces (see Figs. 2i, 3a, 3h, and 4f in main text, and Figs. S10 and S38 discussed later), and high robustness (detailed in Supplementary Note S27). The photonic vdW integration approach[25] has proven with high versatility to infuse arbitrary desired optical functionalities to arbitrary prefabricated photonic templates by selecting proper functional 3D nanomembranes building blocks.

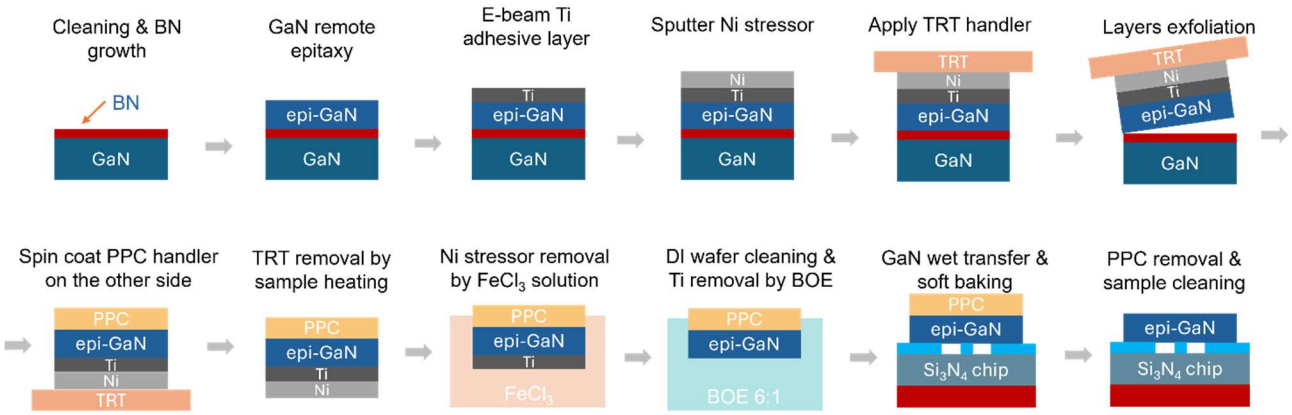


Figure S4. Remote epitaxy and transfer process for freestanding GaN nanomembranes.

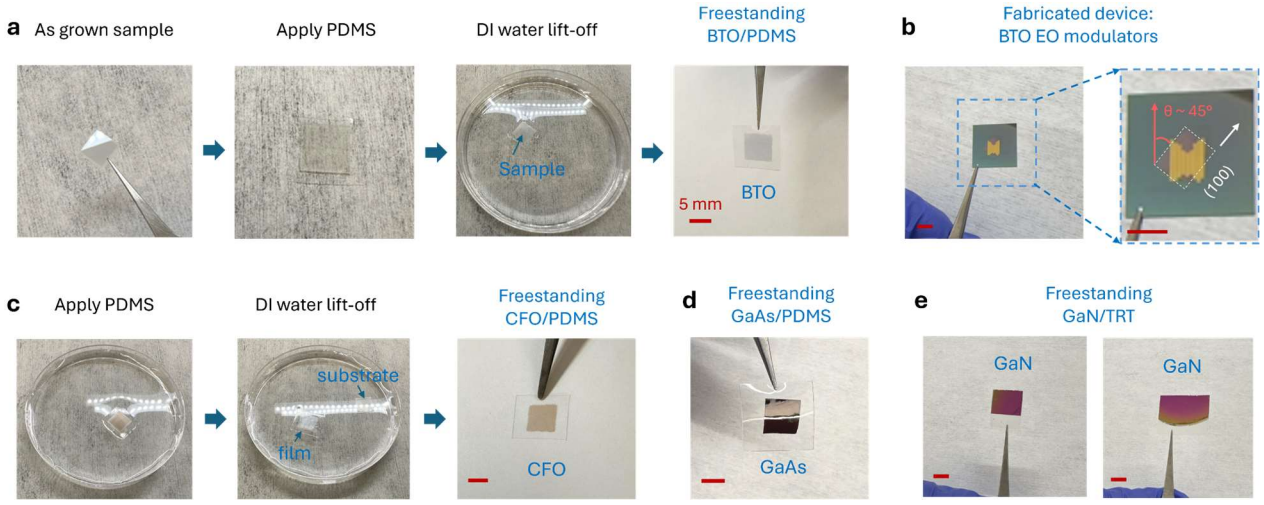


Figure S5. Photographs of BTO film lift-off process (a) and BTO vdW integrated chip (b) with designed 45° film rotation angle $\theta$. (c) Photographs of ELO process for freestanding CFO. (d) and (e) Photographs of freestanding GaAs and GaN nanomembranes. Scale bars: 5 mm.

Photonic chips with prefabricated waveguides, microring resonators, and Mach-Zehnder interferometers (MZIs) patterns etc. are experimentally proven feasible for high-quality nanomembranes vdW integration (Fig. S6), as long as this substrate is overall flat. For example, the etching trenches (due to positive electron beam lithography/EBL resists used) for waveguides and other patterns (Figs. S6a and S6b), and thin electrodes (around 30 nm-thick, shown as Fig. S6c) have been verified for robust 3D film transfer without issues, because the majority of the chip surface is flat to secure uniform film adhesion. However, for photonic chips with significant height distinctions, such as the 500 nm-thick travelling wave electrodes (in Fig. 2f of main text), uniform nanomembrane vdW integration to the substrate will be perturbed. Therefore, thick electrodes are either fabricated atop/after the transferred 3D nanomembranes (e.g. the devices shown in Fig. 2), or applying buried electrode structures (e.g. the device shown in Fig. 4g, detailed later in Supplementary Note S20). This vdW heterogeneous integration strategy well fits the planar processing applied in current complementary metal-oxide-semiconductor (CMOS) foundries for potential scalable manufacturing similar to wafer bonding[7,26,27]. Scanning electron microscopy (SEM) also confirmed the uniform and high-quality nanomembranes bonding to various prefabricated photonic chips without any lossy adhesive interlayers (Fig. S7).

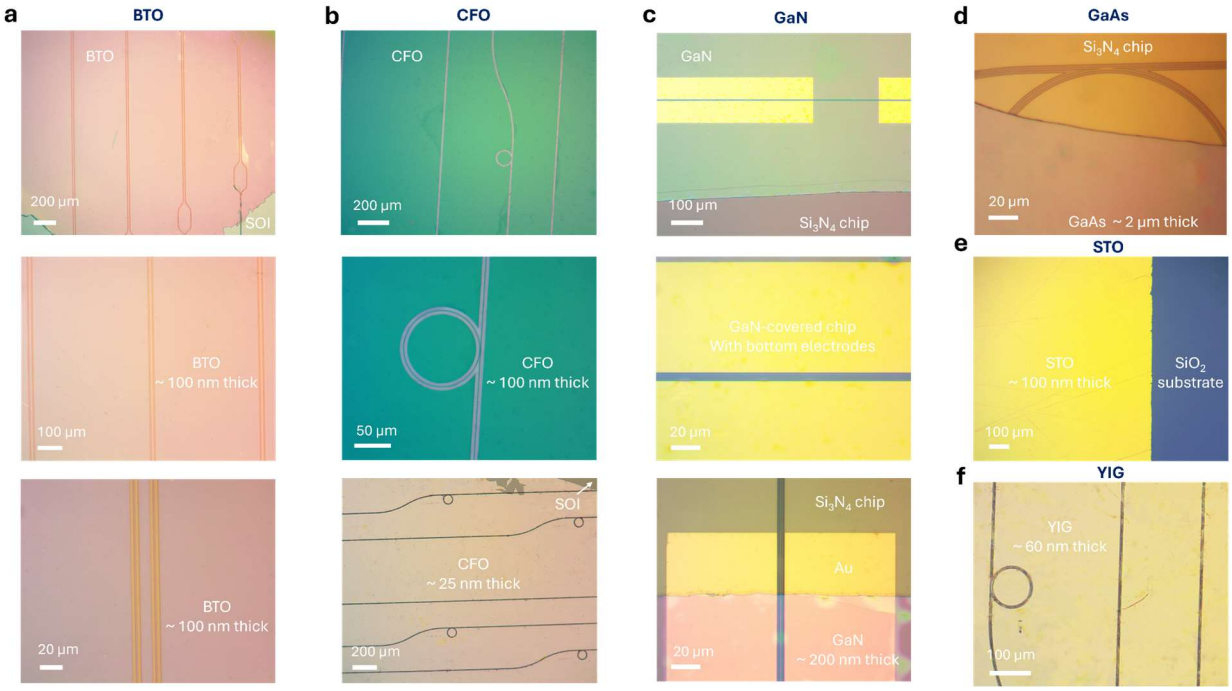


Figure S6. Optical micrographs of vdW integrating various functional nanomembranes to photonic substrates: (a) BTO, (b) CFO, (c) GaN, (d) GaAs, (e) STO, (f) YIG, showing uniform film integration.

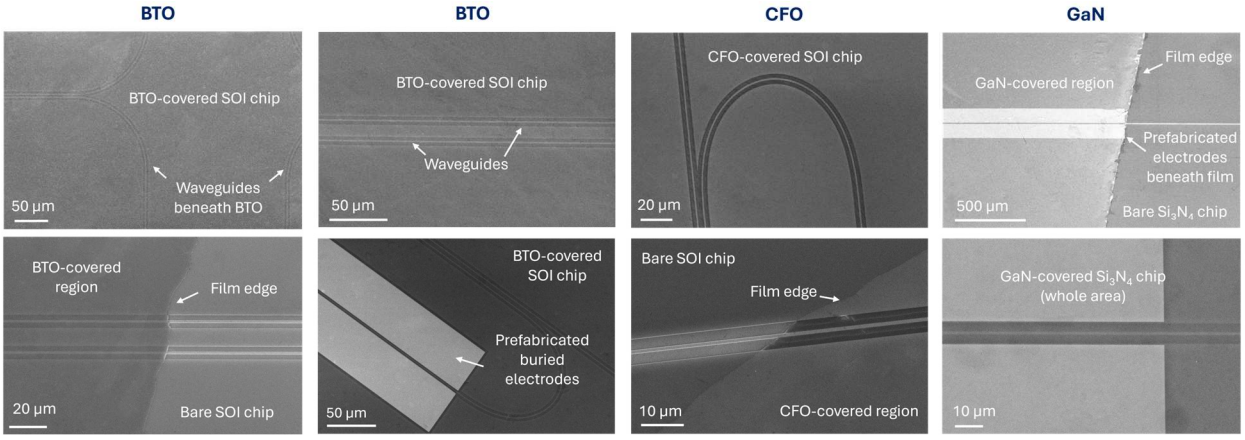


Figure S7. SEM on various vdW hetero-integrated nanomembranes on Si and SiN photonic chips showing uniform and clean surface morphology.

In summary, a library of freestanding single-crystalline 3D nanomembranes with pivotal functionalities for integrated photonics are studied in this work, including EO material BTO (prepared via ELO method), MO material CFO (prepared via ELO) and YIG (prepared via 2DLT and ELO), and group III-V semiconductors GaN (prepared via 2DLT) and GaAs (prepared via 2DLT and ELO). Among them, ELO BTO (with favorable controllability over crystallographic orientation), ELO CFO, 2DLT GaN, and ELO GaAs nanomembranes are selected for heterogeneously integrated photonic device demonstrations.

## S2. Additional material characterization data

Besides the $\varphi$-scan X-ray diffraction (XRD) and electron backscatter diffraction (EBSD) characterizations shown in Fig. 1 (main text), the $2\theta$-$\omega$-scan XRD of the as grown BTO (BTO/SAO/STO), CFO (CFO/MgO/STO), and YIG (YIG/2D/GGG) samples are shown as Figs. S8a-S8c respectively. For CFO, given that the $2\theta$-$\omega$-scan XRD peaks of CFO and MgO are very approaching[22,28], the XRD data for CFO/MgO/STO is shown here (Fig. S8b) instead of the CFO/MgO/MgO (Methods) with very strong MgO peak contributed by the substrate, for a clear and better data visualization. As the MgO interlayer here only has a thin thickness around 20 nm, the XRD peak is majorly contributed by the ~200 nm-thick CFO. Despite that single-crystalline MgO can be also realized by pulsed laser deposition (PLD) on STO substrates[29,30], we have found the direct homoepitaxial MgO buffer layers (atop MgO substrate) yield better CFO quality. By altering growth conditions with lower $O_2$ pressure, the resultant MgO buffer layer showed faster etching speed than the substrate to facilitate ELO of freestanding CFO nanomembranes (see Methods). The $2\theta$-$\omega$-scan XRD data for exfoliated freestanding GaN (2DLT) and GaAs (ELO) nanomembranes resting on TRT support layers are shown as Figs. S8d and S8e respectively.

For electro-optical (EO) material BTO, it has tetragonal crystal unit cells belonging to the $4mm$ point group under room temperature[31,32]. It has a longer crystallographic $c$-axis and two identical shorter axes $a = b < c$. The orientation of the $c$-axis is crucial for the Pockels response and EO applications of BTO[32-37] (discussed in Supplementary Note S7). Besides the $a$-axis-domain BTO (i.e. the crystallographic $c$-axis of BTO is parallel to the film plane) shown in Figs. 1f and 1g (main text) for on-chip EO modulations, by altering the growth condition, $c$-axis-domain BTO (i.e. the crystallographic $c$-axis of BTO is perpendicular to the film plane) can be realized as well. Details are discussed later in Supplementary Note S4. The EBSD map and corresponding Kikuchi pattern of a 60 nm-thick $c$-axis-domain BTO are shown in Figs. S9a and S9b respectively. The EBSD polar maps of different hybrid-domain BTO samples are given as Figs. S9c and S9d.

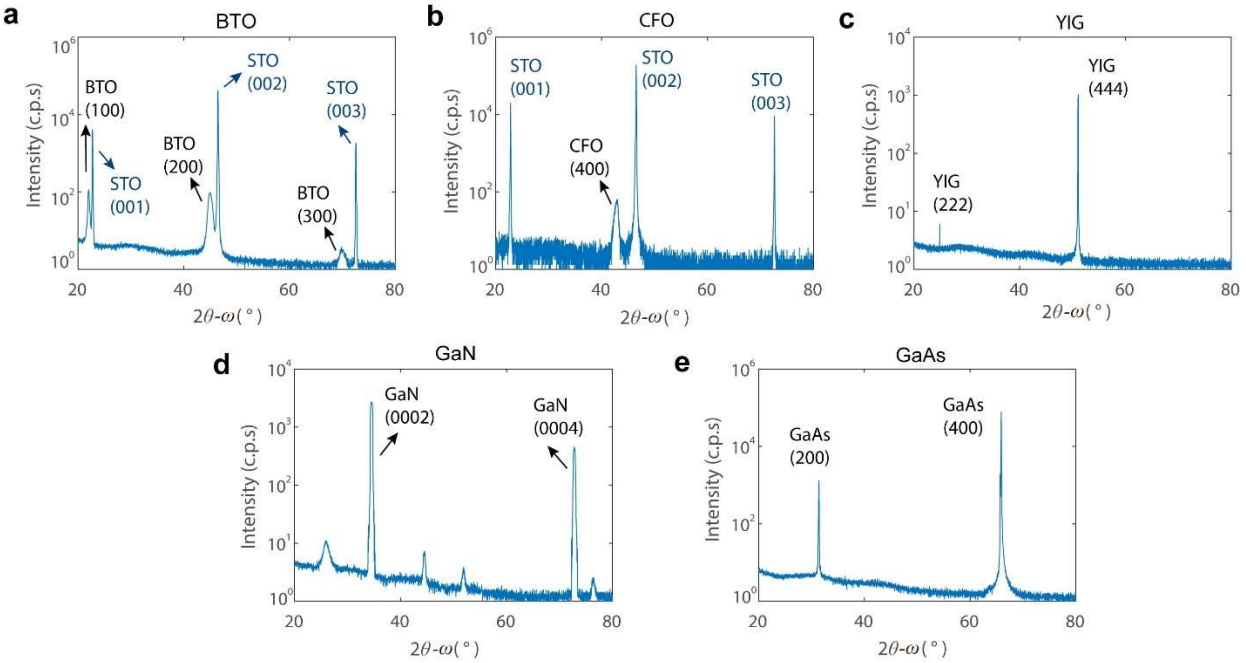


Figure S8. Additional $2\theta$-$\omega$-scan XRD data for grown samples of (a) BTO, (b) CFO, (c) YIG, (d) GaN, and (e) GaAs nanomembranes. For BTO, (200)/(020) peaks are not specifically distinguished in text here.

The experimentally measured permittivity of this (001) BTO nanomembrane is shown as Fig. S9e by constructing a vertical capacitor structure, showing signature butterfly-shaped ferroelectric loop. We note that the exact shape of this hysteresis loop depends on the crystallographic orientation of BTO: for $a$-axis-domain BTO the vertical ferroelectric hysteresis loops are found to be comparatively much smaller or vanishing[38], as in this case the applied voltage is perpendicular to the spontaneous polarizations impacted by BTO's crystallographic $c$-axis orientation.

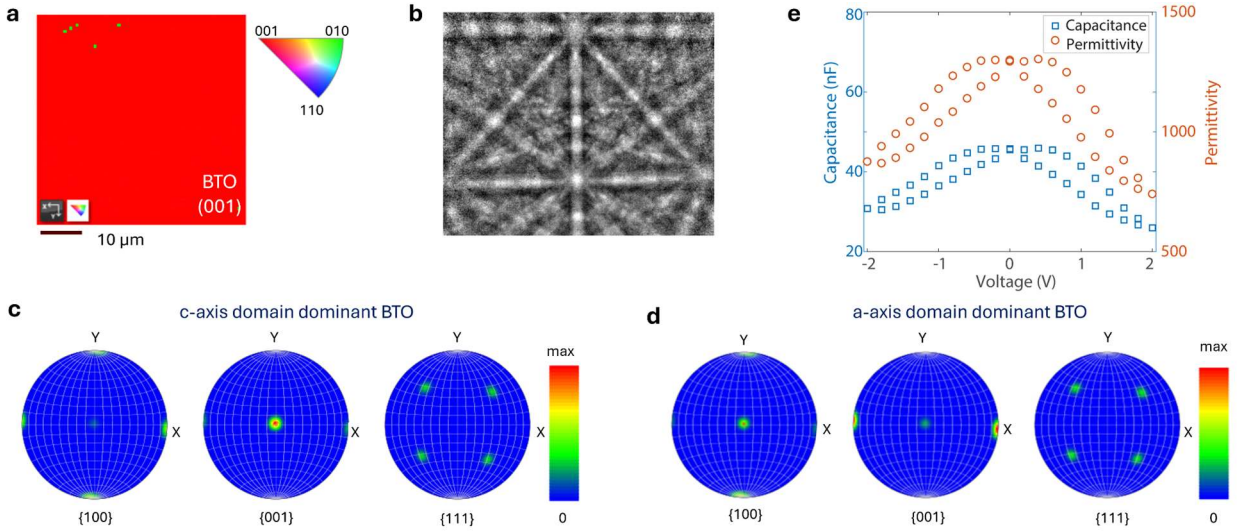


Figure S9. (a) EBSD map of $c$-axis-domain BTO. (b) Corresponding Kikuchi pattern. (c) and (d) EBSD polar maps for hybrid-domain BTO cases: with (c) $c$-axis-domain dominance, or (d) $a$-axis-domain dominance. (e) Experimentally measured capacitance and permittivity data using a vertical capacitor structure for a $c$-axis-domain (001) BTO.

## S3. Artificial 3D heterostructures of GaAs/BTO/GaN/STO

Photonic vdW integration offers a powerful platform for heterogeneous integration[25], enabling the combination of disparate, high-quality optical materials onto arbitrary photonic templates for developing advanced optoelectronic devices. This unique strategy enables the creation of exotic heterogeneous photonic configurations with single-crystalline functional layers of unparalleled performance but with drastically mismatched crystal structures, which are hardly accessible via direct heteroepitaxial approaches.

To embody this concept, Figs. S10a and S10b illustrate the vertical stack and lateral stitch, respectively, of freestanding GaAs, BTO, GaN, and STO films atop $SiO_2$ substrate via photonic vdW integration, further extending the prior concepts of vdW heterostructures[39,40] into 3D thin-films-based materials[25]. Specifically, all these functional nanomembranes are prepared in optimal single-crystallinity, despite with distinct lattice constants (Fig. S10c). In the energy-dispersive X-ray spectroscopy (EDS) of the GaAs/BTO/GaN/STO artificial heterostructure stacked on $SiO_2$ substrate (Fig. S10d), GaAs, BTO, GaN, and STO are colored as yellow, green, red, and blue in the first panel, respectively. We note that this artificial heterostructure stack of GaAs/BTO/GaN/STO is only an example to embody the capability of photonic vdW integration for constructing arbitrary desired high-quality functional optical layers on arbitrary substrate, which can find great value and broad applications in multifunctional hetero-integrated photonics[41-43] and 3D photonics integration[44,45]. A more specific demonstration of such stacked photonic system is beyond the scope of this work. A versatile platform is thus created for advancing nanomembranes technology[18,46-48], studying physical coupling[2,49,50], and prototyping exotic heterogeneous integrated photonic applications[15,25,51-53].

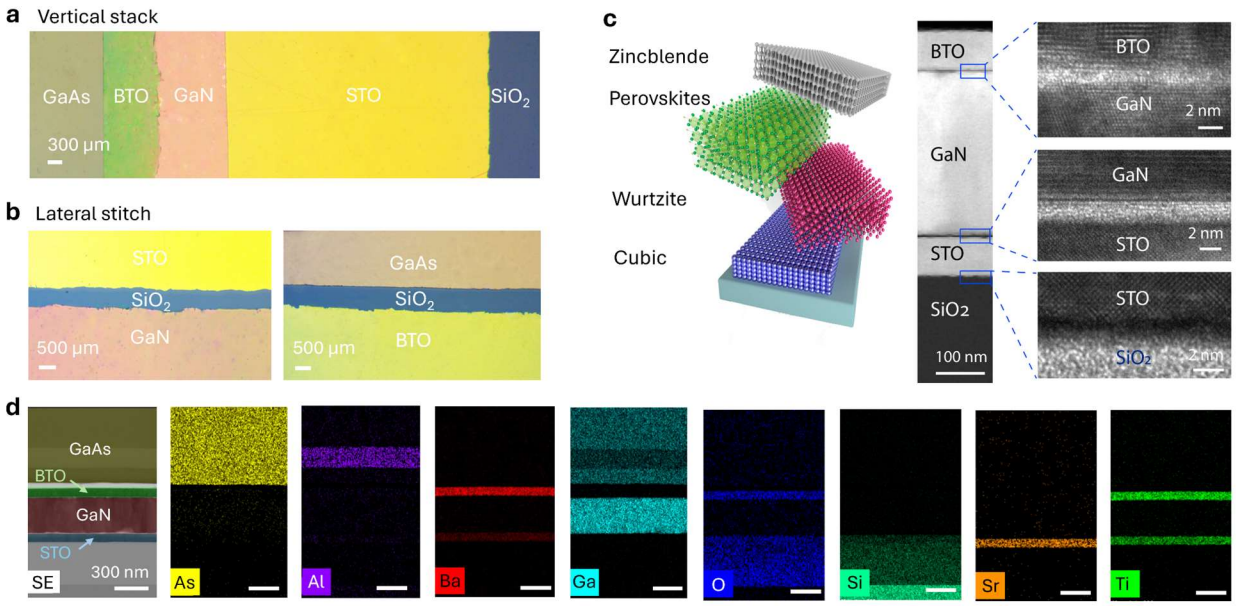


Figure S10. vdW integration of distinct single-crystalline freestanding nanomembranes. (a) and (b) vdW integration modes: Optical microscope photos of vertical stacking (a) and lateral stitching (b) of different 3D nanomembranes. (c) Artificial 3D heterostructures constructed by vdW integrating STO, GaN, BTO to $SiO_2$ substrate, where all the stacked 3D layers are single-crystalline as verified by HR-TEM. (d) STEM-EDS data of a GaAs/BTO/GaN/STO heterostructure atop $SiO_2$ substrate. SE: secondary electron.

## S4. BTO crystallographic axis orientation control

For tetragonal BTO nanomembranes, the orientation of the crystallographic $c$-axis can be controlled by altering growth conditions, which largely impacts BTO's in-plane Pockels response[33,35,54]. Besides the promotion of tensile BTO epitaxial strain relaxation[34,38] (Methods) by PLD process control, the growth temperature, annealing, and cooling rates also play vital role. Figure S11a shows the $2\theta$-$\omega$-scan XRD details of different hybrid-domain BTO nanomembranes transferred to silicon-on-insulator (SOI) substrates during growth condition optimization.

For a brief empirical summary, at lower growth temperatures (around 700~ 800 °C) without film annealing, the grown BTO samples tend to be $c$-axis-domain dominant. This can be tested by the reciprocal space mapping (RSM) measurements (discussed in Supplementary Note S8), or the peak positions in the $2\theta$-$\omega$-scan XRD[35,54]. Given the BTO crystal axes $a = b < c$, for $c$-axis-domain BTO, the longer BTO crystallographic $c$-axis is perpendicular to film plane[31], thus leading to smaller BTO (002) XRD peak angle than $a$-axis-domain (200) or (020) BTO[35], where the longer BTO $c$-axis is parallel to film plane. An example of $c$-axis-domain dominant BTO is shown as Fig. S11a (top panel), while the XRD of $a$-axis-domain dominant BTO is shown in Fig. S11a (bottom panel). In Figs. 1f and 2b (main text), excellent phase pure $a$-axis-domain BTO is observed, with clean (200) or (020) BTO XRD peaks. For the case of hybrid domain BTO (Fig. S11b), a split in the BTO XRD peak takes place (Fig. S11c) around 45°. In contrast to the clean $\varphi$-scan XRD (Fig. 1f), split XRD peaks will be observed for hybrid-domain BTO (Fig. S11d). When growing at elevated temperatures (800~850 °C) with post-growth annealing (detailed in Methods), $a$-axis-domain dominant BTO can be achieved[55]. Nevertheless, in this work post-growth annealing (excluding the slow cooling time) was performed no longer than 4 hours, given that under high $O_2$ pressure and high temperature environments, the SAO interlayer can be degraded[20]. More detailed research can be also performed on the SAO sacrificial layer in future, such as the tetragonal-phased $Sr_4Al_2O_7$ for promoted

BTO epitaxy with tunable lattice constants[19], which has, however, passed beyond the scope of this paper. We have also experimentally found that the XRD and RSM measurements are the more reliable and precise tools to evaluate the $c$-axis orientation of BTO if compared to EBSD, as the Kikuchi patterns (e.g. the one in Fig. S9b) between different BTO domains can be very approaching[31]. For hybrid-domain BTO nanomembranes, the EBSD maps of the representative $c$-axis-domain dominant and $a$-axis-domain dominant BTO samples are shown as Fig. S11f and S11g respectively for reference.

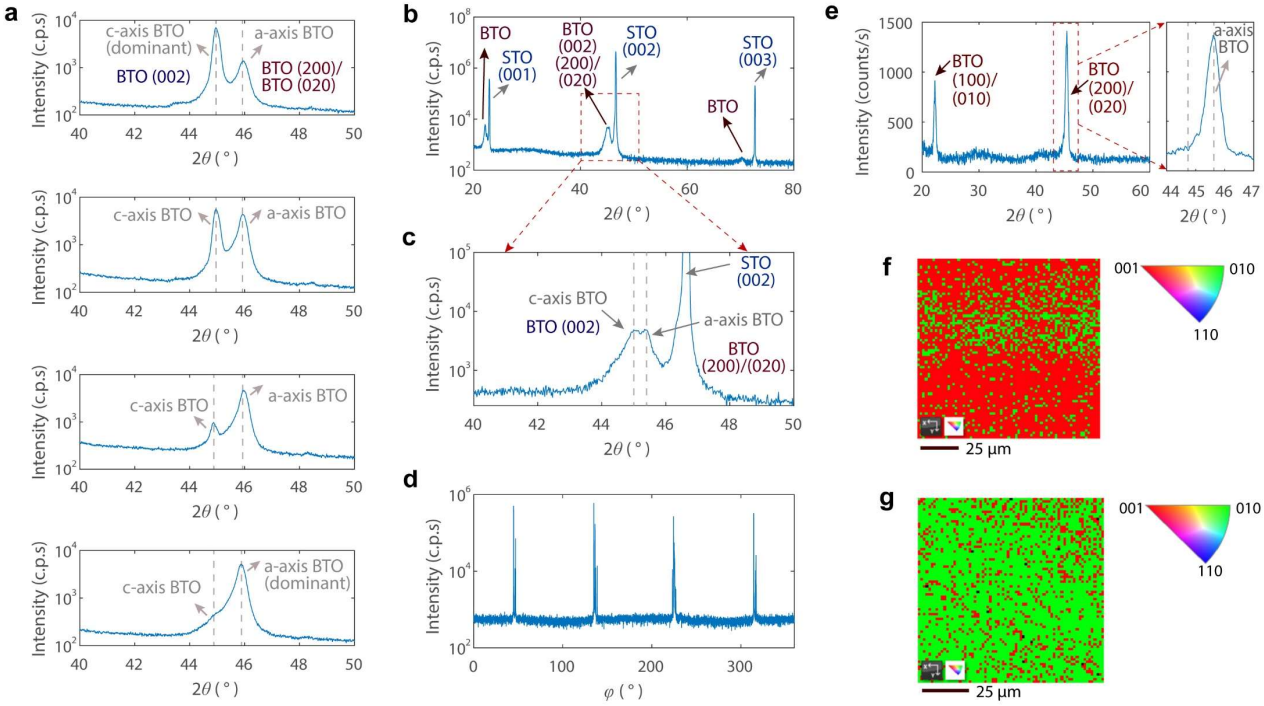


Figure S11. (a) $2\theta$-$\omega$-scan XRD of hybrid-domain BTO nanomembranes transferred to SOI substrates. By altering growth conditions, the resultant BTO samples migrate from $c$-axis-domain dominant to $a$-axis-domain dominant BTO. (b) and (c) $2\theta$-$\omega$-scan XRD (b) and the zoom in (c) of an as-grown BTO/SAO/STO sample with hybrid $c$-axis orientation. (d) Corresponding $\varphi$-scan XRD of the BTO sample shown in (b). (e) $2\theta$-$\omega$-scan XRD of freestanding $a$-axis-domain BTO resting on PDMS, showing narrow BTO (200) or (020) peak. (f) and (g) EBSD maps of BTO samples with hybrid $c$-axis-orientations for $c$-axis-domain dominant (f) and $a$-axis-domain dominant (g) cases.

## S5. Comparisons of ELO and 2DLT

We adopt 2DLT and ELO for the heterogeneous integration of freestanding nanomembranes due to their eminent advantages in fast layer transfer[11], precise film thickness control[6,7], scalable cost reduction[9,25], and high robustness[2] (Fig. S12). For other approaches also permitting the single-crystallinity quality of the hetero-integrated layer, wafer bonding has showcased fruitful results recently[53,56-59]. Nevertheless, sophisticated and lengthy substrate grinding, etching, and polishing procedures are required[35,60]. For mechanical spalling, despite that it can inherit the single-crystallinity from the bulk crystal (given that effective BTO ion slicing is still elusive so far), current demonstrations exhibit highly un-uniform spalled BTO films with vastly compromised film morphology and yield with uncontrollable spalled film thickness[61].

In addition, both 2DLT and ELO enable the recycling of costly substrates[3,11] (see Supplementary Note S27), which contributes significantly to the manufacturing cost of functional materials (such as group III-V semiconductors and complex oxides like STO, BTO, YIG): Only the top thin films are used for devices,

while the expensive bulk substrates primarily only provide mechanical support. The recycled substrates can thus furnish multiple rounds of nanomembranes epitaxy and exfoliation after simple cleaning procedures[7,11,12] towards cost reduction.

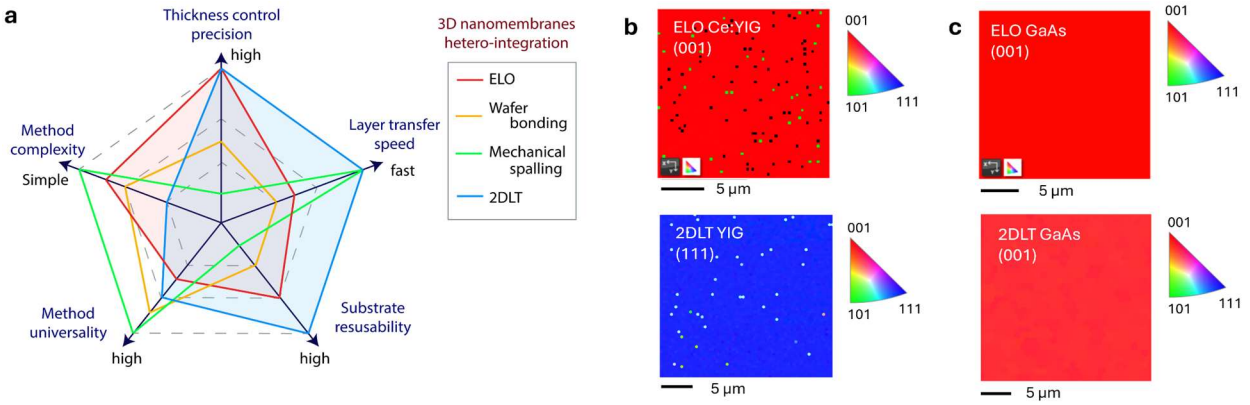


Figure S12. (a) Comparisons of different heterogeneous photonic integration approaches. The ELO and 2DLT methods used in this work are shaded in red and blue colors respectively. (b) and (c) EBSD maps of the different resultant YIG (b) and GaAs (c) nanomembranes under different growth approaches.

For experimental complexity, 2DLT has stringent requirements on 2D-covered substrate to ensure high-quality remote epitaxy and efficient layer release[3,14,17]. For ELO nanomembranes, simpler substrate preparation and epitaxy optimizations are involved. However, the judiciously selection sacrificial layers are mandatory[19,20,62,63], limiting the method universality[10] of ELO compared to 2DLT[3]. For example, despite domain-epitaxy performed[28,64,65], 2DLT YIG showed much better XRD results (Fig. S13, Methods) than domain-epitaxial Ce: YIG (very weak XRD) with cleaner and stronger peaks. Nevertheless, the layer lift-off of 2DLT YIG is found to be more challenging than ELO Ce: YIG, due to the very stringent requirements on 2D interlayer quality and meticulous epitaxy optimizations[2,14]. Failed film exfoliations of 2DLT YIG were also often observed due to etched 2D layers during nonideally controlled remote epitaxy. Figure S12b shows the EBSD maps of ELO Ce: YIG and another 2DLT YIG sample, where the crystal orientation is primarily determined by the crystalline registry of the substrates used (Methods). For group III-V semiconductors (Fig. S12c), both approaches can provide scalable and robust single-crystalline nanomembranes after careful optimizations discussed in our previous works[6,11,13,50]. In brief conclusion, both ELO and 2DLT can offer single-crystalline freestanding nanomembranes after careful optimizations, while 2DLT can become a more competitive option when lacking appropriate sacrificial material to facilitate ELO, but at the cost of increased method complexity.

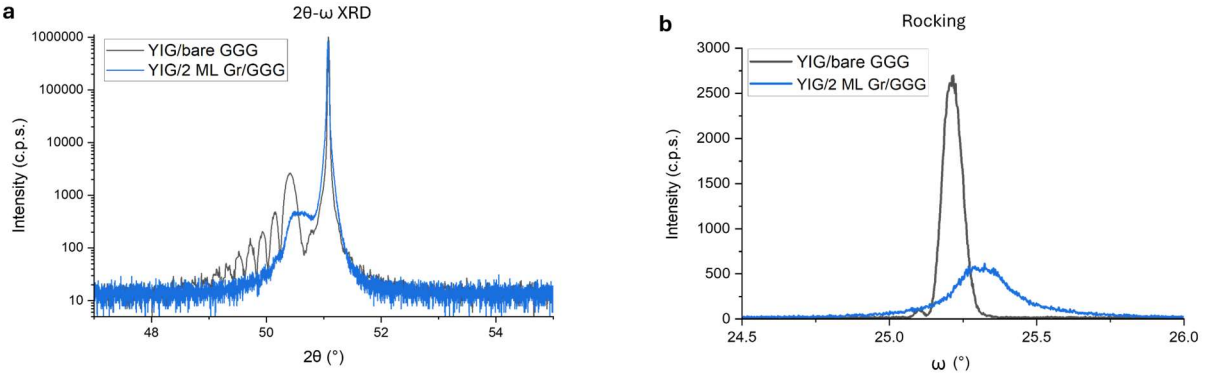


Figure S13. Supplementary $2\theta$-$\omega$-scan (a) and rocking (b) XRD measurements for as-grown 2DLT YIG films atop of two monolayer graphene (2ML Gr)-covered GGG ($Gd_3Ga_5O_{12}$) substrates.

## S6. BTO effective Pockels coefficient estimation details

As discussed in Methods, linear electro-optical (EO) effect (namely Pockels effect) can be formulated by a scalar equation[33] to describe refractive index change of the EO material $\Delta n_{\mathrm{BTO}}$ as

$$\Delta n_{\mathrm{BTO}} = -\frac{1}{2} n_{(0)}^3 r_{\mathrm{eff}} E_{\mathrm{EF}}, \tag{S6-1}$$

where $n_{(0)}$ is the unperturbed refractive index of the EO material[37], $r_{\mathrm{eff}}$ is the effective Pockels coefficient. The applied electric field can be estimated by $E_{\mathrm{EF}} = \frac{V}{g}$, where $V$ is the applied voltage and $g$ is the gap between electrodes.

We have the relation[54,66] between $\Delta n_{\mathrm{BTO}}$ and the mode refractive index change as $\Delta n_{\mathrm{eff}} = \Delta n_{\mathrm{BTO}} \cdot \Gamma$, where $\Gamma = \frac{\int_{\mathrm{EO}} \frac{1}{2}\Re(\mathbf{E}\times\mathbf{H}^*)\cdot\hat{\mathbf{x}}\mathrm{d}S}{\int_{\mathrm{All}} \frac{1}{2}\Re(\mathbf{E}\times\mathbf{H}^*)\cdot\hat{\mathbf{x}}\mathrm{d}S}$ is the overlap between the optical mode and the EO film. Given the modulated phase at one MZI arm is $\Phi = \frac{2\pi L}{\lambda}\Delta n_{\mathrm{eff}}$, where $L$ is the length of the MZI arm, at half-wave voltage $V_\pi$ we have $\Phi_\pi = -\pi = \frac{2\pi L\Gamma}{\lambda}\Delta n_{\mathrm{BTO}} = -\frac{\pi V_\pi L\Gamma}{\lambda g} n_{(0)}^3 r_{\mathrm{eff}}$.

Therefore, we can roughly estimate the effective Pockels coefficient as below.

$$r_{\mathrm{eff}} = \frac{\lambda g}{n_{(0)}^3 \Gamma V_\pi L} \tag{S6-2}$$

Based on Eq. (S6-2), BTO $r_{\mathrm{eff}}$ is estimated based on experimentally measured data $V_\pi L$, numerically simulated Γ via actual device structure parameters, and literature $n_{(0)}$ values.

(1) For a conservative estimation, taking BTO $n_{(0)} = 2.27$ (Ref.[35,66]):

(a) For low-frequency BTO-Si Mach Zehnder modulator (MZM): Si waveguide dimension: 1 μm × 120 nm, BTO thickness: 100 nm, Au electrodes (100 nm) directly deposited on BTO. COMSOL calculated field overlap Γ ≈19.5%. For experimental $V_\pi = 0.65$ V, $L \sim 0.45$ cm (measured at 1 kHz frequency), electrodes gap $g = 4$ μm, at wavelength $\lambda = 1.55$ μm, we have estimated $r_{\mathrm{eff}} \approx 928$ pm/V.

Given that when performing vdW integration of BTO nanomembranes, the rotation angle between BTO (100) axes and the waveguide are set as $\theta \sim 45°$, the effective Pockels coefficient is thus taken as (detailed in Supplementary Note S7) below.

$$r_{\mathrm{eff}} = \frac{\sqrt{2}}{4}(2r_{42} + r_{33} + r_{13}) \tag{S6-3}$$

Assuming Pockels tensor elements as $r_{33} = 100$ pm/V, $r_{13} = 10$ pm/V (same assumption applied henceforth to all estimations in this Note S6), this $r_{\mathrm{eff}}$ corresponds to a Pockels tensor component $r_{42}$ ~1250 pm/V. Currently applied values of $r_{33}$ and $r_{13}$ can be overestimated, while lower $r_{33}$ and $r_{13}$ values taken will lead to further bigger $r_{\mathrm{eff}}$ than current estimation (see Supplementary Note S12).

(b) For high-frequency BTO-Si MZM, Si waveguide dimension: 1.5 μm × 150 nm, BTO thickness: 45 nm, Au electrodes thickness ~500 nm, 250 nm-thick PECVD $SiO_2$ layer between BTO and electrodes (see Fig. S17 for details), COMSOL calculated field overlap Γ ≈ 8.50%.

For experimental $V_\pi = 14.4$ V, $L \sim 0.1$ cm (measured at 2 MHz frequency), electrodes gap $g = 8$ μm, at wavelength $\lambda = 1.55$ μm, we have estimated $r_{\mathrm{eff}} \approx 867$ pm/V, corresponding to $r_{42}$ ~1160 pm/V.

(2) For a less conservative estimation, taking $n_{(0)} = 2.26$ (Ref.[37]):

(a) For low-frequency BTO-Si MZM, calculated Γ ≈ 19.3%. Updating $n_{(0)}$, we have an estimated $r_{\mathrm{eff}} \approx$ 950 pm/V, corresponding to $r_{42}$ ~1290 pm/V.

(b) For high-frequency BTO-Si MZM, calculated $\Gamma \approx 8.47\%$. Updated estimation $r_{\text{eff}} \approx 880$ pm/V, corresponding to $r_{42}$ ~1190 pm/V.

## S7. Multi-domain BTO $r_{\text{eff}}$ Derivation

At crystal principal axes coordinates, we have the impermeability tensor as $\boldsymbol{\eta}(0) = \text{diag}(\eta_1, \eta_2, \eta_3) = \text{diag}(\frac{1}{n_1^2}, \frac{1}{n_2^2}, \frac{1}{n_3^2})$, where $n_1, n_2, n_3$ are the corresponding refractive indices and the semi-axes lengths of the (un-rotated) index ellipsoid[32]. Under external electric field ($\mathbf{E}_{\text{RF}}$), the EO material's impermeability tensor will be impacted and changed into $\boldsymbol{\eta}(\mathbf{E}_{\text{RF}}) = \boldsymbol{\eta}(0) + \Delta\boldsymbol{\eta}(\mathbf{E}_{\text{RF}})$. The perturbed impermeability tensor $\boldsymbol{\eta}(\mathbf{E}_{\text{RF}})$ will still be a 3 × 3 symmetric and positive definite matrix (with matrix elements written as $\eta_{ij}$), corresponding to a rotated and semi-axes-changed ellipsoid.

$$\eta_{11}x^2 + \eta_{22}y^2 + \eta_{33}z^2 + 2\eta_{12}xy + 2\eta_{23}yz + 2\eta_{31}zx = 1 \tag{S7-1}$$

Below the Curie temperature (~120 °C), BTO is in tetragonal phase with the point group of $4mm$ possessing linear EO (Pockels) effect (with crystallographic axes $a = b < c$). Under the Voigt notation we have the EO material's impermeability change written as[33,67]

$$\begin{bmatrix}\Delta\eta_1\\ \Delta\eta_2\\ \Delta\eta_3\\ \Delta\eta_4\\ \Delta\eta_5\\ \Delta\eta_6\end{bmatrix} = \begin{bmatrix}\Delta\eta_{11}\\ \Delta\eta_{22}\\ \Delta\eta_{33}\\ \Delta\eta_{23}\\ \Delta\eta_{31}\\ \Delta\eta_{12}\end{bmatrix} = \begin{bmatrix}\eta_{11}(\mathbf{E}_{\text{RF}}) - \frac{1}{n_1^2}\\ \eta_{22}(\mathbf{E}_{\text{RF}}) - \frac{1}{n_2^2}\\ \eta_{33}(\mathbf{E}_{\text{RF}}) - \frac{1}{n_3^2}\\ \eta_{23}(\mathbf{E}_{\text{RF}})\\ \eta_{31}(\mathbf{E}_{\text{RF}})\\ \eta_{12}(\mathbf{E}_{\text{RF}})\end{bmatrix} = \mathbf{r}_{\text{BTO}} \cdot \mathbf{E}_{\text{RF}} = \begin{bmatrix}0 & 0 & r_{13}\\ 0 & 0 & r_{23}\\ 0 & 0 & r_{33}\\ 0 & r_{42} & 0\\ r_{51} & 0 & 0\\ 0 & 0 & 0\end{bmatrix}\begin{bmatrix}E_x^{\text{RF}}\\ E_y^{\text{RF}}\\ E_z^{\text{RF}}\end{bmatrix} \tag{S7-2}$$

where $\mathbf{r}_{\text{BTO}}$ is the Pockels tensor of BTO (with its elements written as $r_{ij}$), and we have its elements $r_{23} = r_{13}$ and $r_{51} = r_{42}$ due to symmetry constraints. The EO modulation and Pockels effect is thus not only dependent on the applied electric field $\mathbf{E}_{\text{RF}}$, but also on the light polarization direction and the crystal orientation of the BTO material. The optical indicatrix change $\Delta\eta_i = \Delta\left(\frac{1}{n^2}\right)_i = \sum_{j=1}^{3} r_{ij}E_j^{\text{RF}}$, where $\mathbf{E}_{\text{RF}} = \left[E_1^{\text{RF}}, E_2^{\text{RF}}, E_3^{\text{RF}}\right]^T = \left[E_x^{\text{RF}}, E_y^{\text{RF}}, E_z^{\text{RF}}\right]^T$.

The Pockels coefficient matrix $\mathbf{r}_{\text{BTO}}$ above has assumed that the $z$ axis parallel to the crystallographic $c$-axis of BTO. If the c-axis of BTO is rotated, the explicit expression of $\mathbf{r}_{\text{BTO}}$ will be modified. Set $\mathbf{R}$ as a 3 × 3 rotation matrix, and $\mathbf{B}(\mathbf{R})$ as the corresponding (6 × 6) Mandel-Voigt rotation matrix[32,33] that rotates second-rank symmetric tensors in Voigt notation (equivalently rotates the original 3rd-rank Pockels elements $r_{i,j,k}$ with minor symmetry $j \leftrightarrow k$ and then re-contract). The rotated Pockels matrix ${\mathbf{r}_{\text{BTO}}}^{(Q)}$ will be ${\mathbf{r}_{\text{BTO}}}^{(Q)} = \mathbf{B}(\mathbf{R})\mathbf{r}_{\text{BTO}}\mathbf{R}^T$. For example, when BTO c-axis is in plane and parallel to lab axis $x$, we have its Pockels tensor ${\mathbf{r}_{\text{BTO}}}^{(x\|c)}$ (with symmetrical constraints implemented) as below.

$${\mathbf{r}_{\text{BTO}}}^{(x\|c)} = \begin{bmatrix}r_{33} & 0 & 0\\ r_{13} & 0 & 0\\ r_{13} & 0 & 0\\ 0 & 0 & 0\\ 0 & 0 & r_{42}\\ 0 & r_{42} & 0\end{bmatrix} \tag{S7-3}$$

Now consider the following coordinates: under principal axes coordinates $(x', y', z')$, BTO $c$-axis is parallel to $z'$ axis, the other two crystallographic axes $(a = b)$ are parallel to $x'$ and $y'$ axes respectively. Set the lab coordinates as $(x, y, z)$, considering only the $c$-axis in-plane BTO case, assume the angle between BTO $c$-

axis ($\hat{\mathbf{x}}'$) and $x$-axis ($\hat{\mathbf{x}}$) as $\theta = \text{acos}(\hat{\mathbf{x}}' \cdot \hat{\mathbf{x}})$. The dominant light polarization $\mathbf{E}_{\text{opt}}$ (for $TE_{00}$ mode) and applied electric field $\mathbf{E}_{\text{RF}}$ are both parallel to $x$ axis.

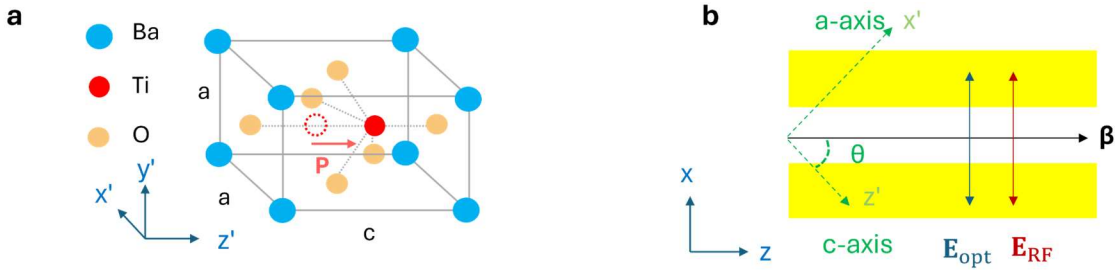


Figure S14. (a) Crystallographic structure of BTO and the principal coordinates. **P**: polarization. (b) Device lab coordinates and the orientations of vectors. $\theta$: rotation angle between BTO $c$-axis ($z'$ axis) and $z$ axis. $\beta$: optical mode propagation constant, showing light propagation and waveguide direction.

**(1) BTO crystal axis un-rotated**

When $\theta = 0$, the crystallographic coordinates overlap with lab coordinates ($a \parallel x$, $b \parallel y$, $c \parallel z$), applying $\mathbf{E}_{\text{RF}} = [E_x^{\text{RF}}, 0, 0]^T$ and light propagation direction $\beta \parallel z$, only the $i = 5$ (i.e. $xz$) row contributes to impermeability change $\Delta\boldsymbol{\eta} = \mathbf{r}_{\text{BTO}} \cdot \mathbf{E}_{\text{RF}}$ in Eq. (S7-1).

$$\Delta\eta_{xz} = \Delta\eta_{zx} = r_{51}E_x^{\text{RF}}, \Delta\eta_{ij} = 0 \text{ otherwise.} \tag{S7-4}$$

Set BTO ordinary and extraordinary light refractive indices as $n_o$ and $n_e$ respectively, we have BTO unperturbed impermeability tensor (in principal axes) $\boldsymbol{\eta}(0) = \text{diag}(\eta_o, \eta_o, \eta_e) = \text{diag}\left(\frac{1}{\varepsilon_o}, \frac{1}{\varepsilon_o}, \frac{1}{\varepsilon_e}\right) = \text{diag}(\frac{1}{n_o^2}, \frac{1}{n_o^2}, \frac{1}{n_e^2})$, the index-ellipsoid (optic indicatrix) from Eq. (S7-1) becomes

$$\eta_o x^2 + \eta_o y^2 + \eta_e z^2 + 2r_{51}zx = 1. \tag{S7-5}$$

We have the explicit Impermeability tensor as $\boldsymbol{\eta}(\mathbf{E}_{\text{RF}}) = \boldsymbol{\eta}(E_x^{\text{RF}})$ as

$$\boldsymbol{\eta}\left(E_x^{\text{RF}}\right) = \begin{bmatrix} \eta_o & 0 & r_{51}E_x^{\text{RF}} \\ 0 & \eta_o & 0 \\ r_{51}E_x^{\text{RF}} & 0 & \eta_e \end{bmatrix}. \tag{S7-6}$$

The relative permittivity tensor $\boldsymbol{\epsilon} = \boldsymbol{\eta}^{-1}$ can be also explicitly calculated as below.

$$\boldsymbol{\epsilon}\left(E_x^{\text{RF}}\right) = \begin{bmatrix} \frac{\varepsilon_o}{1-\varepsilon_o\varepsilon_e\Delta^2} & 0 & -\frac{\varepsilon_o\varepsilon_e\Delta}{1-\varepsilon_o\varepsilon_e\Delta^2} \\ 0 & \varepsilon_o & 0 \\ -\frac{\varepsilon_o\varepsilon_e\Delta}{1-\varepsilon_o\varepsilon_e\Delta^2} & 0 & \frac{\varepsilon_e}{1-\varepsilon_o\varepsilon_e\Delta^2} \end{bmatrix}, \text{ with } \Delta \equiv r_{51}E_x^{\text{RF}} \tag{S7-7}$$

When $\Delta$ is very small, the permittivity tensor can be simplified as first-order small signal form (for BTO $r_{51} = r_{42}$):

$$\boldsymbol{\epsilon}\left(E_x^{\text{RF}}\right) \sim \begin{bmatrix} \varepsilon_o & 0 & -\varepsilon_o\varepsilon_e r_{51}E_x^{\text{RF}} \\ 0 & \varepsilon_o & 0 \\ -\varepsilon_o\varepsilon_e r_{51}E_x^{\text{RF}} & 0 & \varepsilon_e \end{bmatrix} \tag{S7-8}$$

**(2) BTO crystal axis rotated**

When $\theta \neq 0$, set the rotation matrix $\mathbf{R}(\theta)$ (from crystal coordinates to lab coordinates) about $y$ axis by $\theta$:

$$\mathbf{R}(\theta) = \begin{bmatrix} \cos\theta & 0 & \sin\theta \\ 0 & 1 & 0 \\ -\sin\theta & 0 & \cos\theta \end{bmatrix} \tag{S7-9}$$

We have $[x, y, z]^T = \mathbf{R}(\theta)^T[x', y', z']^T$ , and applied electric field in crystal axes $\mathbf{E}_{\mathrm{RF}}{}^{(\mathrm{c})} = \mathbf{R}(\theta)^T[E_x^{\mathrm{RF}}, 0, 0]^T = [E_x^{\mathrm{RF}}\cos\theta, 0, E_x^{\mathrm{RF}}\sin\theta]^T$. The change of impermeability in crystal axes $\Delta\boldsymbol{\eta}^{(\mathrm{c})}\left(E_x^{\mathrm{RF}}\right)$ can thus be given by:

$$\Delta\boldsymbol{\eta}^{(\mathrm{c})}\left(E_x^{\mathrm{RF}}\right) = \begin{bmatrix} r_{13}E_x^{\mathrm{RF}}\sin\theta & 0 & r_{51}E_x^{\mathrm{RF}}\cos\theta \\ 0 & r_{13}E_x^{\mathrm{RF}}\sin\theta & 0 \\ r_{51}E_x^{\mathrm{RF}}\cos\theta & 0 & r_{33}E_x^{\mathrm{RF}}\sin\theta \end{bmatrix} \tag{S7-10}$$

By applying $\boldsymbol{\eta}^{(\mathrm{c})}\left(E_x^{\mathrm{RF}}\right) = \boldsymbol{\eta}(0) + \Delta\boldsymbol{\eta}^{(\mathrm{c})}\left(E_x^{\mathrm{RF}}\right)$ and the rotation of crystal axes to lab axes $\boldsymbol{\eta}^{(\mathrm{lab})}\left(E_x^{\mathrm{RF}}\right) = \mathbf{R}(\theta)\boldsymbol{\eta}^{(\mathrm{c})}\left(E_x^{\mathrm{RF}}\right)\mathbf{R}(\theta)^T$, we have the BTO's impermeability tensor under lab axis $(x, y, z)$ as $\boldsymbol{\eta}(\theta, E_x^{\mathrm{RF}})$:

$$\boldsymbol{\eta}\left(\theta, E_x^{\mathrm{RF}}\right) = \begin{bmatrix} A & 0 & C \\ 0 & B & 0 \\ C & 0 & D \end{bmatrix} \tag{S7-11}$$

with entries:

$$A = \underbrace{(\eta_o\cos^2\theta + \eta_e\sin^2\theta)}_{\text{Zero-field}} + \underbrace{E_x^{\mathrm{RF}}\sin\theta[(2r_{51} + r_{13})\cos^2\theta + r_{33}\sin^2\theta]}_{\text{EO modulation}}$$

$$B = \underbrace{\eta_o}_{\text{Zero-field}} + \underbrace{E_x^{\mathrm{RF}}r_{13}\sin\theta}_{\text{EO modulation}}$$

$$C = \underbrace{(\eta_e - \eta_o)\sin\theta\cos\theta}_{\text{Zero-field}} + \underbrace{E_x^{\mathrm{RF}}\cos\theta[r_{51}(\cos^2\theta - \sin^2\theta) + (r_{33} - r_{13})\sin^2\theta]}_{\text{EO modulation}}$$

$$D = \underbrace{(\eta_e\cos^2\theta + \eta_o\sin^2\theta)}_{\text{Zero-field}} + \underbrace{E_x^{\mathrm{RF}}\sin\theta[(r_{33} - 2r_{51})\cos^2\theta + r_{13}\sin^2\theta]}_{\text{EO modulation}}.$$

The relative permittivity tensor $\boldsymbol{\epsilon}$ can thus be solved in an analytic expression (with $\Psi \equiv AD - C^2$) as below.

$$\boldsymbol{\epsilon}\left(\theta, E_x^{\mathrm{RF}}\right) = \boldsymbol{\eta}^{-1}\left(\theta, E_x^{\mathrm{RF}}\right) = \begin{bmatrix} \frac{D}{\Psi} & 0 & -\frac{C}{\Psi} \\ 0 & \frac{1}{B} & 0 \\ -\frac{C}{\Psi} & 0 & \frac{A}{\Psi} \end{bmatrix} \tag{S7-12}$$

The anisotropic refractive index tensor can thus be derived as $\mathbf{n} = \boldsymbol{\epsilon}^{1/2}$, assuming relative permeability $\mu_r = 1$ for non-magnetic material BTO.

Given that the crystallographic coordinates are rotated by $y$ axis, we have the refractive index component $n_{yy} = 1/\sqrt{B}$. Using the identity $\sqrt{\mathbf{M}} = \frac{\mathbf{M} + \sqrt{\det(\mathbf{M})}\cdot\mathbf{I}}{\sqrt{\mathrm{tr}(\mathbf{M}) + 2\mathrm{sqrt}[\det(\mathbf{M})]}}$ (where $\mathbf{I}$ is the identity matrix) for any given 2 × 2 symmetric positive definite (SPD) matrix $\mathbf{M}$ (where $\boldsymbol{\eta}$ and $\boldsymbol{\epsilon}$ are also SPD matrices due to physical constraints), the $x - z$ block of the refractive index tensor $\mathbf{n}_{xz}$ (2 × 2) can thus be calculated $\mathbf{n}_{xz} = \sqrt{\boldsymbol{\epsilon}_{xz}}$, yielding the full anisotropic refractive index tensor $\mathbf{n}(\theta, E_x^{\mathrm{RF}})$ at lab coordinates $(x, y, z)$:

$$\mathbf{n}\left(\theta, E_x^{\mathrm{RF}}\right) = \begin{bmatrix} \frac{D/\sqrt{\Psi}+1}{\sqrt{A+D+2\sqrt{\Psi}}} & 0 & -\frac{C/\sqrt{\Psi}}{\sqrt{A+D+2\sqrt{\Psi}}} \\ 0 & \frac{1}{\sqrt{B}} & 0 \\ -\frac{C/\sqrt{\Psi}}{\sqrt{A+D+2\sqrt{\Psi}}} & 0 & \frac{A/\sqrt{\Psi}+1}{\sqrt{A+D+2\sqrt{\Psi}}} \end{bmatrix} \tag{S7-13}$$

The above Eqs. (S7-11) ~ (S7-13) can be implemented into commercial numerical simulation tools such as Lumerical FDTD Solutions or COMSOL Multiphysics for full Pockels electromagnetic simulations (input

Pockels components $r_{13}, r_{33}, r_{42} = r_{51}$) for light propagating in single-domain BTO under external electric field (discussed later in Supplementary Note S11).

**(3) Multi-domain BTO**

Set $\theta$ as the angle between waveguide direction and BTO $c$-axis, applying the coordinates transform from crystal axes to lab axes $[x, y, z]^T = \mathbf{R}(\theta)^T[x', y', z']^T$, the refractive index change at $\hat{\mathbf{x}}$ direction can be written from Eqs. (S7-1) and (S7-2) as

$$Ax^2 + \cdots = \{(\eta_o \cos^2\theta + \eta_e \sin^2\theta) + E_x^{\mathrm{RF}}[(2r_{42} + r_{13})\sin\theta\cos^2\theta + r_{33}\sin^3\theta]\}\, x^2 + \cdots = 1, \quad \text{(S7-14)}$$

where symmetry relation $r_{51} = r_{42}$ has been applied. Given that in this case both light polarization $\mathbf{E}_{\mathrm{opt}}$ and applied electric field $\mathbf{E}_{\mathrm{RF}} = [E_x^{\mathrm{RF}}, 0, 0]^T$ are parallel to $x$ axis, the other terms in Eq. (S7-1) except $\eta_{11}x^2$ can be omitted. We thus have the impermeability change as $\Delta\eta_{11} = E_x^{\mathrm{RF}}\sin\theta[(2r_{42} + r_{13})\cos^2\theta + r_{33}\sin^2\theta]$ in lab coordinates. By combining it with the Pockels equation, we have the effective Pockels coefficient for single-domain BTO as

$$r_{\mathrm{eff}}(\theta) = [(2r_{42} + r_{13})\sin\theta\cos^2\theta + r_{33}\sin^3\theta]. \quad \text{(S7-15)}$$

For $c$-axis in-plane BTO (i.e. $a$-axis-domain BTO), 4 potential domain orientations exist. Set $\varphi$ as the BTO domain orientation (for not poling a-domain/ c-axis parallel to film BTO grown in our case, possible $\varphi$ values are 0°, 90°, 180°, 270°) respective to the film edge (100), and $\gamma_\varphi$ as the portion of the $\varphi$ orientated domains (satisfying $\sum_\varphi \gamma_\varphi = 1$), the effective Pockels coefficient of the BTO film is the weighted average of all the possible domains[37].

$$r_{\mathrm{eff}}(\theta, \varphi) = \sum_\varphi \gamma_\varphi[\sin(\theta + \varphi)\cos^2(\theta + \varphi)(2r_{42} + r_{13}) + \sin^3(\theta + \varphi)r_{33}] \quad \text{(S7-16)}$$

After poling (i.e. either $\varphi \in \{0°, 90°\}$ or $\varphi \in \{180°, 270°\}$) assuming the portion of perpendicularly orientated domains are same, we have $r_{\mathrm{eff}}(\theta) = \frac{1}{2}[\cos^2\theta \sin\theta\,(2r_{42} + r_{13}) + \sin^3\theta r_{33}] + \frac{1}{2}\left[\cos^2\left(\theta + \frac{\pi}{2}\right)\sin\left(\theta + \frac{\pi}{2}\right)(2r_{42} + r_{13}) + \sin^3\left(\theta + \frac{\pi}{2}\right)r_{33}\right]$. Thus, we have

$$\begin{aligned} r_{\mathrm{eff}}(\theta) &= \frac{1}{2}(2r_{42} + r_{13})(\cos^2\theta \sin\theta + \sin^2\theta \cos\theta) + \frac{1}{2}r_{33}(\cos^3\theta + \sin^3\theta) \\ &= \frac{\sqrt{2}}{2}\cos\left(\theta - \frac{\pi}{4}\right)\left[\left(\frac{3}{2}r_{33} - r_{42} - \frac{1}{2}r_{13}\right) + (2r_{42} + r_{13} - r_{33})\cos^2(\theta - \frac{\pi}{4})\right], \end{aligned} \quad \text{(S7-17)}$$

with trigonometric identities transform applied. Therefore, given that $\cos\left(\theta - \frac{\pi}{4}\right) \in [-1,1]$, thus at $\theta = \frac{\pi}{4}$, the effective Pockels coefficient reaches its maxim as below[37,54].

$$r_{\mathrm{eff}} = \frac{\sqrt{2}}{4}(2r_{42} + r_{33} + r_{13}). \quad \text{(S7-18)}$$

## S8. RSM measurement details

Reciprocal space mapping (RSM) XRD is a powerful tool to quantify the crystallographic orientations of hybrid-domain BTO[35,55,68,69]. Detailed RSM analyses are performed for as grown BTO/SAO/STO samples (Fig. S15a), the positions of lattice planes are calibrated based on the (103) lattice plane of the STO substrate (Methods). To evaluate the crystal orientation of the freestanding BTO nanomembranes, a thick $a$-axis-domain BTO was transferred to fused glass substrate (Fig. S15b), where scaling calibrations were made similarly to Fig. S15a. The original data shown in Fig. S15b was then modified in color bar, yielding a clearer color visualization of the crystal planes shown in Fig. 2c (main text). For a lattice plane $(h, k, l)$, the reciprocal space lattice units can be calculated as below.

$$(q_x, q_z) = \left(\sqrt{\frac{k^2}{a^2} + \frac{l^2}{c^2}}, \frac{h}{a}\right) \quad \text{(S8-1)}$$

Given the lattice parameters for tetragonal BTO as $a = b = 3.994$ Å and $c = 4.038$ Å, the theoretical positions for single $a$-axis-domain BTO crystal planes (301) and (310) are thus estimated as (2.47, 7.51) and (2.50, 7.51) respectively (in the unit of nm$^{-1}$). The two approaching intensities of (301) and (310) planes indicate two equivalent domain orientations for $a$-axis BTO domains (with identical proportions)[34], where the BTO $c$-axes are parallel to film plane but can have two orientations perpendicular to each other[35,37,54] (as shown in Fig. S15a inset panel). The theoretical $(q_x, q_z)$ position for single $c$-axis-domain BTO (103) crystal plane (interchanging the formula of $q_x$ and $q_z$in Eq. S8-1) is estimated as (2.50, 7.43). From Fig. S15b, a significant (over 2 orders of magnitude) intensity contrast can be observed between (301) or (310) planes and (103) planes, verifying our resultant BTO nanomembranes are pure single-crystalline and $a$-axis-domain dominant, which is crucial to realize giant in-plane Pockels response and on-chip EO applications[35].

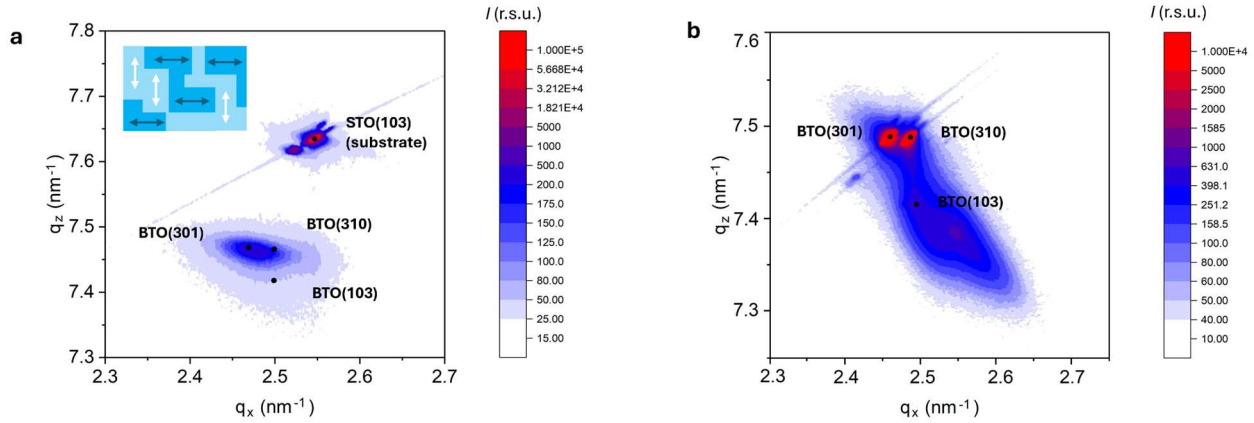


Figure S15. RSM XRD for (a) as grown BTO/SAO/STO sample with an around 80 nm-thick $a$-axis-domain BTO, and (b) RSM for an over 300 nm-thick $a$-axis-domain BTO transferred to amorphous glass substrate. Inset panel: top view schematics of $a$-axis-domain BTO with two possible $c$-axis orientations in multiple ferroelectric domains, where the arrows indicate the direction of spontaneous ferroelectric polarization (parallel to $c$-axis orientation).

## S9. Si and SiN photonics fabrication details

The Si and $Si_3N_4$ (SiN) photonic chips are fabricated at university cleanrooms based on commercial SOI or stoichiometric $Si_3N_4$-on-insulator (SiNOI) wafers via electron-beam lithography (EBL) and inductively coupled plasma reactive ion etching (ICP-RIE) processes (Methods, Figs. S16a and S16b). Optical measurements (Fig. S16c) and SEM characterizations (Fig. S16d) confirmed the good quality of these lab-fabricated chips, through foundry-based professional photonic chips are expected to further enhance the performance of devices discussed in this work (see Supplementary Note S15). Despite photolithography is more favorable to realize electrodes patterning, aligned EBL was adopted instead primarily due to the practical cleanroom facilities constraints here. To facilitate ideal vdW integration and layer bonding of the freestanding functional nanomembranes, buried electrode structures are applied for certain devices (such as the device in Fig. 4g in main text) to eliminate big height variations of the chip surface. In this case, the area for placing electrodes needs to be patterned and etched together with the waveguides (Figs. S16b, S16e). Therefore, after metal deposition and lift-off, thick electrodes can have the same height as the photonic waveguides to enable good vdW heterogeneous integration. Very thin electrodes are proven feasible for good vdW integration, such as the ones (~30 nm thick Ti/Au) used in SiN photonic chips (Fig.

S16f) for III-V nanomembranes vdW integration, with uniform layer bonding (Figs. S6, S7) and high robustness after proper thermal treatments (Supplementary Note S27).

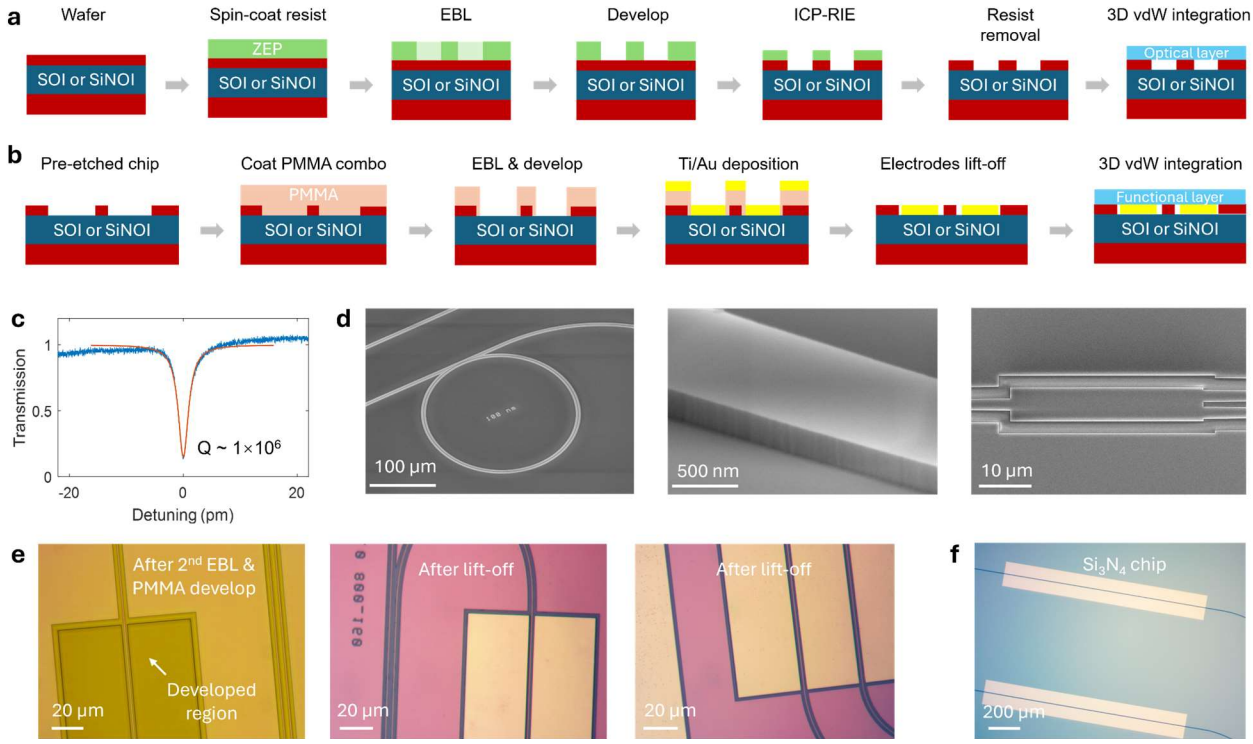


Figure S16. (a) Device fabrication flow for SOI or SiNOI photonic chips. (b) Additional nanofabrication steps when photonic chips with buried electrodes are needed. (c) Normalized optical transmission curve for a SOI microring resonator. (d) SEM images of fabricated SOI and SiNOI photonic structures. (e) Optical micrographs of a SOI chip after aligned EBL and development of thick double-layered PMMA for buried electrodes (left panel), and the fabricated devices after metal lift-off (right panels). (f) Optical micrograph of fabricated SiNOI chips before performing vdW integration.

## S10. High-speed BTO MZMs design

The BTO Mach-Zehnder modulator (MZM) device structures for Figs. 2k and 2h (main text) are illustrated as Figs. S17a and S17b respectively. To enable high-speed EO applications, travelling wave electrodes design are required[57,70-72] to simultaneously catch the following goals: (1) matched group velocities[73] between the high-speed microwave (RF) electrical signal $n_g^{\mathrm{RF}}$ and optical signal $n_g^{\mathrm{Opt}}$, (2) about $Z_0 = 50$ Ω device characteristic impedance, and (3) low RF signal propagation loss along the electrodes. Nevertheless, the big relative permittivity of BTO at low frequencies makes it challenging to perfectly match $n_g^{\mathrm{RF}}$ and $n_g^{\mathrm{Opt}}$. Therefore, a trade-off emerged when designing BTO-based MZMs.

To best exploit the large in-plane Pockels response of $a$-axis-domain BTO, thicker BTO nanomembranes can be selected for higher overlap between the light field and EO material. Directly depositing electrodes atop BTO layer with narrow gap distance $g$ between the signal (S) and ground (G) electrodes also enable strongest electric field intensity within the BTO material under given bias voltage. However, in this case, the group velocities are largely mismatched between $n_g^{\mathrm{RF}}$ and $n_g^{\mathrm{Opt}}$, and the device characteristic impedance $Z_0$ is also typically found far away from the 50 Ω target, leading to narrow EO 3 dB bandwidths

(benchmarked in Supplementary Note S12) and faltering the requirements for high-speed integrated EO applications.

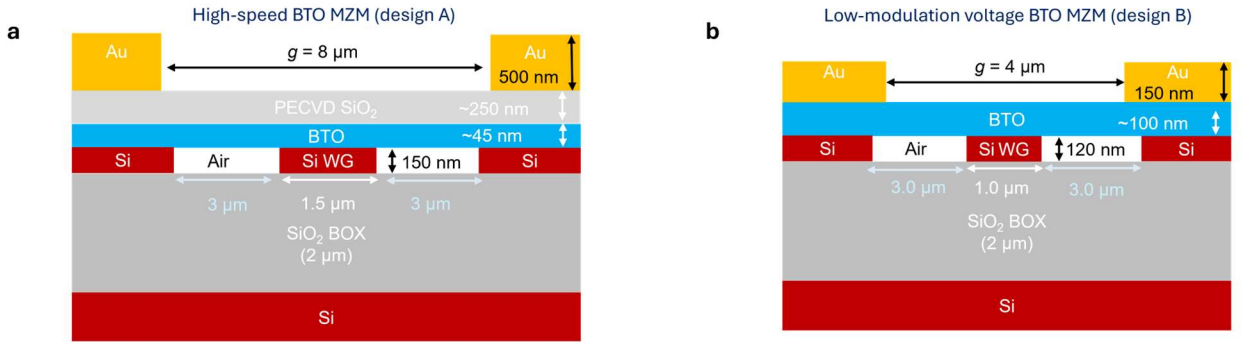


Figure S17. (a) and (b) Device structure schematics for the BTO nanomembranes vdW integrated MZMs shown in Fig. 2k (namely high-speed BTO MZM under device structure 'design A') and Fig. 2h (namely low-speed BTO MZM under 'design B' structure) respectively. PECVD: plasma-enhanced chemical vapor deposition. WG: waveguide. BOX: buried oxide.

To further enhance EO bandwidth, we moderately sacrificed device driving voltage ($V_\pi L$) by increasing the gap distance $g$ between the signal (S) and ground (G) electrodes; a $SiO_2$ layer (with thickness of $t_{SiO2}$) is also inserted between BTO and electrodes, for a better match of $n_g^{RF}$ and $n_g^{Opt}$, as well as catching the 50 Ω target of device characteristic impedance $Z_0$, at the cost of slightly reduced electric field intensity $E^{RF}$ delivered to BTO layer. Group velocity matching is a non-trivial step due to the large discrepancy between the relative permittivity of BTO at microwave ($\varepsilon_{RF} \sim 1000$, with varying values over frequencies[35,37]) and optical ($\varepsilon_{opt} \sim 5.2$) frequencies. The mismatched group velocities and $Z_0$ contribute the major reasons limiting the operation speed of prior BTO-based EO modulators[31]. The simulated (COMSOL Multiphysics) electric field distribution of the high-speed BTO MZM device (with structure illustrated as Fig. S17a) are shown as Fig. S18a. By running parametric sweep optimizations (Fig. S18b, Fig. S18c), the $SiO_2$ layer thickness is selected as $t_{SiO2} = 250$ nm, and the signal electrodes width $w_s$ and height $h_s$ are chosen as 10 μm and 500 nm respectively. Figures S18d-S18e show the simulated microwave (RF) signal loss, device characteristic impedance $Z_0$, microwave signal group index $N_m$, and device 3 dB bandwidth $S_{21}$, respectively. Thicker electrodes may further reduce RF signal propagation loss, while current electrodes thickness $h_s$ ~500 nm is limited by our university cleanroom facilities. We also note that current performances of these proof-of-concept devices shown in Fig. 2 (main text) are primarily limited by device fabrication with further room of improvement (discussed in Supplementary Note S15).

Therefore, we applied a balanced device structure (namely 'design A') to trade device $V_\pi \cdot L$ for a higher EO bandwidth for realizing high-speed BTO MZMs, with reduced electrodes microwave loss (Fig. S19a) and a better catch device impedance $Z_0$ to the target value of 50 Ω (Fig. S19b). Compared to 'design B' (Fig. S17b), device configuration 'design A' (Fig. S17a) exhibits a largely improved theoretical EO 3 dB bandwidth (Figs. S19c-S19f, simulated via COMSOL Multiphysics). The large BTO microwave permittivity, varying BTO Pockels coefficients at higher frequency (Ref.[37]), and especially the non-ideal device electrodes fabrication (Supplementary Note S15) all contribute to the discrepancy between the theoretical and experimental device EO bandwidth, for challenges in designing ideal ultrahigh-speed BTO MZMs. We note that this proof-of-concept 23 GHz experimental 3 dB EO bandwidth for our current BTO MZMs has already outperformed previous works using similar designs (i.e. BTO MZMs)[74-76] (detailed in Supplementary Note S12) with further room of improvement. Compared to prior microring resonators-based BTO EO modulators[35,36,54], the BTO MZMs demonstrated in this work have significantly broader operation spectrum than microring modulators.

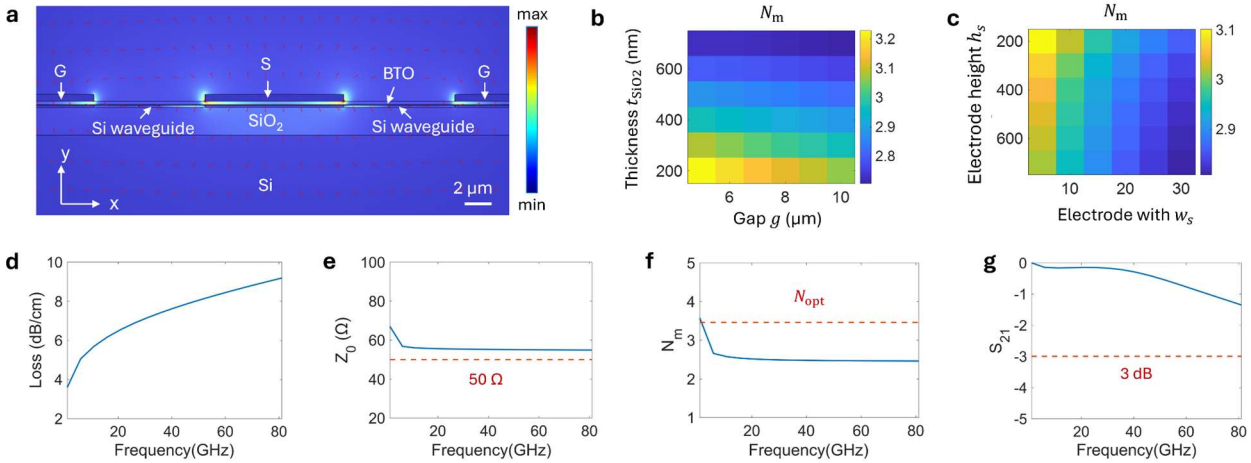


Figure S18. (a) Simulated RF electric field $E^{\mathrm{RF}}$ distribution of the BTO MZM cross-section. S: signal electrode. G: ground electrode. $t_{\mathrm{SiO2}}$: thickness of PECVD $SiO_2$ between BTO layer and electrodes (structure shown in Fig. S17a). (b) Simulated microwave group index $N_m$ as a function of $t_{\mathrm{SiO2}}$ and G-S electrodes gap $g$. (c) Simulated $N_m$ as a function of signal electrode width $w_s$ and height $h_s$. (d)-(g) Simulated microwave loss, characteristic impedance $Z_0$, microwave signal group index $N_m$, and EO 3 dB bandwidth (scatter parameter $S_{21}$ as the ratio of power) as a function of electrical signal frequency, respectively.

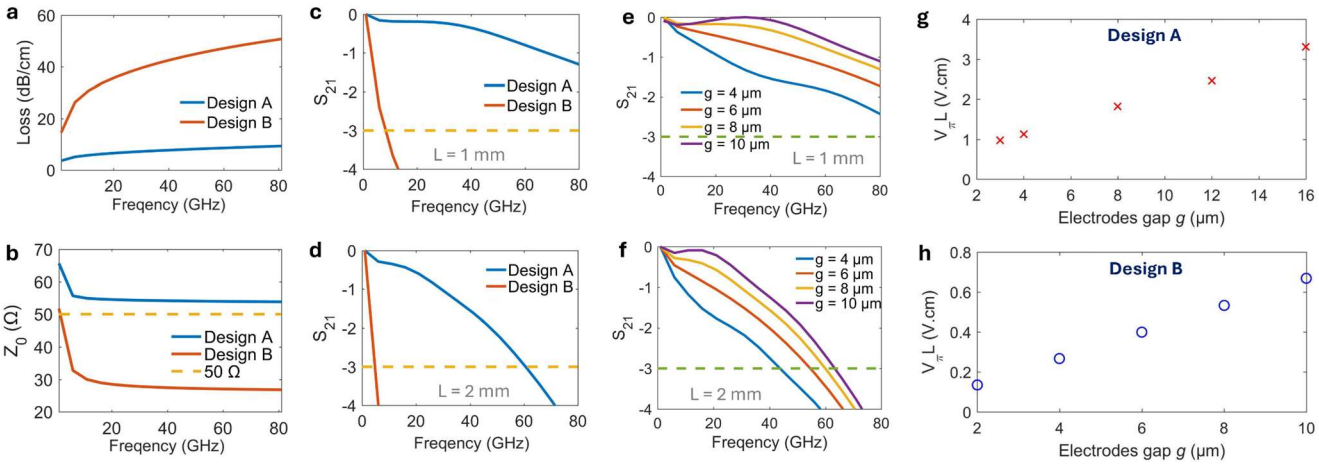


Figure S19. Design trade-offs and benchmarks. (a) and (b) The microwave electrodes loss and device impedance, respectively, as a function of frequency for device structure design A and design B. (c) and (d) scatter parameter $S_{21}$ comparisons for a MZM arm length $L$ of 1 mm and 2 mm, respectively. (e) and (f) $S_{21}$ under different electrodes gap distances $g$ for MZM arm length of 1 mm and 2 mm, respectively. (g) and (h) MZM $V_\pi \cdot L$ as a function of electrodes gap $g$ for device structures design A and B, respectively.

We note that the BTO MZMs in this work are based on hybrid EO waveguide structure, where EO modulation is facilitated via the coupling between the optical field in BTO layer and the Si waveguide core. The spatial modal overlap factor Γ (i.e. the portion of the optical power inside BTO) and the electrodes gap distance $g$ all highly impact the overall device $V_\pi \cdot L$, as the optical power outside EO material cannot contribute to modulation (discussed in Supplementary Note S6). Our current hybrid EO waveguide design can infuse arbitrary desired optical functionalities (e.g. EO modulation) to arbitrary established photonic platforms (e.g. Si photonics) with unparalleled degrees of freedom, and leverage the maturity and high

robustness of current Si and SiN photonic technologies[60,77,78]. If compared to prior hybrid-waveguides-based EO MZMs using LT or LN[77,78], our experimental $V_\pi \cdot L$ values for BTO-MZMs are about 3~6 times (for 'design A') and 12~28 times (for 'design B') lower. Compared to previous publications directly using patterned BTO material as waveguides[79,80], despite their intrinsically higher optical field overlap factor Γ than hybrid EO waveguide configurations, this work still shows better EO modulator $V_\pi \cdot L$, thanks to the significantly higher BTO Pockels coefficients by fundamentally circumventing the lattice mismatch limit in direct BTO heteroepitaxy from those prior works (Supplementary Note S12). If solely pursuing for lower driving voltage, the $V_\pi \cdot L$ for the BTO MZMs in this work can be further reduced below 0.2 V·cm, by altering the electrodes gap distance $g$ at the cost of increased loss and deteriorated device EO bandwidth (Figs. S19g and S19h).

## S11. Rigorous BTO Pockels tensor simulations

Electromagnetic finite-element method (FEM) numerical simulations are performed via COMSOL Multiphysics to probe the impact of BTO effective Pockels coefficient $r_{\text{eff}}$ on device EO modulation. Real device structure parameters are implemented. Coupled FEM simulations are conducted via the following steps.

**Step 1**: Static electric field simulation first calculating the applied electric field distribution $\mathbf{E}_{\text{RF}}(x, y, z)$ via applying bias voltage to signal (S) and ground (G) electrodes.

In this step, BTO is set as constant and isotropic relative permittivity[35,37] $\varepsilon_{\text{RF}} = 1000$ (Supplementary Note S2). Then the external electric field ('**es.Ex**' in COMSOL and other field components) are obtained, where the applied voltage is fixed as $V_0 = 1$ V (Supplementary Fig. S20).

**Step 2**: Electromagnetic (optical) simulation for mode analysis around $\lambda = 1.55$ μm, implementing $\mathbf{E}_{\text{RF}}$ and BTO $r_{\text{eff}}$.

In this step, effective Pockels coefficient is implemented to the refractive index of BTO as $n_{\text{EO}} = n_{(0)} - \Delta n_{\text{BTO}} = n_{(0)} - \frac{1}{2} n_{(0)}^3 r_{\text{eff}} E_{\text{RF}}$, where $E_{\text{RF}}$ is fed by the '**es.Ex**' distribution calculated from **Step 1**. Optical field distribution $\mathbf{E}_{\text{opt}}$ and effective mode indices (after EO modulation) ${n_{\text{eff}}}^{1\text{V}}$, are thus obtained. Only fundamental $TE_0$ mode is considered here. Other guided modes (such as $TM_0$ and $TE_1$) also theoretically exist but have significantly smaller mode index and higher loss compared to $TE_0$ mode.

**Step 3**: Same electromagnetic simulation for mode analysis, but at zero applied electric field $\mathbf{E}_{\text{RF}}(x, y, z) \equiv 0$. In this step, BTO refractive index is set as a constant for $n_{(0)}$ at $\lambda = 1.55$ μm. The simulation yields $TE_0$ mode effective mode index (zero-field) ${n_{\text{eff}}}^{0\text{V}}$.

**Results:**

At half-wave voltage $V_\pi$, the phase modulation at one MZM arm is $\Phi = \frac{2\pi L}{\lambda} \Delta n_{\text{eff}} = -\pi$. Given that $\Delta n_{\text{eff}} = \frac{V_\pi}{V_0} \left( {n_{\text{eff}}}^{1\text{V}} - {n_{\text{eff}}}^{0\text{V}} \right)$, where $V_0 = 1$ V used in simulation, we have the theoretical half-wave voltage product:

$$V_\pi L = \frac{\lambda}{2({n_{\text{eff}}}^{0\text{V}} - {n_{\text{eff}}}^{1\text{V}})} \tag{S11-1}$$

Taking BTO $n_{(0)} = 2.27$ as an example[35,66]:

(1) For low-modulation-voltage BTO EOM (device structure shown as Fig. S17b), by setting BTO effective Pockels coefficient as $r_{\text{eff}} = 928$ pm/V (see Supplementary Note S6), we have the simulated ${n_{\text{eff}}}^{0\text{V}} \approx 2.324199$, ${n_{\text{eff}}}^{1\text{V}} \approx 2.323911$. It corresponds to a calculated $V_\pi L \approx 0.27$ V·cm, roughly agreeing with the experimental value $V_\pi L \approx 0.29$ V·cm.

(2) For high-speed BTO EOM (device structure shown as Fig. S17a), by setting BTO $r_{\text{eff}} = 867$ pm/V (Supplementary Note S6), we have the simulated ${n_{\text{eff}}}^{0\text{V}} \approx 2.521025$, ${n_{\text{eff}}}^{1\text{V}} \approx 2.520983$. It corresponds to a calculated $V_\pi L \approx 1.8$ V·cm (via Eq. S11-1), which is much higher than the experimental $V_\pi L \approx 1.4$ V·cm, indicating an underestimated BTO actual $r_{\text{eff}}$ in this case.

A closer estimation can be reached if we assume BTO $r_{\text{eff}} = 900$ pm/V, yielding a simulated ${n_{\text{eff}}}^{0\text{V}} - {n_{\text{eff}}}^{1\text{V}} \approx 2.521023\text{-}2.52097$, and a calculated $V_\pi L \approx 1.5$ V·cm agreeing well with the experimentally measured value. The simulated optical field distributions of one BTO MZM arm are shown as Fig. S20.

(3) Discussions: This estimation method eliminates the disadvantage of high sensitivity of predicted $r_{\text{eff}}$ on the value of modal overlap factor Γ manifested in Supplementary Note S6. Nevertheless, the results of this approach still depend on the selected value of $n_{(0)}$.

If taking $n_{(0)} = 2.26$ into simulation[37], for the low-modulation-voltage BTO MZM structure, setting $r_{\text{eff}} = 950$ pm/V, we have the simulated ${n_{\text{eff}}}^{0\text{V}} \approx 2.321985$, ${n_{\text{eff}}}^{1\text{V}} \approx 2.321696$, and calculated $V_\pi L \approx 0.27$ V·cm.

For high-speed BTO MZM structure, setting $r_{\text{eff}} = 900$ pm/V, we have the simulated ${n_{\text{eff}}}^{0\text{V}} \approx 2.524113$, ${n_{\text{eff}}}^{1\text{V}} \approx 2.524069$, corresponding to a calculated $V_\pi L \approx 1.7$ V·cm.

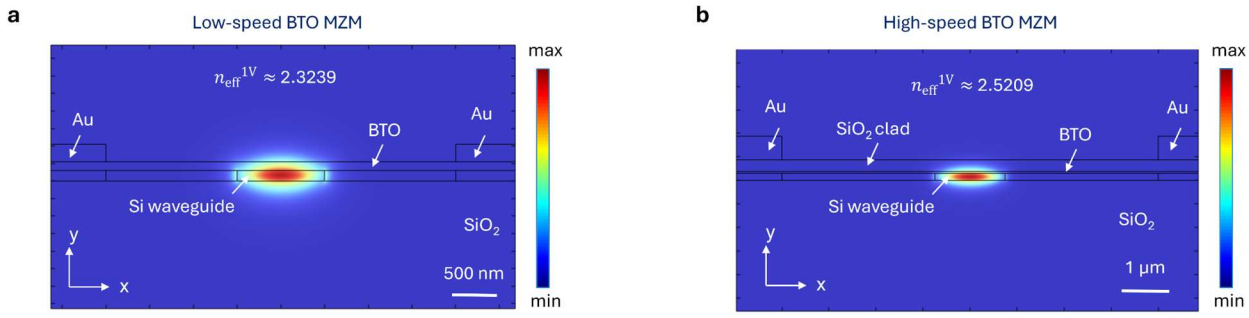


Figure S20. Coupled electromagnetic simulations implementing both RF electric field and BTO Pockels coefficients for optical fields (at wavelength $\lambda = 1550$ nm) for the low-speed (a) and high-speed (b) BTO MZMs. The explicit device structures for panels (a) and (b) are shown in Fig. S17b and S17a respectively.

## S12. Benchmarks for BTO $r_{\text{eff}}$ details

Photonic vdW integration[25] permits optimal single-crystalline functional nanomembranes available for heterogeneous integration to arbitrary photonic substrates with precisely controlled film thickness and well-defined crystallographic orientations. This feature becomes critical, especially when crystal quality and orientation drastically impact material and device performance, such as the EO Pockels material BTO. Supplementary Fig. S21 gives the benchmark details for main text Figs. 5a and 5b, with corresponding references marked near the scattered plots. The single-crystallinity with well-controlled crystallographic $c$-axis orientation (which drastically impact EO performance), and the artificially delaminated freestanding form of the BTO nanomembranes (for boundless heterogeneous integration to arbitrary established photonic substrates) are the two crucial factors to enable the record-setting Pockels response for the vdW-integrated BTO photonic devices demonstrated in this work obviating prior lattice-mismatch limits[79].

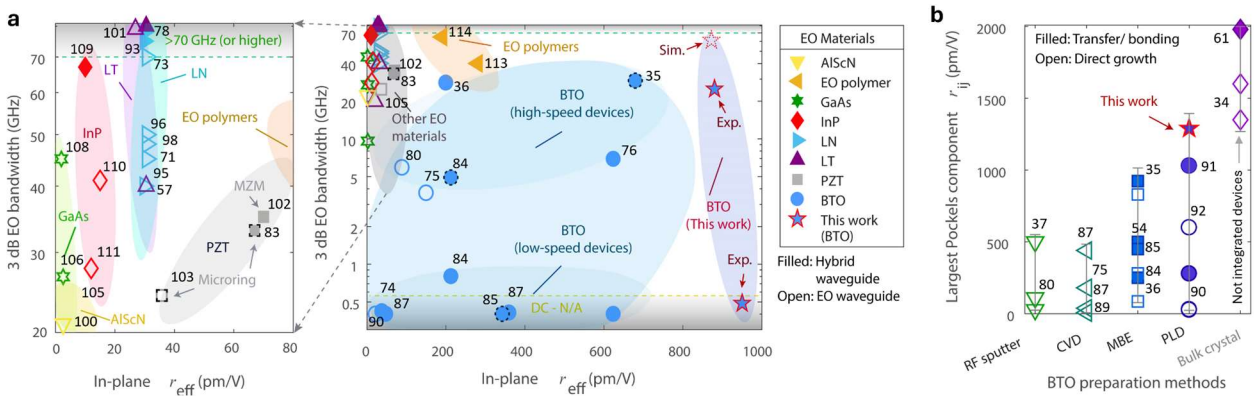


Figure S21. (a) Benchmark details for BTO-based EO modulators. Hybrid waveguides are marked with filled symbols (defined in the notes after Table S1), otherwise open symbols are applied. Symbols with dashed outlines represent microring structures-based EO modulators, while solid-outlined symbols denote MZI-based EO modulators. (b) Benchmarks on the reported largest Pockels tensor component $r_{ij}$ made by different BTO growth methods. Open symbols represent directly grown BTO on various substrates or structures, while filled symbols denote transferred or bonded BTO layers.

Leveraging vdW integrated single-crystalline *a*-axis-domain BTO nanomembranes, desired EO functionality is infused to well-established Si photonics. We experimentally demonstrated giant in-plane effective Pockels coefficient $r_{\text{eff}}^{\parallel}$ approaching 950 pm/V, corresponding to an estimated largest Pockels tensor component $r_{42}$~1290 pm/V (Supplementary Note S6), with measured half-wave voltage and device length product $V_\pi L$ around 0.29 V·cm. Another modified high-speed BTO MZM showcased strong $r_{\text{eff}}^{\parallel}$ around 880 pm/V (corresponding to an estimated $r_{42}$~1190 pm/V) and a decent proof-of-principle EO 3 dB bandwidth of 23 GHz (Supplementary Note S15). Detailed electromagnetic simulations agree with our Pockels coefficient estimation (Supplementary Note S11). The resultant Pockels coefficient is over 40 times higher than current mainstream EO material lithium niobate (LN)[67,71-73], and around 5~20 times higher than PZT[81-83].

Table S1 – Benchmarks of reported EO materials and devices.

| EO Material | Hybrid waveguide | Structure | $r_{\text{eff}}^{\parallel}$ (pm/V) | Largest $r_{ij}$ (pm/V) | $V_\pi \cdot L$ (V·cm) | EO 3dB BW (GHz) | Notes on material preparations | Ref |
|---|---|---|---|---|---|---|---|---|
| BTO | Yes (Si–BTO) | Microring | 680* | 923 | — | 30 | MBE BTO on Si with engineered STO buffer. | 35 |
| BTO | Yes (Si–BTO) | MZI | 213 | — | 1.5 | 0.8 | MBE BTO on SOI with engineered STO buffer layer. Top Si hybrid slab WG. | 84 |
| | | Microring | — | — | — | 4.9 | | |
| BTO | Yes (Si–BTO) | Microring | 380 | — | — | 12* | Molecular wafer bonding. | 54 |
| BTO | Yes (Si–BTO) | MZI | 48 | — | 1.67 | — | Transferred freestanding c-axis BTO. | 74 |
| BTO | Yes (Si–BTO & SiN-BTO) | Microring MZI | 200 | — | 5 | ~30* (ring) ~20 (MZI) | MBE BTO on Si with engineered STO buffer. | 36 |
| BTO | Yes (SiN–BTO) | Microring | 343 | — | 0.3 | DC/NA | MBE BTO on Si with engineered STO buffer. | 85 |
| BTO | Yes (SiN–BTO) | MZI | 360 | — | 0.5 | DC/NA | MOCVD BTO on MgO. | 86 |
| BTO | Yes (SiN–BTO) | MZI | 38 | — | 4.5 | DC/NA | MOCVD BTO on MgO. | 87 |
| BTO | Yes (SiN–BTO) | MZI | 624* | > 1000$^{\perp}$ | 0.62 | 6.9 | BTO growth with engineered STO buffer. | 76 |
| BTO | N/A | N/A | 388* | <500* | — | — | RF sputtered BTO on $SiO_2$ with buffer. | 37 |
| BTO | N/A | N/A | 121 | — | — | — | ALD BTO on STO with $BaSnO_3$ buffer layer. | 88 |
| BTO | N/A | N/A | 55~160* | 1980$^{\perp}$ | — | $5.92\times10^{-4}$ * | Mechanical spalling from bulk BTO. | 61 |
| BTO | N/A | N/A | 7 | 6.2 ($r_{33}$) | — | — | CVD BTO film microstructures. | 89 |
| BTO | No | MZI | 22 | — | 5.7 | — | Poly-crystal BTO grown on glass. | 90 |

| | | | | | | | | |
|---|---|---|---|---|---|---|---|---|
| BTO | No | MZI | 162 | — | 0.54 | — | RF sputtered BTO with STO buffer layer. | [79] |
| BTO | No | MZI | 150 | — | 1.248 | 3.7 | MOCVD BTO on MgO. | [75] |
| BTO | No | MZI | 89 | — | 2.32 | > 5.9* | RF sputter BTO on SOI. | [80] |
| BTO | No | MZI | — | 390 ~1030* | — | — | PLD BTO on MgO. | [91] |
| BTO | No | N/A | — | 600* | — | — | PLD BTO on DSO for polarization rotator. | [92] |
| BTO (This work) | Yes (Si–BTO) | MZI | 928~950 | 1250~1290 | 0.29 | DC/NA | Measured at 1 kHz. Limited by TWE. | \ |
| | | | 867~880 | 1160~1190 | 1.44 | 23 | Limited by device TWE fabrication. | |
| | | | 880 | 1190* | — | > 60* | Simulated EO 3 dB BW for 1-mm device. | |
| LN | Yes (SiN–LN) | MZI | — | 30.9 | 8.2~8.8 | — | Wafer bonding LNOI with SiNOI. | [60] |
| LN | Yes (SiN–LN) | MZI | — | 30.9 | — | ≈100 | Wafer bonding LNOI with SiNOI. | [93] |
| LN | Yes (Si–LN) | MZI | — | 30.9 | 6.7 | >100 | Wafer bonding LNOI with SOI. | [94] |
| LN | No | MZI | — | 30.9 | 1.29 | >40 | LN WG based on LNOI. | [95] |
| LN | No | MZI | — | 30.9 | 2.16 | >50 | LN WG based on LNOI. | [96] |
| LN | No | MZI | — | 30.9 | 2.8 | >45 | LN WG based on LNOI. | [71] |
| LN | No | MZI | — | 30.9 | — | >110 | LN WG based on LNOI. | [97] |
| LN | No | MZI | — | 30.9 | 2.5 | >70 | LN WG based on LNOI. | [73] |
| LN | No | MZI | — | 30.9 | 2.47 | ~48 | LN WG based on LNOI. | [98] |
| LN | No | MZI | — | 30.9 | 3.67 | 22 | LN WG based on LNOI. | [99] |
| LT | Yes (SiN–LT) | MZI | — | 30* | 4.08 | ~100* | Wafer bonding LTOI with SiNOI. | [60] |
| LT | Yes (SiN–LT) | MZI | — | 30* | 3.5 | > 70 | Micro-transfer of LT lifted off from LNOI | [78] |
| LT | No | MZI | — | 16.9 | 0.0351 | > 20 | LT WG based on LTOI. | [100] |
| LT | No | MZI | — | 16.9 | — | 110 | LT WG based on LTOI. | [101] |
| LT | No | MZI | — | 30* | 1.9 | 40 | LT WG based on LTOI. | [57] |
| PZT | Yes (SiN–PZT) | Microring | 67 | 100* | 3.2 | 33 | CSD grown PZT on SiN with seed layers. | [83] |
| PZT | Yes (Si–PZT) | MZI | 70* | 67 | 3.2 | ~30 | CSD grown PZT on SiN with seed layers. | [102] |
| PZT | No | Microring | 35.8 | 100* | 1.17 | 24.9 | Wafer bonding of PZT. | [103] |
| Si* | No | MZI | 10~80* | — | — | 10 | Strained Si with SiN. (No EO for normal Si) | [104] |
| AlScN | No | MZI | 1~2.86* | — | 3.12 | 22 | Direct growth of AlScN. | [105] |
| GaAs | No | MZI | 2* | — | 9 | 27 | Monolithic GaAs modulator. | [106] |
| GaAs | No | MZI | 2* | — | — | 9.6 | Epitaxial GaAs structures and design. | [107] |
| GaAs | No | MZI | — | — | — | >40* | Epitaxial GaAs. | [108] |
| InP | Yes (Si–InP) | MZI | — | — | — | >67 | Direct MOVPE InP with deposited Si layer. | [109] |
| InP | No | MZI | — | <30 | 0.68 | 41 | Epitaxial InP. | [110] |
| InP | No | MZI | — | — | — | 28 | Epitaxial InP. | [111] |
| EOP | Yes (plasmonic) | MZI | — | 1000 | 0.01 | >500 | EO polymers in plasmonic structure. | [112] |
| EOP (JRD1) | Yes | MZI | — | 200~390* | 0.26 ~0.41 | 40 | EO polymer (JRD1) on Si. | [113] |
| EOP (YID124) | Yes | MZI | — | 180~300* | 1.3 | >67 | EO polymer (YID 124) on Si. | [114] |

Notes: (1) Abbreviations: Barium titanate (BTO), lithium niobate (LN), lithium tantalate ($LiTaO_3$), lead zirconate titanate (PZT), aluminum scandium nitride (AlScN), gallium arsenide (GaAs), indium phosphide (InP), dysprosium scandate (DSO or $DyScO_3$), electro-optical (EO) polymers (EOP) such as JRD1, and YID124 (Ref.[115]), Mach-Zehnder interferometer (MZI), bandwidth (BW), waveguide (WG), Metalorganic vapor-phase deposition (MOCVD); metal-organic vapor-phase epitaxy (MOVPE); pulsed laser deposition (PLD); chemical solution deposition (CSD); Atomic layer deposition (ALD); travelling wave electrode (TWE); effective in-plane Pockels coefficient ($r_{\text{eff}}^{\parallel}$), half-wave voltage length product ($V_\pi \cdot L$). (2) For hybrid waveguide classification, if the waveguide is made solely by EO material, such as LNOI (LN-on-insulator) and LTOI (LT-on-insulator), it is classified as not hybrid waveguide. Otherwise, it is ascribed as a hybrid waveguide structure (marked as high-index waveguide material–coupled to functional EO material, such as Si-LN). (3) Superscripts: only in-plane Pockels coefficients $r_{\text{eff}}^{\parallel}$ (crucial for chip-integrated EO applications) are benchmarked in the Table. Superscript $^{\perp}$ denotes out-of-plane (perpendicular to film) Pockels coefficients $r_{ij}$. Superscript $^{*}$ denotes estimated value. (4) For the largest reported Pockels components $r_{\text{ij}}$, by default $r_{42} = r_{51}$ is reported, otherwise the exact

Pockels tensor component is marked out beneath the number (such as $r_{33}$). '—' denotes no explicit values were reported by the reference. (5) For EO bandwidth, DC/NA denotes low-frequency (like direct-current to kHz-level) measurements are performed or reported. Experimental setup (such as photodetector or vector network analyzer/VNA) limited EO 3dB bandwidth measurements are marked out, for example > 67 GHz.

Table S1 manifests the benchmarks details shown in Fig. S21, showcasing a clear supremacy of BTO over other EO materials in terms of the Pockels coefficient value[33]. Given the integrated photonics background, we note that only *in-plane* Pockels coefficients $r_{\text{eff}}^{\parallel}$ are focused here on Table S1, as *out-of-plane* effective Pockels coefficients generally cannot be effectively probed in integrated photonic chips with planar electrodes structures[34,35,54,70]. For references with reported device structures and $V_\pi L$, the $r_{\text{eff}}^{\parallel}$ can be estimated via Eq. (S6-2). For instance, in Ref.[76], the reported $r_{\text{eff}}$ are measured via free-space optics and perpendicular to film plane. Taking the device structure parameters (extracted from Fig. 5e in Ref[76] with scale bar and related discussions) as: $Si_3N_4$ (SiN) waveguide width × height as 1 μm × 260 nm (estimated), reported electrodes gap $g$ as 10 μm, BTO thickness as 135 nm, $SiO_2$ thickness between SiN waveguide and BTO around 150 nm, and ($> 1$ μm) $SiO_2$ cladding atop BTO, the modal overlap factor can be calculated as $\Gamma \approx 34.7\%$, by setting $Si_3N_4$ refractive index as 2.0 and BTO refractive index[33,37] as $n_{(0)} = 2.26$. By further feeding the reported experimental $V_\pi L = 0.62$ V·cm to Eq. (S6-2), the in-plane effective Pockels efficient can thus be estimated[76] as $r_{\text{eff}}^{\parallel} = \frac{\lambda g}{n_{(0)}^3 \Gamma V_\pi L} \approx 624$ pm/V.

## S13. Supplementary HR-TEM data for BTO MZMs

Selected area electron diffraction (SAED) pattern was taken from the BTO film via JEOL 2100F transmission electron microscope (TEM) and calibrated against the SAED pattern taken from the Si wafer substrate at the same TEM condition to ensure the accuracy of $d$ spacing measurements for the right panel of main text Fig. 2j. The relative orientation of the diffraction vector [100] and the film is confirmed via the shadow image in a defocused convergent beam electron diffraction pattern that confirms the [100] diffraction points perpendicular to the film in the out of plane direction. This further confirms the $a$-axis-domain BTO besides the XRD and RSM measurements.

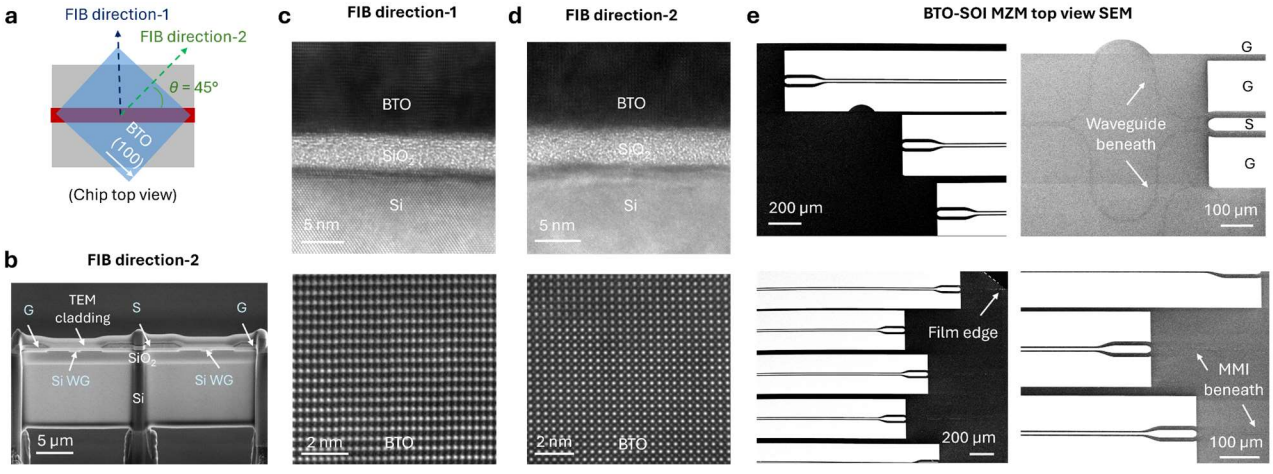


Figure S22. (a) Illustration on the two FIB directions along the photonic chip sample. (b) SEM of the cross-sectional sample (along FIB direction-2) for HR-TEM showing two MZM waveguide arms, BTO layer, and electrodes. S: signal. G: ground. (c) and (d) HR-TEM (top panels) and HAADF-STEM images (bottom panels) for the BTO-Si waveguide interface along FIB direction-1 (c) and direction-2 (d) respectively. (e) Top view SEM images of the fabricated BTO MZMs chip.

The high-resolution (HR)-TEM photos also depend on the focused ion beam (FIB) direction. Figure S22a illustrates the two FIB directions used to prepare the TEM samples: one is perpendicular to the waveguide, while the other has an angle around $\theta \approx 45°$ with respect to the waveguide (i.e. parallel to the epitaxial edge of BTO film). An exemplary TEM sample (cleaved along FIB direction-2) is illustrated as Fig. S22b, showing the two waveguide arms of the MZM and the signal (S) and ground (G) electrodes (with device structure detailed in Fig. S17). The HR-TEM images along the BTO-Si waveguide interfaces along FIB direction-1 and direction-2 are shown as the top panels of Figs. S22c and S22d respectively with clear BTO lattice fringes. The corresponding high-angle annular dark-field scanning transmission electron microscopy (HAADF STEM) images of the BTO layers are shown as lower panels.

The top-view SEM images of the BTO vdW-integrated EO MZMs are shown in Fig. S22e, where the Si waveguide patterns can be seen beneath the heterogeneous integrated BTO layer. The EDS SEM images of the two TEM samples with different FIB cleavage directions are shown in Fig. S23.

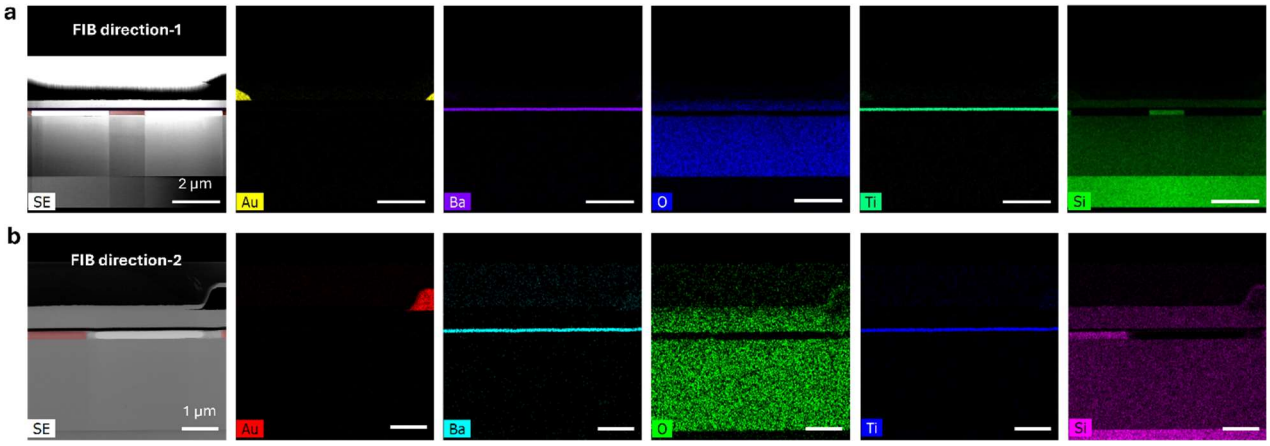


Figure S23. (a) and (b) STEM-EDS images for the two TEM samples along FIB direction-1 (a) and direction-2 (b) respectively. The left-most panels are the corresponding second-electron (SE) bright-field STEM images, where the Si waveguides are manually colored in red.

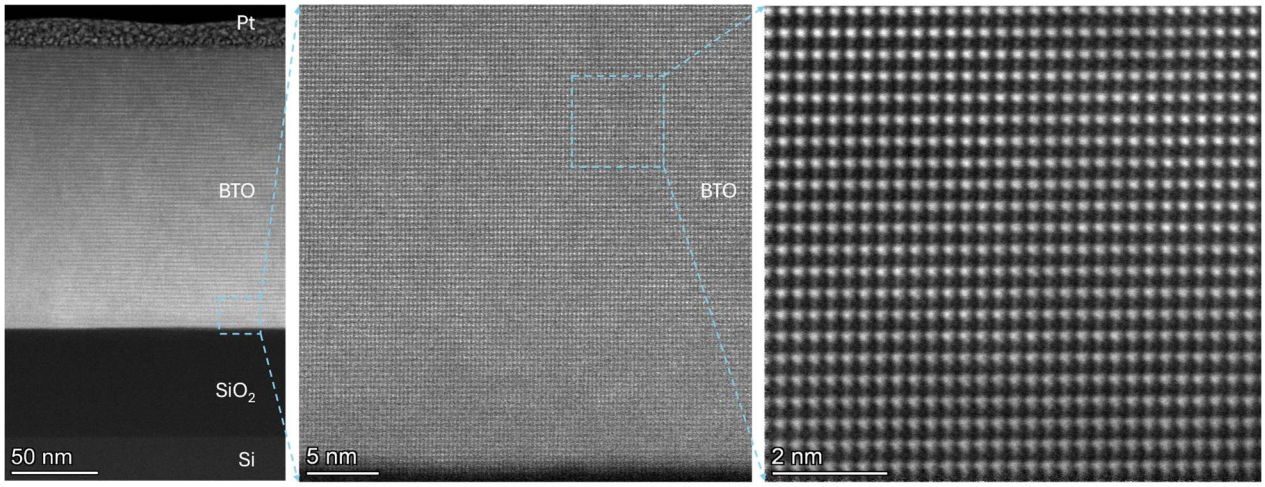


Figure S24. High-resolution scanning transmission electron microscopy (HR-STEM) for the cross-section of the single-crystalline freestanding BTO film vdW-integrated to $SiO_2$/Si substrate.

## S14. BTO crystal quality and intrinsic BTO material loss

High-resolution scanning transmission electron microscopy (HR TEM) is performed to validate the single-crystallinity of the vdW-integrated BTO nanomembranes with minimal crystallization defects (Fig. S24, Methods). The introduction of SAO sacrificial layer enables the delamination of freestanding BTO nanomembranes for boundless heterogeneous photonic integration on arbitrary substrates, which can achieve previously inaccessible crystal quality with well-controlled BTO crystallographic orientations via conventional heteroepitaxial approaches[31,35,36,54,80,91].

High-angle annular dark-field (HAADF)-TEM also confirmed the high crystal quality of the as-grown BTO/SAO/STO samples before transfer with desired $a$-axis-domains vital for integrated EO applications (Fig. S25). The rapid degradation of SAO layer (sensitive to humidity and oxygen) under zoomed-in electron beams during TEM was observed, followed by partially vanished SAO layer lattice fringes after repeated focus adjustment and imaging. We also further characterized the threading dislocation density (TDD) of the as grown BTO film (i.e. BTO/ SAO/STO sample) via electron channeling contrast imaging (ECCI), confirming low TDD around $1.35 \times 10^7 \sim 4 \times 10^7$ cm$^{-2}$ (Fig. S26, where the threading dislocation defects are marked out in blue dashed circles for Fig. S26a only) indicating high-quality BTO nanomembranes.

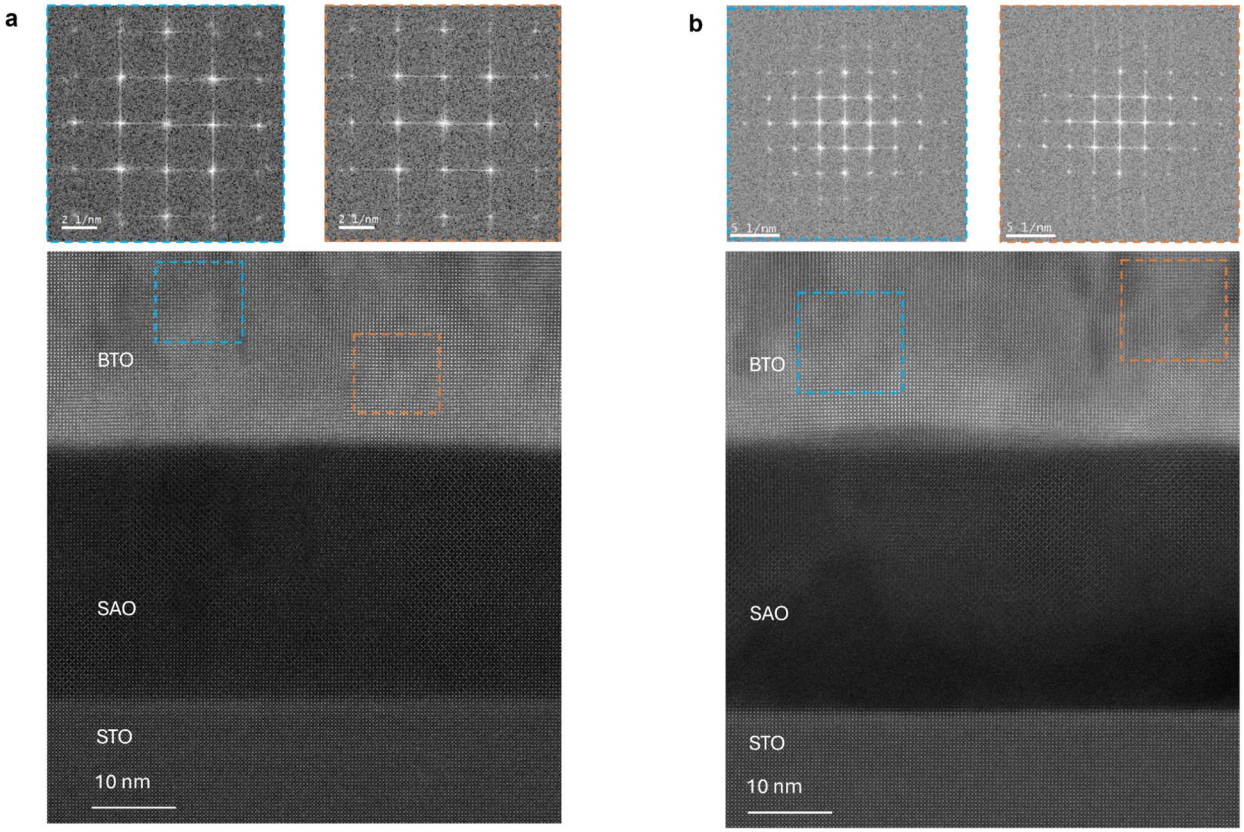


Figure S25. HR-STEM for as grown BTO /SAO/STO samples. The SAO sacrificial layer was degraded due to electron beam and ambient oxygen/humidity exposure during sample transfer and storage. The ununiform brightness contrast is due to nonideal FIB thinning process for TEM sample preparations. Top panels: corresponding fast Fourier transform (FFT) diagrams.

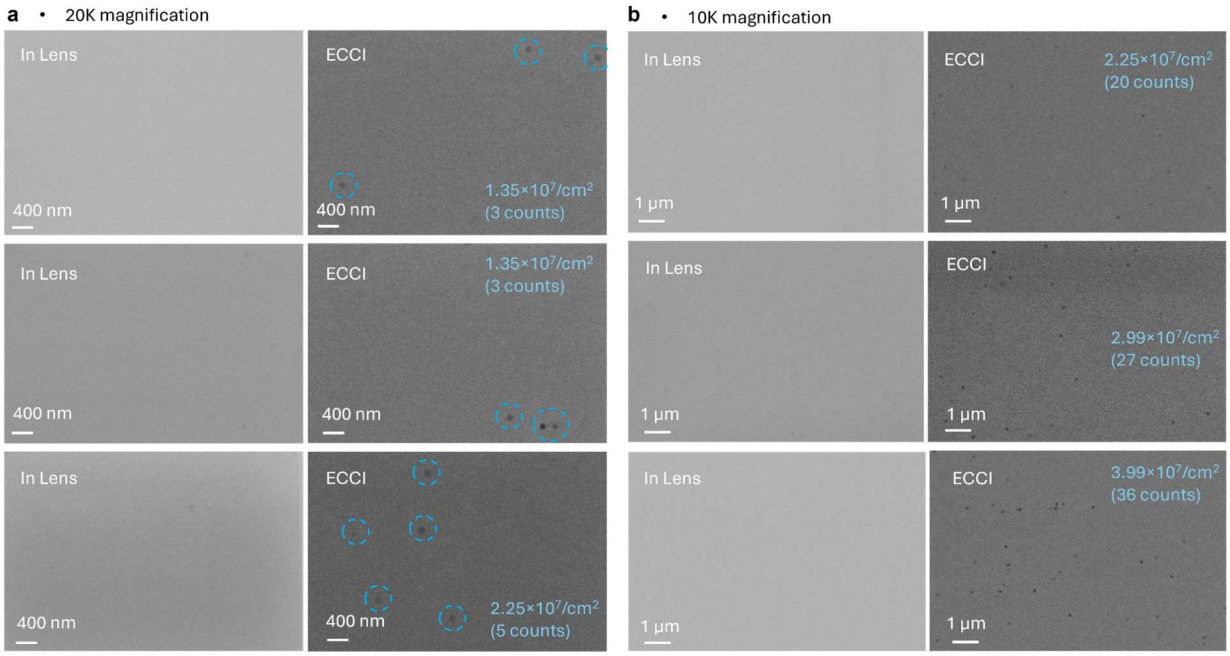


Figure S26. Electron channeling contrast imaging (ECCI) for as grown BTO/SAO/STO samples with (a) 20,000 and (b) 10,000 magnifications, respectively, showing low BTO film threading dislocation density.

Spectroscopic ellipsometry (J.A. Woollam alpha-SE Spectroscopic Ellipsometer) is also performed to characterize the intrinsic material loss of BTO (via an 80 nm-thick BTO as-grown BTO film on STO substrate with thin interlayer). The measured BTO complex refractive indices $(n, k)$ are shown in Fig. S27a with good model fit (Fig. S27b). The measured BTO $k$ at 890 nm (limited by the maximum tool measurement range) is about $2 \times 10^{-6}$, corresponding to an optical loss about 1 dB/cm at 890 nm wavelength. Further variable angle spectroscopic ellipsometer (VASE) measurements via another SE tool (J.A. Woollam VASE) also confirms lower BTO intrinsic material loss[33] at the telecom wavelengths. The measured BTO $k$ at 1550 nm wavelength is around $2 \times 10^{-7}$, corresponding to a low BTO material loss of about 0.07 dB/cm, which is enabled by the high-quality of the freestanding BTO films and this loss remains low for majority of integrated photonic applications. The source of additional optical loss mainly comes from the 3D nanomembrane transfer and subsequent nonideal device fabrication processes.

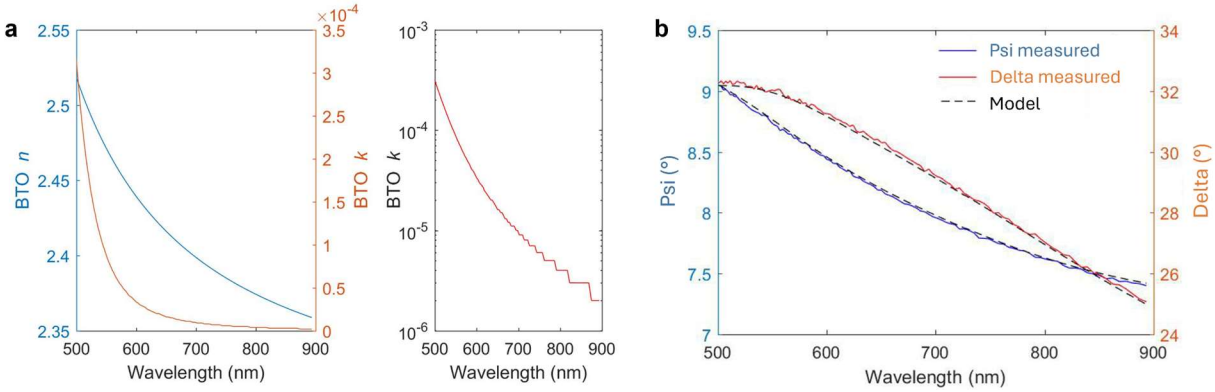


Figure S27. (a) Spectroscopic ellipsometer (SE) measured BTO film complex refractive indices $(n, k)$ (left panel) and replotted BTO $k$ in logarithmic $y$-scale (right panel). The stairs-like shape in BTO $k$ curve is due to the limited SE tool measurement resolution in $k$ and the logarithmic scale plot in $y$-axis. (b) SE model fit.

## S15. Supplementary high-speed BTO MZMs measurement data

The experimental setup for high-speed EO MZMs is shown in Fig. S28a (and Methods), where the EO scattering parameter $S_{21}$ (as ratio of powers) was characterized by a 67 GHz vector network analyzer (VNA, R&S ZNA67).

The microwave measurements of the high-speed BTO MZMs are shown as Figs. S28b-S28e. The discrepancy between measured and designed device performances is mainly ascribed to the imperfect travelling-wave electrodes fabrication with non-vertical side walls due to cleanroom facility constraints (Supplementary Note S9), which can induce additional losses and can be also evidenced by the partially collapsed nonideal electrode edges shown in the SEM images of Fig. 2i (in main text), Fig. S22b and Fig. S23 (left panels). Nevertheless, an over 23 GHz EO 3 dB bandwidth is still experimentally confirmed despite nanofabrication imperfections (Fig. S29). The estimated edge coupling loss (without chip facet polishing limited by facility) is about 6~8 dB per facet, and the measured total fiber-to-fiber loss is around 18~22 dB depending on chip dicing. Compared to wafer bonded LN and LT to Si and SiN photonics (with sophisticated and lengthy substrate grinding, polishing, and etching processes), the heterogeneous integration of BTO is still in its early stages, with comparatively higher optical loss for the BTO hybrid waveguides as reported in prior works[35,36,54,85,116]. These proof-of-concept results can be further enhanced in optical coupling by applying professional foundry-based photonic chips, with mitigated optical loss by further enhancing device fabrication and optimizing the 3D nanomembrane transfer integration setups and processes to unlock broader applications and impacts. Asymmetric optical phase modulation is also observed (Figs. S29c) due to ferroelectric material BTO, which could be further exploit to develop photonic memories[117] but beyond the scope of this paper. Detailed device EO bandwidth characterization data (supplementary for Fig. 2k in main text) are shown in Figs. S29d and S29e, where increasing microwave signal reflection was observed at high frequencies due to the mismatched target device characteristic impedance $Z_0$ to the 50 Ω target, leaving further room for improvements in future works.

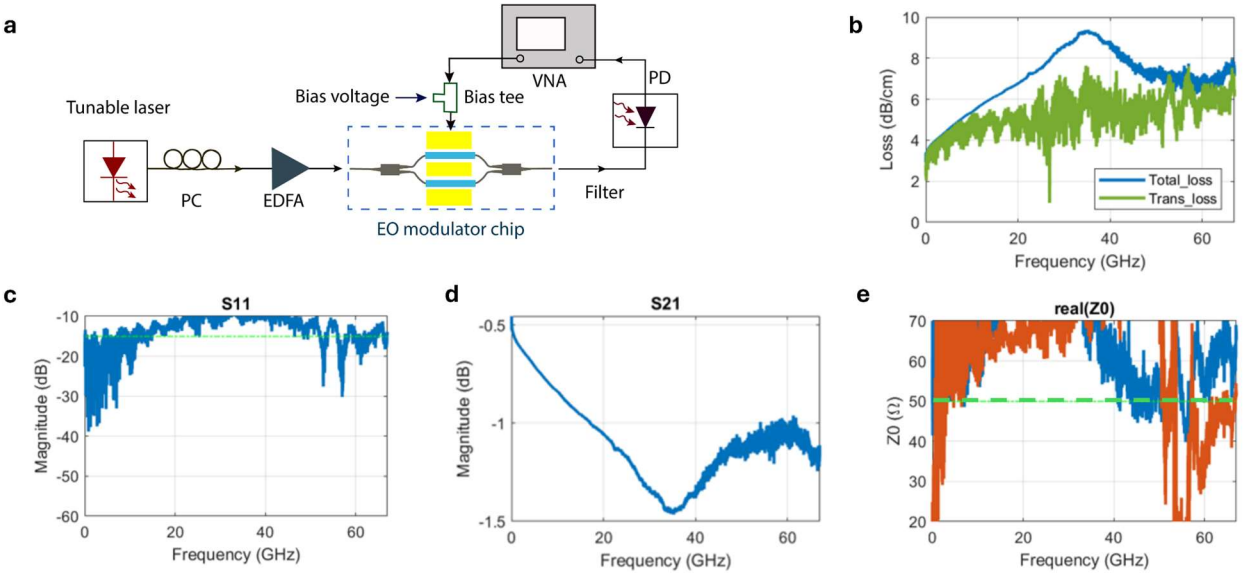


Figure S28. (a) High-speed EO modulator measurement setup. (b) Measured electrodes microwave transmission (trans) and total loss. (c) and (d) Measured microwave reflection ($S_{11}$) (c) and transmission ($S_{21}$) (d) ratio of the fabricated electrodes, respectively. (e) Measured device characteristic impedance $Z_0$.

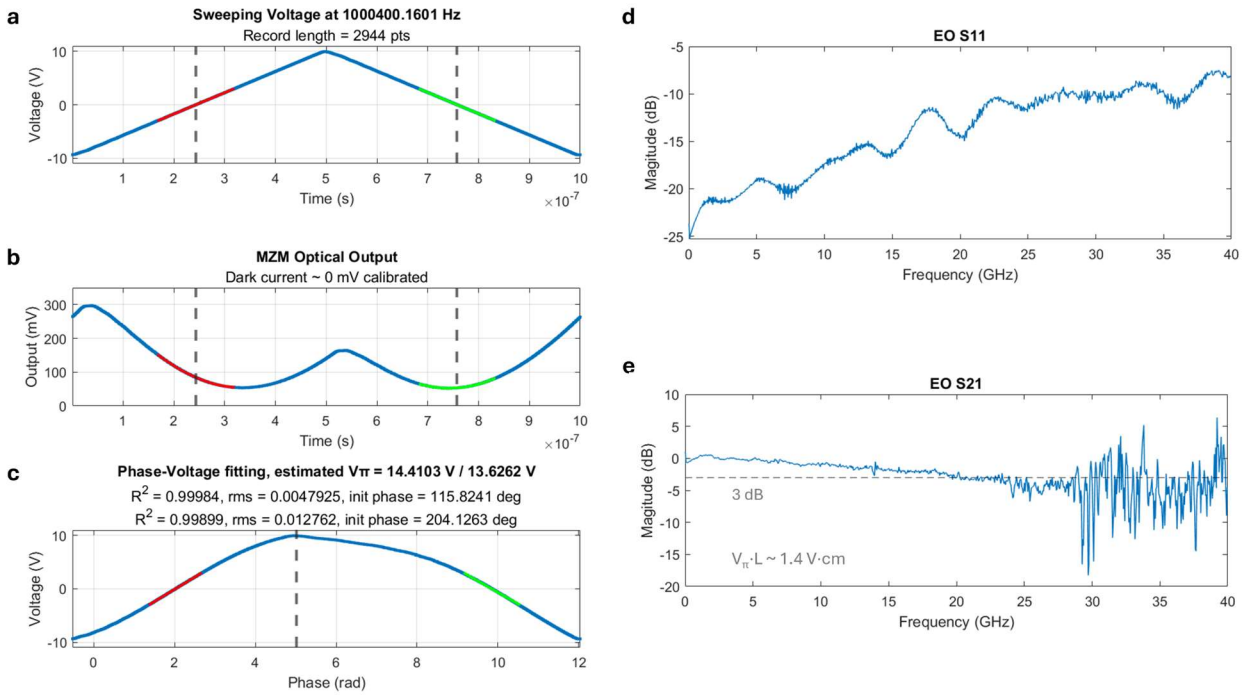


Figure S29. (a) Sweeping triangular voltage signal. (b) and (c) Corresponding optical output of the BTO MZM by the photodetector (b), and device phase voltage fitting (c), respectively. (d) and (e) Measured EO reflection ($S_{11}$) (d) and transmission ($S_{21}$) (e) as a function of signal frequency, respectively. Device modulation length $L$ is 1 mm.

## S16. Details for remote epitaxial GaN

Besides conventional layer transfer steps discussed in Fig. S1 and Supplementary Note S1, additional attention is required when high-stress-level metal adhesive layers are used. For the single-crystalline unintentionally-doped (UID) GaN film grown by remote epitaxy via molecular beam epitaxy (MBE, detailed in Methods)[3,11], high-stress-level Ti/Ni adhesive layers are needed to overcome the strong adhesive energy between the in-situ grown BN and substrate to facilitate efficient nanomembrane exfoliation (Fig. S4). The strong strain in the Ti/Ni layer prohibits uniform vdW integration, leading to detached or rolled up nanomembranes after retrieving the thermal release tape (TRT) supporting layer.

To address this issue, another polymer handler such as PPC or PMMA was spin coated to the exfoliated GaN nanomembranes, followed by the TRT removal by soft baking and Ti/Ni stressor layer etching (Fig. S4). Upon the removal of the high-stress-level Ti/Ni adhesive layers, the freestanding GaN nanomembranes are cleaned and subsequently transferred to target photonic chips with uniform and robust layer bonding to the photonic chips to develop heterogeneous integrated photodetectors.

The impact of defects reduction through remote epitaxial GaN (Figs. S30a, S30b) is further compared to conventional direct epitaxial GaN (Figs. S30c, S30d), showing reduced threading dislocation density (TDD) via electron channeling contrast imaging (ECCI) characterizations thanks to the spontaneous relaxation on 2D-covered interfaces[13]. The two samples (Figs. S30b, S30d) are grown together in same batch via MBE (Methods) for a quick benchmark, where the TDD can be further suppressed for carefully optimized 2DLT GaN nanomembranes (Figs. S30e)[3,11].

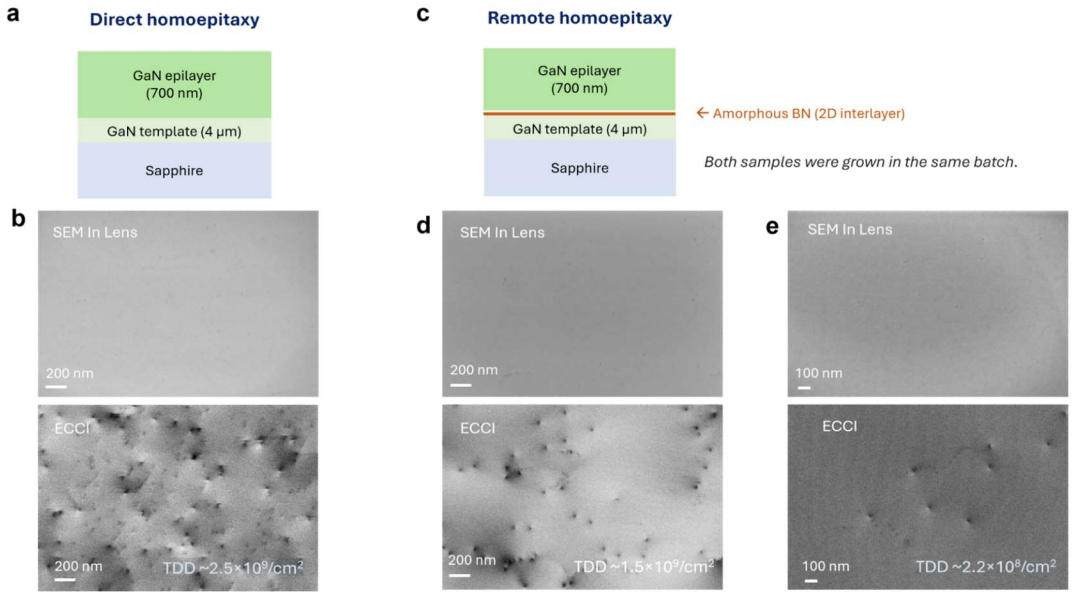


Figure S30. Comparison of direct- and remote epitaxial-GaN films defects density. (a) Direct GaN epitaxy. (b) SEM (top) and electron channeling contrast imaging (ECCI, bottom panel) showing threading dislocation density (TDD). (c) GaN remote epitaxy with 2D interlayer. (d) SEM and ECCI of the remote epitaxial GaN with reduced TDD. (e) SEM and ECCI of another optimized remote epitaxial GaN film.

## S17. Additional TEM data for GaAs and GaN photodetectors

Besides the TEM images in main text Fig. 3b and 3h, the zoom-in HR-TEM details of the GaN and GaAs nanomembranes are shown in Fig. S31a, verifying excellent single-crystalline quality. The STEM-EDS composite maps of the constituent elements for the vdW-integrated GaAs (with p-i-n doping structures shown in Fig. S3a) are given in Fig. S31b.

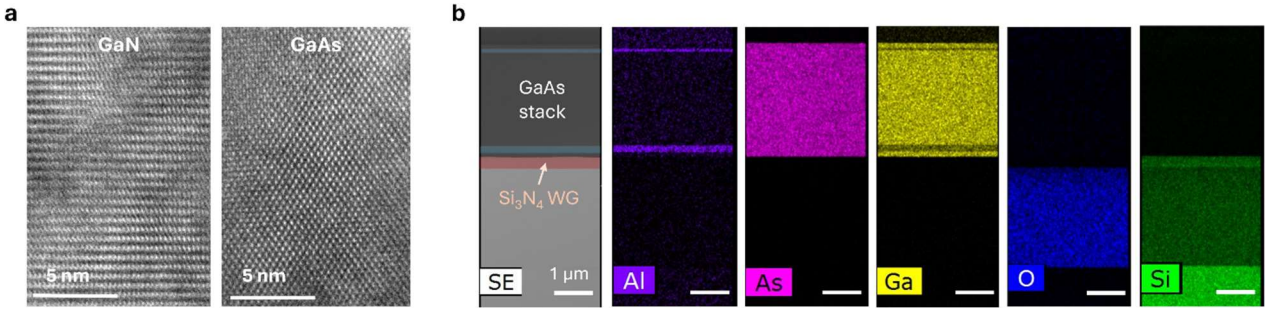


Figure S31. (a) HR-TEM images for the vdW-integrated GaN (left) and GaAs (right) nanomembranes. (b) EDS SEM of vdW-integrated freestanding GaAs atop SiN waveguide. In the left-most second electron (SE) SEM panel, the SiN and AlGaAs layers are colored as red and blue colors respectively.

## S18. III-V-SiN photodetector samples details

The device structures are illustrated in Fig. S32a, where the etching trenches $d_t$ for the SiN waveguide are 2.5 μm, waveguide width × height as 1 μm × 220 nm. Bottom electrodes spacing $g_b$ and thickness $h$ are 6 μm and 30 nm respectively, and top electrodes spacing as $g_t$ varying from 2~5 μm between different devices. Limited by current cleanroom facilities, only GaAs films were patterned by combining EBL and

piranha solution wet etch (Methods). Adopting further ICP-RIE patterning with reduced device footprint can further enhance performance of the vdW integrated III-V-SiN photodetectors. The presence of air gap $h$ primarily affects the coupling length between the III-V nanomembrane and the SiN waveguide underneath. Numerical simulations indicate that over 99.9% of the input light power can be absorbed by the III-V layer after a 40 μm propagation length with air gap $h = 30$ nm (Fig. S32a). Similar photoresponsivity is observed for GaAs-SiN photodetectors with similar device size but different air gap heights (as main text Fig. 3f). Buried electrodes are applied to eliminate air gap to $h = 0$ nm (Figs. S32b, S32c). Despite stronger photoresponsivity expected from GaN nanomembranes at shorter ultraviolet (UV) wavelengths such as 365 nm, the largely increasing optical loss from our lab-made SiN waveguide chips prohibits on-chip photodetector measurements at shorter wavelengths. For the photoresponsivity measurements for GaN-based integrated detectors, calibrations on delivered optical power intensity to the GaN-photodetectors were performed. Bare SiN chips (without GaN vdW integration) of identical patterns are measured first. Then the optical power reached to the GaN-photodetectors are estimated by considering the output laser source power after fiber lens, chip edge coupling loss, and waveguide propagation loss (over 25 dB/cm at $\lambda = 405$ nm wavelength). This calibration was found necessary due to the increasing SiN chip loss at short light wavelengths. Appreciable and negligible photoresponsivity were, respectively, observed for the GaAs- (Fig. S33e) and GaN-based photodetectors (Fig. S33f) at $\lambda = 520$ nm, as this small photon energy far below the GaN bandgap cannot enable efficacious GaN sideband photodetection[11,118].

In contrast, for GaAs-based photodetectors only edge coupling loss was considered, given the acceptable optical loss at longer wavelengths (around 1.5 dB/cm at $\lambda = 780$ nm wavelength for our lab-made chips). To facilitate further advanced waveguide-integrated UV photodetectors, additional attentions on optimizing SiN photonic chips fabrication or adopting foundry-based chips are required[51] for future works. For the measurement of current-voltage ($I$-$V$) curves and photoresponsivity (Methods), only one pair of bottom contact (BC1) and top contact (TC1), or combo (BC2 and TC2) were probed at the same time.

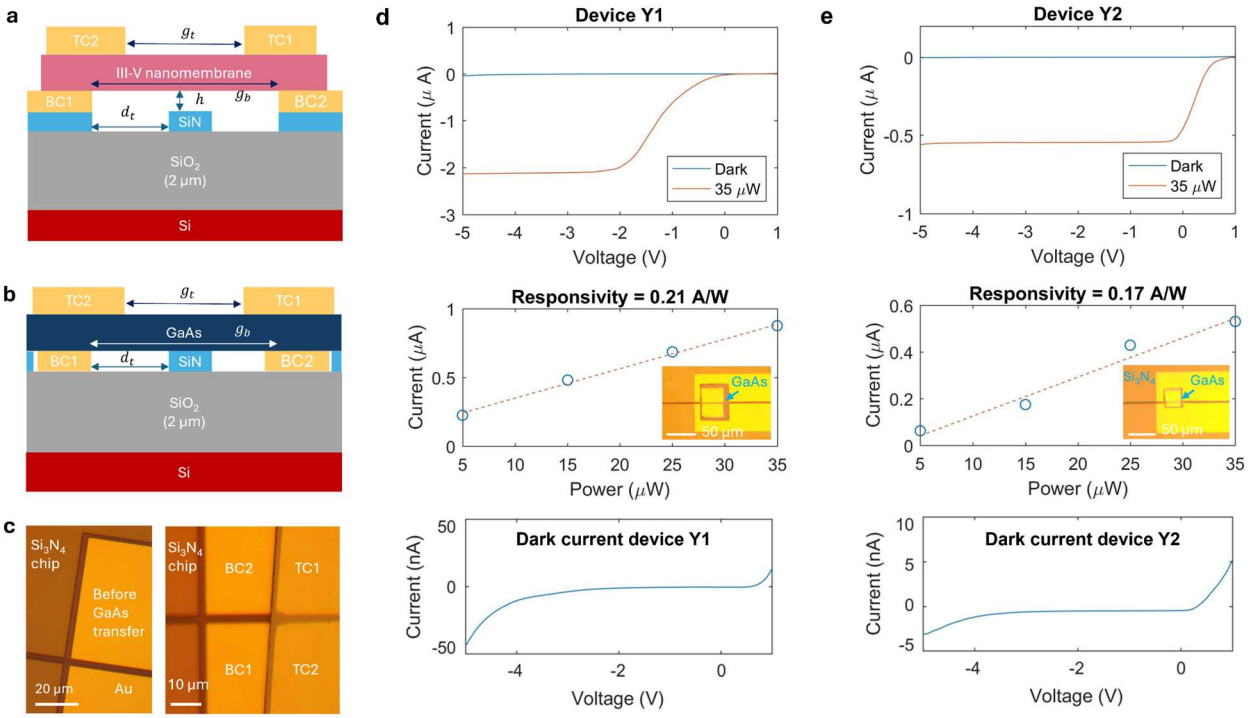


Figure S32. (a) and (b) Device structure schematics for the vdW-integrated III-V nanomembrane photo-detectors with (a) and without (b) air gap $h$. (c) Optical micrographs of GaAs photodetector without air gap. (d) and (e) $I$-$V$ curves for two GaAs-vdW integrated photodetectors Y1 and Y2, respectively, with different reduced device sizes (shown as inset micrographs of middle panels). BC: bottom contact. TC: top contact.

Device dark currents are separately measured in an enclosed probe station (C-6 Probe Station, Everbeing Int'l Corp.) equipped with semiconductor device parameter analyzer (Keysight B1500A. The other $I$-$V$ data are measured in the chip end-coupling setup fed with different laser sources (Methods, Fig. S33). The dark current for the GaN-SiN photodetector shown in main text Fig. 3m is 45.6 nA at 5V bias voltage. At -2 V bias voltage, the dark currents are 16.4 nA and 19.8 nA for the GaAs-SiN photodetectors shown in main text Fig. 3f left and 3f right panels, respectively. The photocurrent values are also largely related to the effective device sizes (under the case of sufficient light absorption from the underlying SiN waveguides). By further reducing the size of the electrode contacts and the patterned GaAs nanomembranes (Methods), much smaller dark currents are measured in smaller-sized photodetectors (with air gap $h$~30 nm): 1.2 nA and 0.54 nA for devices shown in Figs. S32d and S32e, respectively (at -2 V bias voltage), with slightly reduced photoresponsivity (with sufficient device length for light absorption).

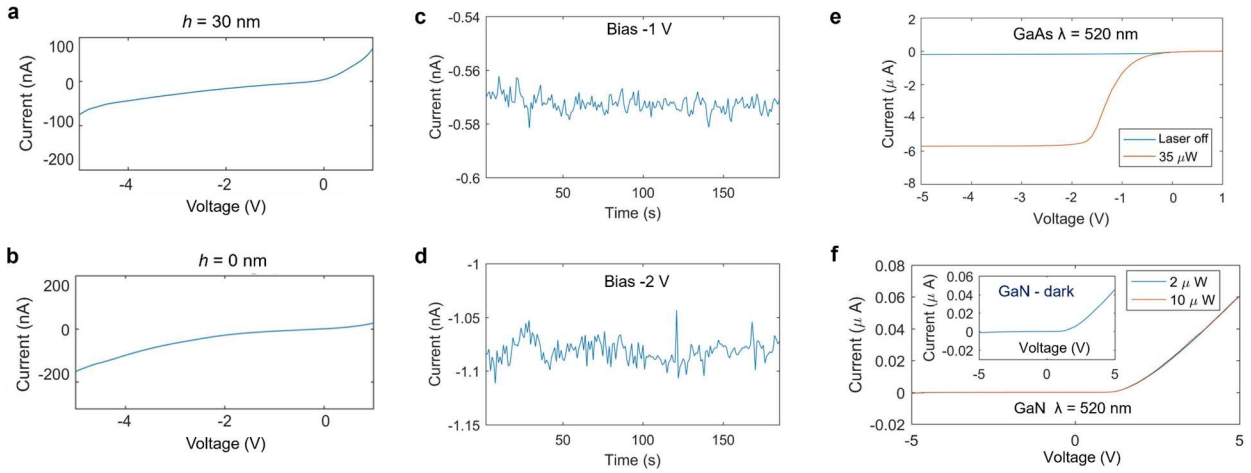


Figure S33. (a) and (b) Dark current $I$-$V$ curves for the devices shown in main text Fig. 3f left, and right panels, respectively. (c) and (d) $I$-$T$ (dark current-time) curves for device Y1 at -1 V and -2 V bias voltage, respectively. (e) Device $I$-$V$ curves for the GaAs-based photodetector (with $h = 0$ nm) measured at $\lambda =$ 520 nm. (f) Device $I$-$V$ curves for the GaN film-vdW integrated SiN waveguide photodetector (shown in main text Fig. 3j) measured at $\lambda = 520$ nm. Inset panel: measured GaN-device dark current via probe station setup.

## S19. Benchmarks for waveguide-coupled III-V photodetectors

By lateral stitching of GaAs and GaN freestanding single-crystalline nanomembranes atop the same SiN photonic chip, extended wide-spectrum photodetection can be enabled. The benchmarks for waveguide-coupled on-chip photodetectors based on group III-V (including III-N) semiconductors supporting the scattering plot shown in Fig. 5d (in main text) are shown in Table S2. Waveguide-coupled structures are mainly focused here (some free-space photodetectors for comparison are also marked out in the Table).

Table S2 – Benchmarks of waveguide-integrated III-V photodetectors.

| Materials | Waveguide-based? | Wavelength (nm) | Responsivity (A/W) | Integration approach notes | Ref. |
|---|---|---|---|---|---|
| InGaAs | Yes (Si) | 1320 | 0.2 | (Growth) Monolithic selective epitaxy on SOI chip. | [119] |
| InGaAs | Yes (SiN) | 1064 | 0.31 | (Transfer) Heterogeneous low-temperature die bonding to SiN chip. | [120] |
| InGaAs | Yes (SiN) | 1550 | 0.3 | (Transfer) Heterogeneous bonding to SiN chip. | [121] |
| InGaAs | Yes (LN) | 1550 | 0.4 | (Transfer) Heterogeneous III-V bonding onto LNOI chips. | [122] |
| InGaAs | Yes (Si) | 1550 | 0.17 | (Growth) Direct epitaxial III-V growth on Si. | [123] |

| | | | | | |
|---|---|---|---|---|---|
| InP | Yes (Si) | 1575 | 0.45 | (Transfer) Heterogeneous bonding of InP membrane to Si photonics. | [124] |
| GaAs | Yes (SiN) | 850 | 0.11 | (Transfer) Micro-transfer printing of GaAs. | [125] |
| GaAs | Yes (GaAs) | 800 | 0.052 | (Growth) Monolithic epitaxial GaAs/AlGaAs. | [126] |
| GaAs | Yes (PI) | 850 | 0.4 | (Growth) Epitaxial GaAs combined with polyimide (PI) waveguide. | [127] |
| GaAs | Yes ($Ta_2O_5$) | 635 | 0.3 | (Transfer) Adhesive die-to-wafer bonding onto $Ta_2O_5$ waveguides. | [128] |
| | | 780 | 0.36 | | |
| GaAs | No | 620 | 0.04 | (Transfer) ELO GaAs and bonding to form integrated photodetectors. | [129] |
| AlGaAs | No | 440 | 0.137 | (Growth) Epitaxial free-space device on GaAs substrate. | [130] |
| | | 540 | 0.19 | | |
| GaN | No | 370 | 0.14 | (Growth) Monolithic epitaxial GaN photodetector. | [131] |
| GaN | No | 240 | 0.005 | (Growth) Monolithic epitaxial GaN photodetector. | [132] |
| AlGaN | No | 305 | 0.004 | (Growth) Monolithic epitaxial AlGaN photodetector. | [133] |
| GaAs | Yes (SiN) (This work) | 780 | 0.30 | (Transfer) Lateral stitching of vdW-integrated single-crystalline GaAs and GaN nanomembranes on SiN photonic chip. | \ |
| | | 520 | 0.16 | | |
| GaN | | 405 | 0.017 | | |

Note: The primary photodetection material is marked out. For waveguide-coupled photodetectors, the waveguide materials are manifested, such as: Yes (SiN). Silicon nitride ($Si_3N_4$): SiN. Epitaxial lift-off (ELO). For integration approach, if the operating III-V (or III-N) semiconductors are directly grown on the photonic structures or substrates, it is classified as 'Growth'-based approach. Otherwise, it is denoted as 'Transfer'-based approach.

## S20. Device details for CFO/BTO hybrid microring

For the CFO-SOI microring-based on-chip optical isolators shown in main text Fig. 4c, an 80 nm-thick $SiO_2$ is deposited via PECVD on prefabricated SOI chip to engineer the desired spatial modal overlap between CFO layer and the operating transverse magnetic (TM) mode[86]. The CFO films were latter patterned via combined EBL and wet etching processes (Methods). For the multifunctional EO and magneto-optical (MO) modulation devices shown in Fig. 4g (main text), PECVD $SiO_2$ (~ 80 nm-thick) was also applied to BTO nanomembrane-transferred SOI photonic chip. To ensure the high uniformity and yield of BTO vdW integration[25], buried electrodes structures (Fig. S16b) are applied.

Compared with other metallic ferromagnets, such as the permalloys of Fe, Co, Ni, etc., CFO is an insulator oxide with comparatively much lower optical absorptions and microwave loss, as well as much higher chemical and thermal stability[134-136]. The optical loss for CFO-covered waveguides is estimated by comparing the quality (Q) factors of the microrings of identical structure after CFO vdW-integration. For a radius $R = 50$ μm microring with experimentally measured free-spectrum range FSR ≈ 1.82 nm, the group index can be calculated as $n_g = \lambda^2/(\mathrm{FSR} \cdot 2\pi R) \approx 4.23$, for 1.555 μm light wavelength $\lambda$. Near critical coupling, we have the intrinsic $Q_{\mathrm{int}} \approx 2Q_{\mathrm{load}}$, where the loaded Q factor can be estimated as $Q_{\mathrm{load}} = \lambda/\Delta\lambda_{\mathrm{FWHM}}$. Applying the measured full-width half-maximum (FWHM) linewidth $\Delta\lambda_{\mathrm{FWHM}}$ (based on not normalized transmission curves) around 37 pm, the estimated MO waveguide loss is $\alpha_{\mathrm{avg}} = 2\pi n_g/(Q_{\mathrm{int}}\lambda) \approx 9$ dB/cm. Given the modal overlap factor Γ ≈ 3.98 %, and the CFO cover ratio $\tau = L_{\mathrm{CFO}}/(2\pi R) \approx 8\%$, where $L_{\mathrm{CFO}}$ is the CFO-covered length, we have the estimated CFO material loss $\alpha_{\mathrm{CFO}} = \alpha_{\mathrm{avg}}/(\Gamma\tau) \approx 2900$ dB/cm. For the CFO/BTO hybrid microring shown in Fig. 4g (main text), taking updated $L_{\mathrm{CFO}} = 160$ μm, Γ ≈ 1.21%, FSR ≈ 0.31 nm, $\Delta\lambda_{\mathrm{FWHM}} \approx 24$ pm, the estimated CFO loss $\alpha_{\mathrm{CFO}}$ is around 5400 dB/cm. Based on the material and device characterization results from previous literature[137-139], the optical scattering from the defects and morphology uniformity of the CFO nanomembranes is a crucial factor contributing to total optical loss of the MO materials.

## S21. Magnet-free CFO optical isolators

Distinctive from ferrimagnetic garnets such as YIG[56,86], CFO is a hard ferrimagnetic material with strong coercivity, where the magnetic field can persist even after the retrieval of external magnets[137,139]. Therefore, magnet-less on-chip optical isolation can be realized by CFO nanomembranes. Besides the conventional nonreciprocal optical applications with external permanent magnets shown in Fig. 4 (main text), the vdW-integrated CFO nanomembranes permits optical isolation without external magnets after CFO magnetization, functioning identically as the combo of hard magnets (e.g. CoFeB) and soft MO materials (e.g. Ce:YIG)[56].

Figure S34a shows the normalized optical transmission of the CFO-integrated SOI microring after removing the permanent magnet for 30 minutes. The single-crystallinity film quality enables stronger magnetic responses than those based on poly-crystal CFO films[137,139,140], persisting after magnets retrieval (Fig. S34b, can be enhanced in time duration). The fabricated devices were magnetized at room temperature by a neodymium magnet overnight with ~300 mT magnetic field intensity limited by experimental setup. Current setup limits the sufficient magnetization of the CFO nanomembranes vdW-integrated to the SOI chips (Fig. S34), which can be further enhanced by applying stronger magnets and engineered sample heating and cooling procedures during magnetization[86,136,141] for compact optical isolators.

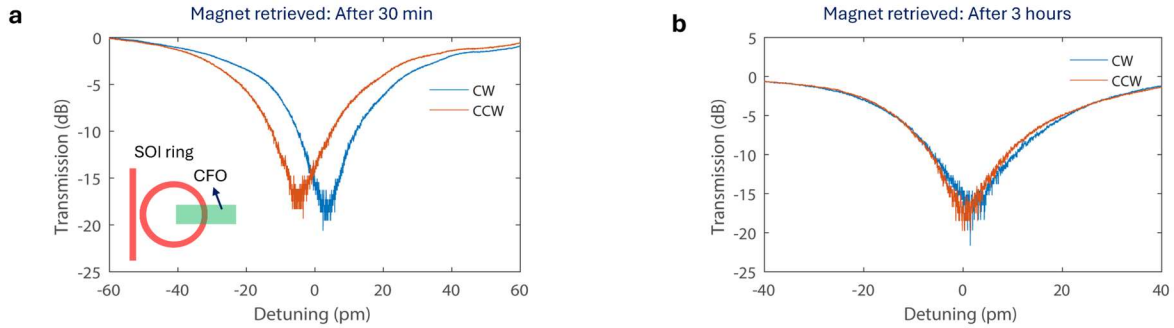


Figure S34. Normalized optical transmission between clockwise (CW) and counterclockwise (CCW) light after retrieving external permanent magnet for (a) 30 min, and (b) 3 hours.

## S22. Faraday rotation coefficient estimation details

Through magneto-optical (MO) effect, time reversal symmetry can be broken to facilitate optical isolators and circulators[86]. The dielectric matrix $\epsilon$ of the MO material is no longer symmetric[142]

$$\epsilon = \begin{bmatrix} \epsilon_{xx} & 0 & i\epsilon_{xz} \\ 0 & \epsilon_{yy} & 0 \\ -i\epsilon_{xz} & 0 & \epsilon_{zz} \end{bmatrix}, \tag{S22-1}$$

where the non-zero off-diagonal component $\epsilon_{xz} \approx n\lambda\theta_F/\pi$ is related to the Faraday rotation $\theta_F$ as a consequence of Zeeman splitting, with $n$ as refractive index and $\lambda$ as light wavelength[86,142,143].

For a resonant microring resonator $m\lambda = n_{\text{eff}} \cdot L$, where $L$ is the ring perimeter and $m$ is an integer, in small effective-index perturbation, $\Delta n_{\text{eff}}$ shifts the resonance by $\Delta\lambda = \lambda\Delta n_{\text{eff}}/n_{\text{g}}$, with $n_{\text{g}}$ as the group index. The difference in effective index between CW and CCW light[86] can be given below.

$$2\lambda_{\text{MO}} = \Delta\lambda = \lambda\frac{\Delta n_{\text{eff}}}{n_{\text{g}}} \tag{S22-2}$$

Given the experimentally measured free spectrum range as FSR = 1.82 nm for the approximate $R = 50$ μm radius SOI micro-ring ($L = 2\pi R$), the group index is calculated as $n_{\text{g}} = \frac{\lambda^2}{\text{FSR}\cdot L} \approx 4.23$ for $\text{TM}_0$ mode

around $\lambda = 1555$ nm. With the experimentally measured $\Delta\lambda = 36$ pm, the non-reciprocal phase shift (NRPS)[144] is calculated as $\Delta\Phi_{\mathrm{NRPS}} = 2\pi\frac{\Delta\lambda}{\mathrm{FSR}} = 0.124$ rad. We have

$$\Delta\Phi_{\mathrm{NRPS}} = (\beta_{\mathrm{CW}} - \beta_{\mathrm{CCW}})L_{\mathrm{MO}} = 2\Delta\beta L_{\mathrm{MO}} = 2\theta_{\mathrm{F}}L_{\mathrm{MO}}, \quad \text{(S22-3)}$$

where $\beta$ is $TM_0$ mode propagation constant, $L_{\mathrm{MO}}$ is the length of the magneto-optical (MO) material CFO, and $\theta_{\mathrm{F}}$ is the Faraday rotation coefficient.

Therefore, for $L_{\mathrm{MO}} \approx 26.5$ μm, the mode-effective Faraday rotation coefficient ${\theta_{\mathrm{F}}}^{\mathrm{eff}} = \frac{\Delta\Phi_{\mathrm{NRPS}}}{2L_{\mathrm{MO}}} \approx 2344$ rad/m. To derive the intrinsic CFO film Faraday rotation coefficient ${\theta_{\mathrm{F}}}^{\mathrm{film}}$, the modal overlap factor Γ between the $TM_0$ mode and the ~80 nm-thick CFO (with ~60 nm $SiO_2$ buffer in between) is numerically calculated via FEM method $\Gamma = \frac{\int_{\mathrm{MO}} \frac{1}{2}\Re(\mathbf{E}\times\mathbf{H}^*)\cdot\hat{\mathbf{x}}\,dS}{\int_{\mathrm{All}} \frac{1}{2}\Re(\mathbf{E}\times\mathbf{H}^*)\cdot\hat{\mathbf{x}}\,dS} \approx 3.98\%$. We have ${\theta_{\mathrm{F}}}^{\mathrm{film}} = {\theta_{\mathrm{F}}}^{\mathrm{eff}}/\Gamma \approx 33800°$/cm.

For the CFO/BTO hybrid microring, the device structure parameters: Si waveguide dimension: 750 nm × 220 nm, BTO thickness: 60 nm, $SiO_2$ thickness: 80 nm, CFO thickness: 40 nm. Given the FSR ~ 0.31 nm for the racetrack microring resonator, the experimentally measured CW and CCW wavelength split $\Delta\lambda$ ~ 10.1 pm, and CFO length $L_{\mathrm{MO}}$ ~ 160 μm, NRPS is calculated as $\Delta\Phi_{\mathrm{NRPS}} = 2\pi\frac{\Delta\lambda}{\mathrm{FSR}} \approx 0.204$ rad. Mode effective Faraday rotation yields ${\theta_{\mathrm{F}}}^{\mathrm{eff}} = \frac{\Delta\Phi_{\mathrm{NRPS}}}{2L_{\mathrm{MO}}} \approx 640$ rad/m. Given the numerically simulated field overlap $\Gamma \sim 1.21\%$, the intrinsic CFO film Faraday rotation coefficient for this device is estimated as ${\theta_{\mathrm{F}}}^{\mathrm{film}} = {\theta_{\mathrm{F}}}^{\mathrm{eff}}/\Gamma \approx 30100°$/cm.

## S23. Ferromagnetic loop measurements

The magnetic properties of grown CFO and YIG nanomembranes were evaluated at room temperature using vibrating sample magnetometer (VSM 7410 Series, Lake Shore). For instance, the as-grown CFO/MgO sample and bare MgO substrate of identical size were measured first. The CFO ferromagnetic loop was then obtained by subtracting the substrate response from as grown samples (Fig. S35a, Methods)[145,146]. The measured Ce: YIG magnetic hysteresis is shown as Fig. S35b.

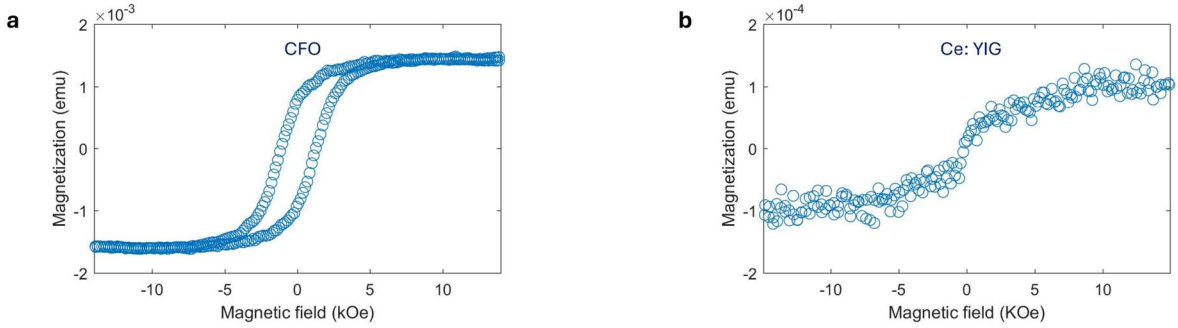


Figure S35. (a) Representative measured magnetic loop data of the CFO/MgO sample (10 × 10 mm) after substrate background subtraction. (b) Measured magnetic loop of the thick Ce: YIG film.

## S24. Benchmarks of MO material CFO

The benchmark details for different MO materials are shown in Fig. S36 and Table S3. CFO exhibits giant Faraday rotation coefficients and magnet-less operation capability compared to other magnetic materials. Device performance parameters, such as the non-reciprocal phase shift (NRPS), effective length of the

magneto-optical (MO) waveguide $L_{MO}$, and propagation loss of the MO waveguides $\alpha_{wg}$ are benchmarked as well in Table S3. Thanks to the giant CFO Faraday rotation coefficient, a big NRPS can be realized in an ultracompact length $L_{MO}$ of about 26 μm. The optimal single-crystalline nanomembrane quality also enhances magnetic response and reduces optical losses from defects scattering and imperfect CFO crystal quality found in previous works[21,137,139], circumventing the prior obstacles of lattice mismatching for defective heteroepitaxial CFO layer by applying photonic vdW integration[25].

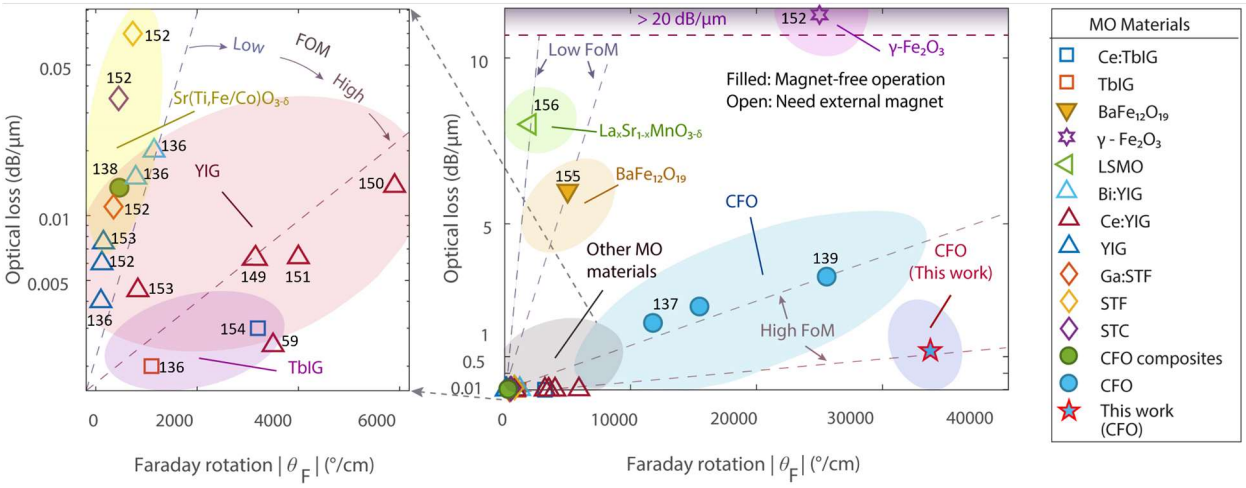


Figure S36. Benchmark details on the key parameters of different MO materials. Detailed symbol explanations are made below Table S3. Corresponding reference numbers are marked out near the points.

Table S3 – Benchmarks of reported MO materials and devices.

| MO Material | $\theta_F$ (°/cm) | Material loss $\alpha_m$ (dB/cm) | Propag. loss $\alpha_{wg}$ (dB/cm) | Operation λ (nm) | FOM (°/dB) | NRPS (rad/ mm) | MO WG length $L_{MO}$ (mm) | Notes on material preparations | Ref |
|---|---|---|---|---|---|---|---|---|---|
| Ce:YIG | -1500 | — | — | 1550 | — | 1.9* | 0.85* | Sputtered Ce: YIG film on Si with YIG buffer. | 147 |
| Ce:YIG | -3000 | — | 31.9 | ~1550 | — | 0.55* | 5.6* | Wafer bonding of Ce:YIG film to SOI microring. | 148 |
| Ce:YIG | -3200 | 60* | 6.3* | 1550 | 53 | 0.79* | 2* | Wafer bonding of Ce:YIG film to SOI. | 149 |
| Ce:YIG | −5900 | 137* | 31.7 | 1550–1570 | 43 | 1.57* | 1* | PLD Ce: YIG on SiN with YIG buffer layer. | 150 |
| Ce:YIG | -4000 | — | 14.5 | 1550 | — | 0.98* | 0.92* | Wafer bonding of Ce: YIG dies. | 151 |
| Ce:YIG | -830 | 45 | — | 1550 | 21 | — | — | Poly-crystal YIG growth. | 152 |
| Ce:YIG | −1263 | — | — | 1540–1550 | — | 0.63* | 0.2* | PLD poly-crystal Ce: YIG on Si. | 153 |
| Ce:YIG | -3500 | — | 13 | 1550 | — | 0.5* | 0.22* | Wafer bonding of Ce: YIG/GGG to Si photonics. | 59 |
| YIG | 100 | 50* | — | 1550 | 2 | — | — | Direct grown poly-crystal YIG. | 152 |
| YIG | 120 | 60* | — | 1550 | 2 | — | — | RF sputtered poly-crystal YIG. | 136 |
| Bi:YIG | −1200 | 200 | 50* | 1550 | 6 | — | — | RF sputtered poly-crystal Bi: YIG on Si. | 136 |
| Bi:YIG | -838 | 150 | — | 1550 | 5.6 | — | — | liquid phase epitaxy on GGG. | 136 |
| Ce:TbIG | −3200 | — | 15* | 1550 | — | — | — | Sputtered Ce:TbIG on Si. | 154 |
| TbIG | -1100 | — | 20* | 1550 | — | — | — | Sputtered Ce:TbIG. | 136 |
| CAFO | 12000 | 8300 | 3700 | ~1550 | 1.5 | — | — | RF sputtered CAFO with different buffer layers. | 140 |
| CFO NPs | 310 | 130* | — | 820, 1550 | 2.4 | — | — | CFO nanoparticle composites. | 138 |
| CFO | 25600 | 34000 | — | 1550 | 0.8 | — | — | Sputtered CFO on Si. | 139 |
| CFO | 15500 | — | 210 | 1545–1550 | — | 3.6* | 0.04* | Sputtered CFO on Si. | 137 |

| | | | | | | | | | |
|---|---|---|---|---|---|---|---|---|---|
| $BaFe_{12}O_{19}$ | 5000* | 60000* | — | ~1550 | 0.08 | — | — | PLD growth. Magnet-less operation. | 155 |
| $\gamma$-$Fe_2O_3$ | 25000 | 350000* | — | 1550 | 0.07 | — | — | — | 152 |
| LSMO | 2000 | 80000* | — | 460, ~1550 | 0.025 | — | — | Ion-plasma evaporation on STO substrates. | 156 |
| Ga:STF | -400 | 110* | — | 1550 | 3.6 | — | — | — | 152 |
| STC | -500 | 350* | — | 1550 | 1.4 | — | — | — | 152 |
| STF | -780 | 700* | — | 1550 | 1.1 | — | — | — | 152 |
| This work (CFO) | 33800 | 5400* | 9* | 1550 | 6 | 4.68 | 0.026 | vdW integration of single-crystalline CFO film. Magnet-less optical isolation. | \ |

Notes: $\theta_F$: Faraday rotation coefficient. $\alpha_m$: material absorption loss. $\alpha_{wg}$: the estimated device propagation loss for the magneto-optical (MO) waveguide, which is highly dependent on MO waveguide device structure. λ: Light wavelength. FOM: figure of merit, defined as $|\theta_F|/\alpha_m$. NRPS: non-reciprocal phase shift (based on calculation estimation). $L_{MO}$: length of the MO material-integrated waveguide (WG). YIG: yttrium iron garnet ($Y_3Fe_5O_{12}$), TbIG: terbium iron garnet ($Tb_3Fe_5O_{12}$), CFO: cobalt ferrite ($CoFe_2O_4$), CAFO: aluminum-substituted cobalt ferrite ($CoAl_xFe_{2-x}O_4$), GGG: gadolinium gallium garnet ($Gd_3Ga_5O_{12}$), STO: strontium titanate ($SrTiO_3$). NPs: nanoparticles, LSMO: lanthanum strontium manganite ($La_{0.7}Sr_{0.3}MnO_{3-\delta}$), STF: strontium titanate-ferrite oxide ($Sr(Ti,Fe)O_{3-\delta}$), STC: strontium titanium cobalt oxide ($Sr(Ti,Co)O_{3-\delta}$), Estimated Faraday rotation values are marked with * superscript. Not reported values are marked by — symbol. Approximate operation wavelengths are marked with ~ symbol. Most directly grown MO films are polycrystalline.

## S25. Fully integrated MO devices prospects

In the proof-of-concept demonstrations shown in Fig. 4 (main text), permanent magnets are applied to verify the non-reciprocal optical transmissions. Nevertheless, the bulk external magnets do not fit integrated photonic applications. To facilitate fully chip-integrated MO devices, electromagnets via metal coil structures can be applied[56,59] (Fig. S37a), where the vdW-integrated CFO nanomembrane can be optionally patterned for desired spatial modal overlap (Methods). Through injecting electrical current (as white arrows in Fig. S37a), magnetic fields can be locally induced around the microring waveguide (Fig. S37b) operating at transverse magnetic (TM) optical mode (Fig. S37c). The metal electromagnet design was not applied in current work limited by experimental setup, because in this case precise temperature control is needed to exclude the current-induced thermal tuning effect on the microring resonators. Current external magnet fully confirmed the feasibility of CFO-based MO applications excluding any thermal-related tuning effects. Nevertheless, fully integrated MO nonreciprocal devices can be envisaged in future work. The multifunctional electromagnetically reconfigurable microring demonstrated in this work can be further modified in device structure and design to enable magnetically mode conversion, polarization rotation, and non-reciprocal EO modulations for lasers[27,157], amplifiers[53], and in-memory computing[56,158] tasks. For freestanding YIG films, only its film growth, crystal quality characterizations, layer lift-off, and transfer are studied in this work (detailed in Supplementary Note S5). Device implementation of freestanding YIG nanomembranes is not carried out here due to not fully optimized YIG film patterning.

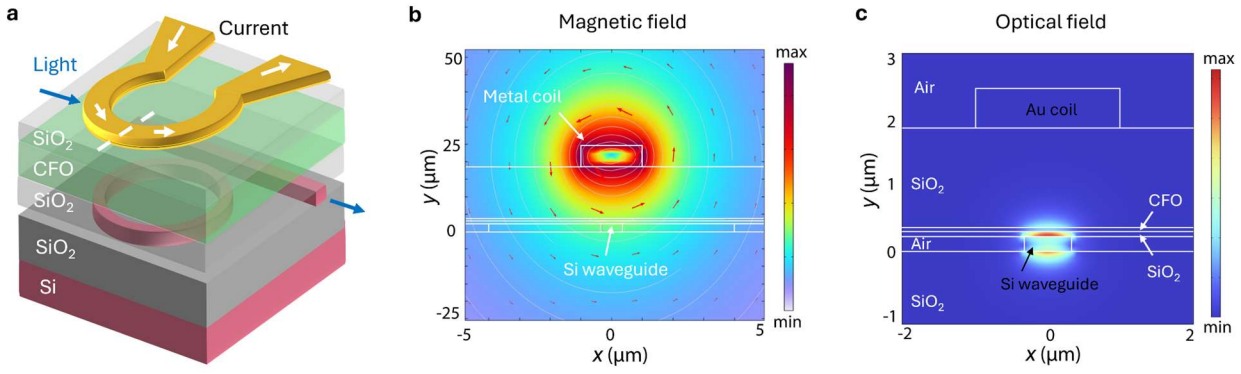


Figure S37. (a) Structure schematics of fully integrated CFO-SOI nonreciprocal microring with electromagnet. Light propagation directions are marked in blue arrows. (b) and (c) Simulated cross-

sectional magnetic field (b) and fundamental TM mode optical field (c) distributions of the microring waveguide.

## S26. Wafer-scale BTO nanomembrane vdW integration

Photonic vdW integration of functional freestanding nanomembranes[2,25] can be performed at varying scales from millimeter-sized film (main text Fig. 1e) to wafer-scale (Fig. S38a). After soft hotplate baking (~100 °C) and cleaning processes (Methods), smooth surface morphologies were confirmed by AFM at 16 representative areas for the transferred 1-inch-diameter BTO film with a spacing around 5 mm between different measurement areas (Fig. S38b). An average root mean square (RMS) roughness below 1 nm was experimentally confirmed, which can be further reduced by applying chemical mechanical planarization (CMP) polishing[35]. Cross-sectional HAADF STEM images confirm the atomically clean and electronically sharp interface between the vdW-integrated single-crystalline BTO layer and the oxide substrate (Fig. S38c) with high robustness (Supplementary Note S27). Corresponding EDS STEM composition maps are shown in Fig. S38d.

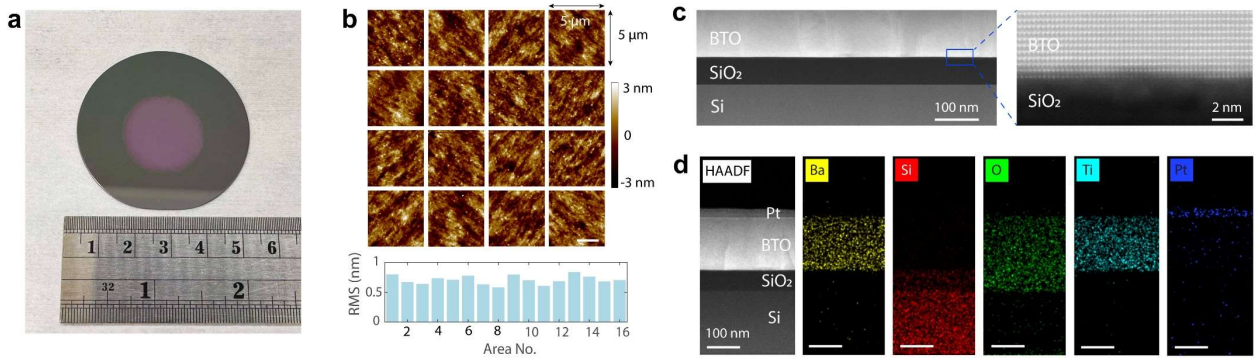


Figure S38. (a) Photograph of 1-inch diameter BTO vdW integrated onto $SiO_2$ substrate. (b) AFM images from 16 representative areas over the transferred BTO film, with measured RMS roughness shown below. (c) and (d) Cross-sectional HAADF STEM image (c) and EDS maps of vdW-integrated single-crystalline BTO nanomembrane.

The layer transfer processes of wafer-scale nanomembranes are similar (Methods), while additional layer lift-off time and attention in layer handling are needed for large-sized samples[11]. For example, polymer handers such as PPC or PMMA can be applied. Despite trivial details, the sample edge needs to be exposed to the etchant, otherwise the polymer-encapsulated sacrificial layer will largely increase layer lift-off time (Fig. S39a). Supporting layers such as thermal release tape (TRT) are also found necessary for large-scale nanomembrane lift-off. Otherwise, the heavy wafer substrate tends to get detached from the film stacks and sank down into the etchant before the full completion of sacrificial layer etching, leading to compromised film lift-off yield. Shallow etchant or bottom supporting pieces (second left panel in Fig. S39b) can address this issue. After nanomembrane vdW integration, overnight drying and subsequent thermal treatments (Supplementary Note S27) were applied to enhance layer bonding to the substrate. Compared to TRT-based transfer, where wrinkles are more easily generated during the thermal release and cooling process with layer thermal deformation, mixed PPC- or PMMA-handlers-based layer transfer with engineered polymer Young's modulus[8] can yield better vdW-integration uniformity of the freestanding films (Fig. S39b). Despite that practical details and tentative handlings are needed here to facilitate ideal vdW integration of functional nanomembranes[25], the proof-of-concept demonstrations here primarily aim to verify the feasibility of large wafer-scale vdW integration perspectives. Automatic transfer[159,160] or bonding tools[161] can be applied in future for larger scale manufacturing. Compared with conventional wafer bonding

(discussed in Fig. S12a), the proposed 2DLT and ELO schemes features fast layer release speed (almost instant for 2DLT[1,3] and around 10 min for a 1 × 1 cm BTO[2]) without necessitating sophisticated substrate grinding or CMP procedures[25], precise film thickness control, and reduced film manufacture cost by substrates recycling[9,11] (Fig. S40).

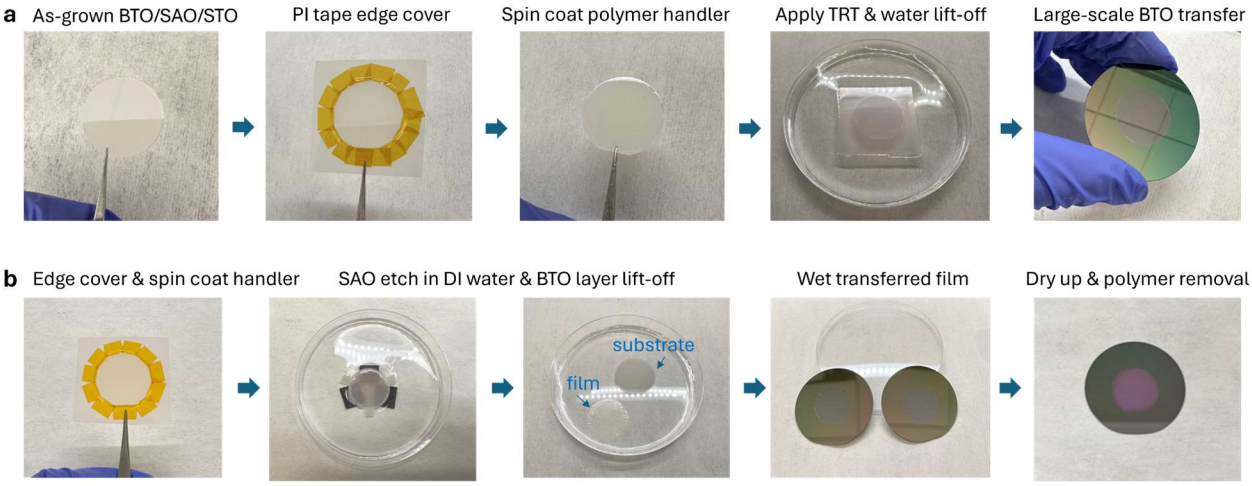


Figure S39. (a) and (b) Layer lift-off and transfer process of BTO nanomembranes via TRT (a) and PPC polymer (b) handlers respectively.

## S27. Robustness of photonic vdW integration

After nanomembranes transfer and fully dry up in wet transfer, the samples are put under soft hotplate baking (80~150 °C depending on samples) for overnight to a day (Methods) to enhance nanomembranes adhesion before removing polymer handlers. After proper thermal treatment, very robust nanomembranes bonding to the substrate were experimentally verified. Mild ultrasonic for minutes will not delaminate the transferred films. Nevertheless, for prefabricated photonic substrates with varying structures, such as the bottom electrodes (Supplementary Notes S9), the film attachments are found comparatively weaker than full-dielectric or bare substrates. Highly reliable photonic vdW integration are found feasible for arbitrary substrates, as long as the substrates are in general flat and smooth[162] without big and dense height steps variations (Supplementary Notes S1, S20). As evidenced by Figs. 2i, 3a, 4f (main text) and supplementary Figs. S7, S22, S38, the narrow vdW gaps observed before[8] between layers can vanish after applying soft baking procedures, where solid bonding is experimentally confirmed instead, mediated by the abundant dangling bonds-decorated 3D nanomembrane surfaces[1,2,25]. Currently all nanomembrane transfers are made at ambient pressure in lab, further professional bonding tools with vacuum and heating in cleanroom can further enhance the outcomes. Defects such as wrinkles and cracks may be occasionally induced during the vdW integration process of 3D nanomembranes, leading to additional losses near the defective regions. Despite current initial proof-of-concept demonstrations via human hands, the process-optimized vdW-integrated 3D nanomembranes and devices in this work exhibit high hetero-integration uniformity and robustness (detailed in Supplementary Note S1), which can be further improved by employing professional film transfer setups[60,78,160,163,164].

This work can serve as a comprehensive baseline on leveraging the versatile vdW integration platform for realizing various heterogeneous integrated photonic applications, with diverse functional freestanding 3D nanomembranes, covering thin film epitaxy, lift off, and device implementations with verified unique advantages. Both the single-crystalline film quality (with well-defined crystallographic orientations) and its freestanding form with artificially laminated vdW interfaces are the two keys for enabling boundless and

high-performance photonic heterogeneous integrations reported in this work. We thus highlight the critical role of creating and integrating these freestanding 3D single-crystalline films in photonics, which were not clearly elucidated with careful attention in conventional hetero-integration strategies such as direct heteroepitaxy or wafer bonding. New opportunities await in further leveraging the versatile photonic vdW integration platform to develop 3D photonic integration[44] with ultracompact footprint and unparalleled multifunctionality[1,45,165,166]. An intriguing playground thus unfolds to coalesce various functional optical layers with optimal single-crystallinity but distinct crystal structures that are hardly accessible via direct heteroepitaxial approaches, permitting emerging opportunities for heterogeneous photonic integration[1,2,15,25] and nanomembranes-related physics and technologies[7,18,19,46-49,167-169].

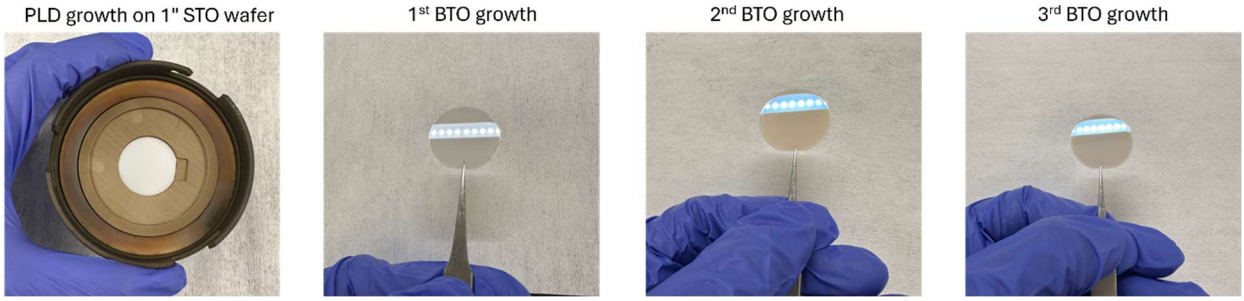


Figure S40. Manufacture cost reduction through recycling of costly substrates in the heterogeneous integration of functional nanomembranes. Repeated acetone/IPA ultrasonic bath and BOE cleaning were applied to substrate after each time of nanomembranes growth and lift-off.

**Supplementary References**


1 Shin, J. *et al.* Vertical full-colour micro-LEDs via 2D materials-based layer transfer. *Nature* **614**, 81-87 (2023).

2 Kum, H. S. *et al.* Heterogeneous integration of single-crystalline complex-oxide membranes. *Nature* **578**, 75-81 (2020).

3 Kim, H. *et al.* Remote epitaxy. *Nature Reviews Methods Primers* **2**, 1-21 (2022).

4 Chang, C. S. *et al.* Remote epitaxial interaction through graphene. *Science Advances* **9**, eadj5379 (2023).

5 Jia, R. *et al.* Long-distance remote epitaxy. *Nature* **646**, 584-591 (2025).

6 Kum, H. *et al.* Epitaxial growth and layer-transfer techniques for heterogeneous integration of materials for electronic and photonic devices. *Nature Electronics* **2**, 439-450 (2019).

7 Rogers, J. A., Lagally, M. G. & Nuzzo, R. G. Synthesis, assembly and applications of semiconductor nanomembranes. *Nature* **477**, 45-53 (2011).

8 Moon, J.-Y. *et al.* Crack-Free Transfer of Wafer-Scale Freestanding Single-Crystalline Nanomembranes Enabled by Elastically Graded Polymer. *Advanced Materials* **n/a**, e13080 (2025).

9 Kim, Y. *et al.* Remote epitaxy through graphene enables two-dimensional material-based layer transfer. *Nature* **544**, 340-343 (2017).

10 Kong, W. *et al.* Polarity governs atomic interaction through two-dimensional materials. *Nature Materials* **17**, 999-1004 (2018).

11 Kim, H. *et al.* High-throughput manufacturing of epitaxial membranes from a single wafer by 2D materials-based layer transfer process. *Nature Nanotechnology* **18**, 464-470 (2023).

12 Kim, H. *et al.* Graphene nanopattern as a universal epitaxy platform for single-crystal membrane production and defect reduction. *Nature Nanotechnology* **17**, 1054-1059 (2022).

13 Bae, S.-H. *et al.* Graphene-assisted spontaneous relaxation towards dislocation-free heteroepitaxy. *Nature Nanotechnology* **15**, 272-276 (2020).
14 Lee, S. *et al.* Route to Enhancing Remote Epitaxy of Perovskite Complex Oxide Thin Films. *ACS Nano* **18**, 31225-31233 (2024).
15 Choi, C. *et al.* Reconfigurable heterogeneous integration using stackable chips with embedded artificial intelligence. *Nature Electronics* **5**, 386-393 (2022).
16 Shim, J. *et al.* Controlled crack propagation for atomic precision handling of wafer-scale two-dimensional materials. *Science* **362**, 665-670 (2018).
17 Kim, H. *et al.* Role of transferred graphene on atomic interaction of GaAs for remote epitaxy. *Journal of Applied Physics* **130**, 174901 (2021).
18 Huang, J.-K. *et al.* High-κ perovskite membranes as insulators for two-dimensional transistors. *Nature* **605**, 262-267 (2022).
19 Zhang, J. *et al.* Super-tetragonal Sr4Al2O7 as a sacrificial layer for high-integrity freestanding oxide membranes. *Science* **383**, 388-394 (2024).
20 Chiabrera, F. M. *et al.* Freestanding Perovskite Oxide Films: Synthesis, Challenges, and Properties. *Annalen der Physik* **534**, 2200084 (2022).
21 Lisfi, A. *et al.* Reorientation of magnetic anisotropy in epitaxial cobalt ferrite thin films. *Physical Review B* **76**, 054405 (2007).
22 Yanagihara, H., Uwabo, K., Minagawa, M., Kita, E. & Hirota, N. Perpendicular magnetic anisotropy in CoFe2O4(001) films epitaxially grown on MgO(001). *Journal of Applied Physics* **109**, 07C122 (2011).
23 Kim, B., Kim, M., Li, B. D., Hool, R. D. & Lee, M. L. Cryogenic GaAs laser power converters. *Solar Energy Materials and Solar Cells* **281**, 113321 (2025).
24 Szymanski, N. J. *et al.* An autonomous laboratory for the accelerated synthesis of novel materials. *Nature* **624**, 86-91 (2023).
25 Meng, Y. *et al.* Photonic van der Waals integration from 2D materials to 3D nanomembranes. *Nature Reviews Materials* **8**, 498–517 (2023).
26 Shekhar, S. *et al.* Roadmapping the next generation of silicon photonics. *Nature Communications* **15**, 751 (2024).
27 Snigirev, V. *et al.* Ultrafast tunable lasers using lithium niobate integrated photonics. *Nature* **615**, 411-417 (2023).
28 Chambers, S. A. *et al.* Molecular beam epitaxial growth and properties of CoFe2O4 on MgO(001). *Journal of Magnetism and Magnetic Materials* **246**, 124-139 (2002).
29 Matsuzaki, K., Takagi, H., Hosono, H. & Susaki, T. Structural study of polar MgO(111) epitaxial thin films grown on SrTiO3 (111). *Physical Review B* **84**, 235448 (2011).
30 Niu, F., Meier, A. L. & Wessels, B. W. Epitaxial growth and strain relaxation of MgO thin films on Si grown by molecular beam epitaxy. *Journal of Vacuum Science & Technology B: Microelectronics and Nanometer Structures Processing, Measurement, and Phenomena* **24**, 2586-2591 (2006).
31 Karvounis, A., Timpu, F., Vogler-Neuling, V. V., Savo, R. & Grange, R. BaTiO3: Barium Titanate Nanostructures and Thin Films for Photonics *Advanced Optical Materials* **8**, 2070094 (2020).
32 Steglich, P. & Kehrein, A. Light propagation in anisotropic materials and electro-optical effects: tutorial on the use of eigenvalue problems, tensors, and symmetries. *J. Opt. Soc. Am. B* **41**, 2191-2210 (2024).
33 Boyd, R. W. in *Nonlinear Optics* 511-523 (Springer, 2008).
34 Abel, S. *et al.* A strong electro-optically active lead-free ferroelectric integrated on silicon. *Nature Communications* **4**, 1671 (2013).
35 Abel, S. *et al.* Large Pockels effect in micro-and nanostructured barium titanate integrated on silicon. *Nature Materials* **18**, 42-47 (2019).
36 Eltes, F. *et al.* An integrated optical modulator operating at cryogenic temperatures. *Nature Materials* **19**, 1164-1168 (2020).

37 Chelladurai, D. *et al.* Barium titanate and lithium niobate permittivity and Pockels coefficients from megahertz to sub-terahertz frequencies. *Nature Materials* **24**, 868-875 (2025).
38 Lee, J. W. *et al.* In-plane quasi-single-domain BaTiO3 via interfacial symmetry engineering. *Nature Communications* **12**, 6784 (2021).
39 Castellanos-Gomez, A. *et al.* Van der Waals heterostructures. *Nature Reviews Methods Primers* **2**, 58 (2022).
40 Geim, A. K. & Grigorieva, I. V. Van der Waals heterostructures. *Nature* **499**, 419-425 (2013).
41 Kaur, P. *et al.* Hybrid and heterogeneous photonic integration. *APL Photonics* **6**, 061102 (2021).
42 Baets, R. & Rahim, A. Heterogeneous integration in silicon photonics: opportunities and challenges: opinion. *Optical Materials Express* **13**, 3439-3444 (2023).
43 Davanco, M. *et al.* Heterogeneous integration for on-chip quantum photonic circuits with single quantum dot devices. *Nature Communications* **8**, 889 (2017).
44 Xiang, C. *et al.* 3D integration enables ultralow-noise isolator-free lasers in silicon photonics. *Nature* **620**, 78-85 (2023).
45 Xiang, C. & Bowers, J. E. Building 3D integrated circuits with electronics and photonics. *Nature Electronics* **7**, 422-424 (2024).
46 Sun, H. *et al.* Ferroelectric topologies in BaTiO3 nanomembranes for light field manipulation. *Nature Nanotechnology* **20**, 881-888 (2025).
47 Yoon, H. *et al.* Freestanding epitaxial SrTiO3 nanomembranes via remote epitaxy using hybrid molecular beam epitaxy. *Science Advances* **8**, eadd5328 (2022).
48 Zhang, X. *et al.* Atomic lift-off of epitaxial membranes for cooling-free infrared detection. *Nature* **641**, 98-105 (2025).
49 Sánchez-Santolino, G. *et al.* A 2D ferroelectric vortex pattern in twisted BaTiO3 freestanding layers. *Nature* **626**, 529-534 (2024).
50 Bae, S.-H. *et al.* Integration of bulk materials with two-dimensional materials for physical coupling and applications. *Nature Materials* **18**, 550-560 (2019).
51 Tran, M. *et al.* Extending the spectrum of fully integrated photonics. *Nature* **610**, 54–60 (2022).
52 De Koninck, Y. *et al.* GaAs nano-ridge laser diodes fully fabricated in a 300-mm CMOS pilot line. *Nature* **637**, 63-69 (2025).
53 Riemensberger, J. *et al.* A photonic integrated continuous-travelling-wave parametric amplifier. *Nature* **612**, 56-61 (2022).
54 Eltes, F. *et al.* A BaTiO3-Based Electro-Optic Pockels Modulator Monolithically Integrated on an Advanced Silicon Photonics Platform. *J. Lightwave Technol.* **37**, 1456-1462 (2019).
55 Kim, B. *et al.* Controlling of lattice strains for crack-free and strong ferroelectric barium titanate films by post-thermal treatment. *Scientific Reports* **12**, 5363 (2022).
56 Pintus, P. *et al.* Integrated non-reciprocal magneto-optics with ultra-high endurance for photonic in-memory computing. *Nature Photonics* **19**, 54-62 (2025).
57 Wang, C. *et al.* Lithium tantalate photonic integrated circuits for volume manufacturing. *Nature* **629**, 784-790 (2024).
58 Zhang, J. *et al.* Ultrabroadband integrated electro-optic frequency comb in lithium tantalate. *Nature* **637**, 1096-1103 (2025).
59 Pintus, P. *et al.* An integrated magneto-optic modulator for cryogenic applications. *Nature Electronics* **5**, 604-610 (2022).
60 Cai, J. *et al.* Heterogeneously integrated lithium tantalate-on-silicon nitride modulators for high-speed communications. *Nature Communications* **17**, 3314 (2026).
61 Thureja, P. *et al.* Spalled Barium Titanate Single Crystal Thin Films for Functional Device Applications. *Nano Letters* **25**, 11089-11096 (2025).
62 Ji, D. *et al.* Freestanding crystalline oxide perovskites down to the monolayer limit. *Nature* **570**, 87-90 (2019).
63 Varshney, S. *et al.* Hybrid Molecular Beam Epitaxy for Single-Crystalline Oxide Membranes with Binary Oxide Sacrificial Layers. *ACS Nano* **18**, 6348-6358 (2024).

64 Narayan, J. & Larson, B. C. Domain epitaxy: A unified paradigm for thin film growth. *Journal of Applied Physics* **93**, 278-285 (2003).
65 Sung, S.-Y., Qi, X. & Stadler, B. J. H. Integrating yttrium iron garnet onto nongarnet substrates with faster deposition rates and high reliability. *Applied Physics Letters* **87**, 121111 (2005).
66 Messner, A. *et al.* Plasmonic Ferroelectric Modulators. *J. Lightwave Technol.* **37**, 281-290 (2019).
67 Hu, Y. *et al.* Integrated electro-optics on thin-film lithium niobate. *Nature Reviews Physics* **7**, 237-254 (2025).
68 Cho, S. *et al.* Strongly enhanced dielectric and energy storage properties in lead-free perovskite titanate thin films by alloying. *Nano Energy* **45**, 398-406 (2018).
69 Surampalli, A. & Reddy, V. R. X-ray reciprocal space mapping study of domain evolution with electrical poling in BaTiO3 single crystal. *AIP Conference Proceedings* **2265**, 030015 (2020).
70 Marpaung, D., Yao, J. & Capmany, J. Integrated microwave photonics. *Nature Photonics* **13**, 80-90 (2019).
71 Wang, C. *et al.* Integrated lithium niobate electro-optic modulators operating at CMOS-compatible voltages. *Nature* **562**, 101-104 (2018).
72 Zhu, D. *et al.* Integrated photonics on thin-film lithium niobate. *Advances in Optics and Photonics* **13**, 242-352 (2021).
73 He, M. *et al.* High-performance hybrid silicon and lithium niobate Mach–Zehnder modulators for 100 Gbit s− 1 and beyond. *Nature Photonics* **13**, 359-364 (2019).
74 Mengxue, T. *et al.* Towards high quality transferred barium titanate ferroelectric hybrid integrated modulator on silicon. *Light: Advanced Manufacturing* **5**, 479-489 (2025).
75 Tang, P., Towner, D. J., Hamano, T., Meier, A. L. & Wessels, B. W. Electrooptic modulation up to 40 GHz in a barium titanate thin film waveguide modulator. *Opt. Express* **12**, 5962-5967 (2004).
76 Alexander, K. *et al.* A manufacturable platform for photonic quantum computing. *Nature* **641**, 876-883 (2025).
77 Li, Z. *et al.* High density lithium niobate photonic integrated circuits. *Nature Communications* **14**, 4856 (2023).
78 Niels, M. *et al.* A high-speed heterogeneous lithium tantalate silicon photonics platform. *Nature Photonics* **20**, 225-231 (2026).
79 In Kim, G., Yim, J. & Bahl, G. Low loss monolithic barium titanate on insulator integrated photonics with intrinsic quality factor >1 million. *arXiv e-prints*, arXiv:2507.17150 (2025).
80 Dong, Z. *et al.* Monolithic Barium Titanate Modulators on Silicon-on-Insulator Substrates. *ACS Photonics* **10**, 4367-4376 (2023).
81 Zhu, M., Du, Z., Jing, L., Yoong Tok, A. I. & Tong Teo, E. H. Optical and electro-optic anisotropy of epitaxial PZT thin films. *Applied Physics Letters* **107**, 031907 (2015).
82 Mao, J. *et al.* Ultra-fast perovskite electro-optic modulator and multi-band transmission up to 300 Gbit s−1. *Communications Materials* **5**, 114 (2024).
83 Alexander, K. *et al.* Nanophotonic Pockels modulators on a silicon nitride platform. *Nature Communications* **9**, 3444 (2018).
84 Xiong, C. *et al.* Active Silicon Integrated Nanophotonics: Ferroelectric BaTiO3 Devices. *Nano Letters* **14**, 1419-1425 (2014).
85 Ortmann, J. E. *et al.* Ultra-Low-Power Tuning in Hybrid Barium Titanate–Silicon Nitride Electro-optic Devices on Silicon. *ACS Photonics* **6**, 2677-2684 (2019).
86 Dötsch, H. *et al.* Applications of magneto-optical waveguides in integrated optics: review. *J. Opt. Soc. Am. B* **22**, 240-253 (2005).
87 Pingsheng, T., Towner, D. J., Meier, A. L. & Wessels, B. W. Low-loss electrooptic BaTiO/sub 3/ thin film waveguide modulator. *IEEE Photonics Technology Letters* **16**, 1837-1839 (2004).
88 Reynaud, M. *et al.* Electro-optic response in epitaxially stabilized orthorhombic mm2 BaTiO3. *Physical Review Materials* **5**, 035201 (2021).

89 Kormondy, K. J. *et al.* Microstructure and ferroelectricity of BaTiO3 thin films on Si for integrated photonics. *Nanotechnology* **28**, 075706 (2017).
90 Petraru, A., Schubert, J., Schmid, M., Trithaveesak, O. & Buchal, C. Integrated optical Mach Zehnder modulator based on polycrystalline BaTiO3. *Optics Letters* **28**, 2527-2529 (2003).
91 Winiger, J. *et al.* PLD Epitaxial Thin-Film BaTiO3 on MgO − Dielectric and Electro-Optic Properties. *Advanced Materials Interfaces* **11**, 2300665 (2024).
92 Cao, Y., Ng, J. D., Lin, H.-L., Tan, S. L. & Danner, A. An active straight waveguide polarization rotator in single crystal thin film barium titanate-on-insulator. *Applied Physics Letters* **122**, 031106 (2023).
93 Valdez, F., Mere, V. & Mookherjea, S. 100 GHz bandwidth, 1 volt integrated electro-optic Mach–Zehnder modulator at near-IR wavelengths. *Optica* **10**, 578-584 (2023).
94 Weigel, P. O. *et al.* Bonded thin film lithium niobate modulator on a silicon photonics platform exceeding 100 GHz 3-dB electrical modulation bandwidth. *Opt. Express* **26**, 23728-23739 (2018).
95 Li, Y. *et al.* High-Performance Mach–Zehnder Modulator Based on Thin-Film Lithium Niobate with Low Voltage-Length Product. *ACS Omega* **8**, 9644-9651 (2023).
96 Hassanien, A. E., Ghoname, A. O., Chow, E., Goddard, L. L. & Gong, S. Compact MZI modulators on thin film Z-cut lithium niobate. *Opt. Express* **30**, 4543-4552 (2022).
97 Yang, L. *et al.* Volume manufacturing of thin-film lithium niobate modulators with bandwidth 110 GHz based on 4-inch wafer with a quartz handle. *Light: Advanced Manufacturing* **6**, 575-581 (2025).
98 Xu, M. *et al.* High-performance coherent optical modulators based on thin-film lithium niobate platform. *Nature Communications* **11**, 3911 (2020).
99 Pan, B. *et al.* Demonstration of high-speed thin-film lithium-niobate-on-insulator optical modulators at the 2-μm wavelength. *Optics Express* **29**, 17710-17717 (2021).
100 Powell, K. *et al.* A sub-volt near-IR lithium tantalate electro-optic modulator. *APL Photonics* **10**, 091303 (2025).
101 Wang, C. *et al.* Ultrabroadband thin-film lithium tantalate modulator for high-speed communications. *Optica* **11**, 1614-1620 (2024).
102 Feutmba, G. F. *et al.* High frequency characterization of PZT thin-films deposited by chemical solution deposition on SOI for integrated high speed electro-optic modulators. *Opt. Mater. Express* **13**, 2120-2134 (2023).
103 Liu, G. *et al.* Highly efficient lead zirconate titanate ring modulator. *APL Photonics* **9**, 066111 (2024).
104 Chmielak, B. *et al.* Pockels effect based fully integrated, strained silicon electro-optic modulator. *Opt. Express* **19**, 17212-17219 (2011).
105 Xu, T. *et al.* Silicon-integrated scandium-doped aluminum nitride electro-optic modulator. *Photon. Res.* **13**, 477-487 (2025).
106 Schindler, P. C. *et al.* Monolithic GaAs Electro-Optic IQ Modulator Demonstrated at 150 Gbit/s With 64QAM. *J. Lightwave Technol.* **32**, 760-765 (2014).
107 Lin, S. H. & Wang, S.-Y. High-throughput GaAs PIN electrooptic modulator with a 3-dB bandwidth of 9.6 GHz at 1.3 μm. *Appl. Opt.* **26**, 1696-1700 (1987).
108 Spickermann, R., Dagli, N. & Peters, M. in *Optical Fiber Communications Conference.* ThK6 (Optica Publishing Group).
109 Ogiso, Y. *et al.* Over 67 GHz Bandwidth and 1.5 V Vπ InP-Based Optical IQ Modulator With n-i-p-n Heterostructure. *J. Lightwave Technol.* **35**, 1450-1455 (2017).
110 Lange, S. *et al.* Low Power InP-Based Monolithic DFB-Laser IQ Modulator With SiGe Differential Driver for 32-GBd QPSK Modulation. *J. Lightwave Technol.* **34**, 1678-1682 (2016).
111 Akiyama, S. *et al.* in *16th IPRM. 2004 International Conference on Indium Phosphide and Related Materials,* 581-584 (2004).

112 Burla, M. *et al.* 500 GHz plasmonic Mach-Zehnder modulator enabling sub-THz microwave photonics. *APL Photonics* **4**, 056106 (2019).
113 Kieninger, C. *et al.* Silicon-organic hybrid (SOH) Mach-Zehnder modulators for 100 GBd PAM4 signaling with sub-1 dB phase-shifter loss. *Opt. Express* **28**, 24693-24707 (2020).
114 Ummethala, S. *et al.* in *Conference on Lasers and Electro-Optics.* JTh5B.2 (Optica Publishing Group).
115 Liu, J. *et al.* Recent advances in polymer electro-optic modulators. *RSC Advances* **5**, 15784-15794 (2015).
116 Eltes, F. *et al.* Low-loss BaTiO3–Si waveguides for nonlinear integrated photonics. *ACS Photonics* **3**, 1698-1703 (2016).
117 Geler-Kremer, J. *et al.* A ferroelectric multilevel non-volatile photonic phase shifter. *Nature Photonics* **16**, 491-497 (2022).
118 Tomasulo, S. & Lee, M. L. Advances in wide-bandgap III-V solar cells. *Applied Physics Reviews* **12**, 031309 (2025).
119 Wen, P. *et al.* Waveguide coupled III-V photodiodes monolithically integrated on Si. *Nature Communications* **13**, 909 (2022).
120 Yu, Q. *et al.* Heterogeneous photodiodes on silicon nitride waveguides. *Optics Express* **28**, 14824-14830 (2020).
121 Maes, D. *et al.* High-speed uni-traveling-carrier photodiodes on silicon nitride. *APL Photonics* **8**, 016104 (2023).
122 Wei, C. *et al.* Ultra-wideband waveguide-coupled photodiodes heterogeneously integrated on a thin-film lithium niobate platform. *Light: Advanced Manufacturing* **4**, 30 (2023).
123 Feng, S., Geng, Y., Lau, K. M. & Poon, A. W. Epitaxial III-V-on-silicon waveguide butt-coupled photodetectors. *Optics Letters* **37**, 4035-4037 (2012).
124 Binetti, P. R. A. *et al.* InP/InGaAs Photodetector on SOI Photonic Circuitry. *IEEE Photonics Journal* **2**, 299-305 (2010).
125 Chen, G. *et al.* Integration of high-speed GaAs metal-semiconductor-metal photodetectors by means of transfer printing for 850 nm wavelength photonic interposers. *Optics Express* **26**, 6351-6359 (2018).
126 Lasaosa, D. *et al.* Traveling-wave photodetectors with high power-bandwidth and gain-bandwidth product performance. *IEEE Journal of Selected Topics in Quantum Electronics* **10**, 728-741 (2004).
127 Lei, L., Yujie, L., Chulchae, C., Bipin, B. & Ray, T. C. in *Proc.SPIE.* 10-16.
128 Jafari, M., Fatema, T., Carlson, D. R., Papp, S. B. & Beling, A. Heterogeneously Integrated AlGaAs/GaAs Photodiodes on Tantala Waveguides. *J. Lightwave Technol.* **42**, 8302-8307 (2024).
129 Geum, D.-M. *et al.* Monolithic integration of visible GaAs and near-infrared InGaAs for multicolor photodetectors by using high-throughput epitaxial lift-off toward high-resolution imaging systems. *Scientific Reports* **9**, 18661 (2019).
130 Wang, J. *et al.* InGaP/AlGaAs Near-UV and Visible Avalanche Photodiodes for Li-Fi Application. *IEEE Photonics Technology Letters* **36**, 293-296 (2024).
131 Park, T.-Y. *et al.* 2-Gb/s ultraviolet-light optical wireless communication by InGaN/GaN multi-quantum well dual-function micro-photodetector. *Applied Physics Letters* **124**, 061110 (2024).
132 Wang, J. *et al.* Polarization assisted self-powered GaN-based UV photodetector with high responsivity. *Photon. Res.* **9**, 734-740 (2021).
133 Chang, S.-J. *et al.* AlGaN Ultraviolet Metal–Semiconductor–Metal Photodetectors with Low-Temperature-Grown Cap Layers. *Japanese Journal of Applied Physics* **46**, 2471 (2007).
134 Yan, W. *et al.* On-Chip Nonreciprocal Photonic Devices Based on Hybrid Integration of Magneto-Optical Garnet Thin Films on Silicon. *IEEE Journal of Selected Topics in Quantum Electronics* **28**, 1-15 (2022).

135 Armelles, G., Cebollada, A. & Alvaro, R. Plasmon-phonon interaction effects on the magneto refractive response of spintronic-plasmonic/dielectric structures. *Optical Materials Express* **12**, 1092-1101 (2022).
136 Wei, Z. *et al.* Recent development of magneto-optical thin films and integrated photonic devices. *Journal of Materials Chemistry C* **13**, 12628-12649 (2025).
137 Serrano-Núñez, M. A., Shoji, Y. & Mizumoto, T. Small magnetless integrated optical isolator using a magnetized cobalt ferrite film. *IEICE Electronics Express* **19**, 20210500-20210500 (2022).
138 Choueikani, F. *et al.* Magneto-optical waveguides made of cobalt ferrite nanoparticles embedded in silica/zirconia organic-inorganic matrix. *Applied Physics Letters* **94** (2009).
139 Serrano-Núñez, M. A., Shoji, Y. & Mizumoto, T. J. A. P. E. Giant Faraday rotation of cobalt ferrite thin films deposited on silicon substrates for silicon photonic nonreciprocal device applications. *Applied Physics Express* **13**, 062002 (2020).
140 Sato, K., Okano, M. & Shoji, Y. Ultra-compact microring optical isolator using an aluminum-substituted cobalt ferrite thin film. *Optica* **11**, 889-895 (2024).
141 Bahl, C. R. H. Estimating the demagnetization factors for regular permanent magnet pieces. *AIP Advances* **11**, 075028 (2021).
142 Srinivasan, K. & Stadler, B. J. Magneto-optical materials and designs for integrated TE-and TM-mode planar waveguide isolators: a review. *Optical Materials Express* **8**, 3307-3318 (2018).
143 Dillon, J. F., Jr. Origin and Uses of the Faraday Rotation in Magnetic Crystals. *Journal of Applied Physics* **39**, 922-929 (1968).
144 Yan, W. *et al.* Ultra-broadband magneto-optical isolators and circulators on a silicon nitride photonics platform. *Optica* **11**, 376-384 (2024).
145 Zhu, X. D. Magnetic domains and unusual hysteresis loops of yttrium iron garnet crystals revealed by magneto-optic effects. *AIP Advances* **11**, 085214 (2021).
146 Li, G. *et al.* Tunable perpendicular magnetic anisotropy in epitaxial Y3Fe5O12 films. *APL Materials* **7**, 041104 (2019).
147 Zhang, Y. *et al.* Monolithic integration of broadband optical isolators for polarization-diverse silicon photonics. *Optica* **6**, 473-478 (2019).
148 Tien, M.-C., Mizumoto, T., Pintus, P., Kromer, H. & Bowers, J. E. Silicon ring isolators with bonded nonreciprocal magneto-optic garnets. *Optics Express* **19**, 11740-11745 (2011).
149 Shoji, Y., Mizumoto, T., Yokoi, H., Hsieh, I.-W. & Osgood, R. M. J. A. p. l. Magneto-optical isolator with silicon waveguides fabricated by direct bonding. *Appl. Phys. Lett.* **92** (2008).
150 Yan, W. *et al.* Waveguide-integrated high-performance magneto-optical isolators and circulators on silicon nitride platforms. *Optica* **7**, 1555-1562 (2020).
151 Ghosh, S. *et al.* Ce: YIG/Silicon-on-Insulator waveguide optical isolator realized by adhesive bonding. *Optics Express* **20**, 1839-1848 (2012).
152 Bi, L. *et al.* Magneto-optical thin films for on-chip monolithic integration of non-reciprocal photonic devices. *Materials* **6**, 5094-5117 (2013).
153 Bi, L. *et al.* On-chip optical isolation in monolithically integrated non-reciprocal optical resonators. *Nature Photonics* **5**, 758-762 (2011).
154 Srinivasan, K. *et al.* High-gyrotropy seedlayer-free Ce: TbIG for monolithic laser-matched SOI optical isolators. *ACS Photonics* **6**, 2455-2461 (2019).
155 Šimša, Z. *et al.* Optical absorption and faraday rotation of barium hexaferrite films prepared by laser ablation deposition. *Journal of Physics and Chemistry of Solids* **59**, 111-119 (1998).
156 Sukhorukov, Y. P. *et al.* Magnetooptical Faraday effect in La0. 7Sr0. 3MnO3− δ films. *Technical Physics* **46**, 778-781 (2001).
157 Spencer, D. T. *et al.* An optical-frequency synthesizer using integrated photonics. *Nature* **557**, 81-85 (2018).
158 Xu, H. *et al.* Two-dimensional materials for integrated sensing. *Nature Materials* (2026).

159 Park, S. H. *et al.* Universal selective transfer printing via micro-vacuum force. *Nature Communications* **14**, 7744 (2023).
160 Masubuchi, S. *et al.* Autonomous robotic searching and assembly of two-dimensional crystals to build van der Waals superlattices. *Nature Communications* **9**, 1413 (2018).
161 Niklaus, F., Stemme, G., Lu, J. Q. & Gutmann, R. J. Adhesive wafer bonding. *Journal of Applied Physics* **99**, 031101 (2006).
162 Han, S. *et al.* High energy density in artificial heterostructures through relaxation time modulation. *Science* **384**, 312-317 (2024).
163 Chen, L. *et al.* Fully automatic transfer and measurement system for structural superlubric materials. *Nature Communications* **14**, 6323 (2023).
164 Nakatani, M. *et al.* Ready-to-transfer two-dimensional materials using tunable adhesive force tapes. *Nature Electronics* **7**, 119-130 (2024).
165 Daudlin, S. *et al.* Three-dimensional photonic integration for ultra-low-energy, high-bandwidth interchip data links. *Nature Photonics* **19**, 502-509 (2025).
166 Wan, Y. *et al.* Integrating silicon photonics with complementary metal–oxide–semiconductor technologies. *Nature Reviews Electrical Engineering* **3**, 15-31 (2026).
167 Xu, R. *et al.* Strain-induced room-temperature ferroelectricity in SrTiO3 membranes. *Nature Communications* **11**, 3141 (2020).
168 Rahul *et al.* Crafting moiré superlattices in twisted complex oxide–transition metal dichalcogenide heterostructures. *Nature Communications* **17**, 3025 (2026).
169 Jani, H. *et al.* Spatially reconfigurable antiferromagnetic states in topologically rich free-standing nanomembranes. *Nature Materials* **23**, 619-626 (2024).